論文 / 著書情報
Article / Book Information

題目(和文)	
Title(English)	Low and Extremely Low Cycle Fatigue Performances of Various Structural Steels
著者(和文)	トッチ タイリン
Author(English)	THAILEANG TOUCH
出典(和文)	学位:博士(工学), 学位授与機関:東京工業大学, 報告番号:甲第12467号, 授与年月日:2023年3月26日, 学位の種別:課程博士, 審査員:吉敷 祥一,元結 正次郎,石原 直,西村 康志郎,佐藤 大樹,山田 哲
Citation(English)	Degree:Doctor (Engineering), Conferring organization: Tokyo Institute of Technology, Report number:甲第12467号, Conferred date:2023/3/26, Degree Type:Course doctor, Examiner:,,,,,
学位種別(和文)	博士論文
Type(English)	Doctoral Thesis

A thesis submitted for the degree of

Doctor of Engineering

Low and Extremely Low Cycle Fatigue Performances of Various Structural Steels

Thaileang Touch

Supervisor: Prof. Shoichi Kishiki

Department of Architecture and Building Engineering

Tokyo Institute of Technology

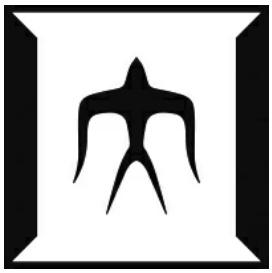

March 2023

Contents

Abstract

The earthquake resistance of steel building structures depends on the energy dissipation capacity of structural members. The energy dissipation capacity of steel members subjected to cyclic loading is based on the deformation capacity of the steel materials. To date, numerous studies have been conducted on the seismic performances of steel structural frame, the deformation capacity of steel members and correlation between the deformation capacities of structural frames and members. In verifying the safety margin of earthquake-resistant buildings, it is important to evaluate their seismic performances under the extremely severe earthquakes. In such a case, the critical part of the member (associated with steel material behavior) is exposed to very large strain (that belongs to extremely LCF regime). Conducting cyclic tests on the steel materials under large strain to better understand their behaviors is crucial for determining the material's suitability for high strain applications and seismic performance. However, conducting such cyclic loading tests present lots of challenges, e.g. due to buckling.

This dissertation aims to investigate the low-cycle fatigue performances (LCF) of various 400 N/mm^2 (SS400), 490 N/mm^2 (SM490A), 590 N/mm^2 (SA440C) structural steels in the LCF and ECLCF regimes. First, the parametric studies were conducted numerically and experimentally to obtain the optimal specimen shape for LCF tests including very large strain amplitudes. The reduced section to diameter (Le/D) ratio and radius of fillet to diameter (R/D) ratio of the specimen are deemed to have beneficial and detrimental effects on the performance of the specimen. For example, large Le/D ratios are good for tensile test but increase the slenderness ratio, making the material prone to buckling under compression. Small R/D may cause stress concentration at the corner of

R section. Nevertheless, the range of the appropriate specimen's proportional ratios are not known. Therefore, *Le* and *R* were used as the parameters to investigate the influences of these ratios. Based on the analytical result, optimal proportional ratios used for large strain tests were proposed. The validation of the proportional ratios were also verified from the material tests and database from previous studies.

By using the appropriate specimen shape, cyclic loading tests were conducted on structural steels with different grades which cover both small (2%) and large (12%) strain amplitudes to investigate the LCF and ECLF performances of the structural steels. First, the test parameters such as steel materials, strain amplitudes and loading conditions (i.e., tension-compression and compression-tension cyclic loadings) were introduced. Based on the test results, the hysteretic curve when illustrated in the nominal and true stress-strain curves were compared followed by the true stress-true strain curves of different structural steels. It was found that the relationship of true stress and true strain is more appropriate in expressing the hysteretic curves, given a wide range of large plastic strains. The LCF performance of SS400 steel was compared with the previous study, and their LCF performances showed a good linear relationship together. This signified the study's data is validated. The LCF performance with large plastic strain was investigated further, considering the effects of steel lots, initial loading direction and steel grades. As a result, the LCF and ELCF performances of the considered structural steels can be evaluated in a unified manner up to about 10% strain. The LCF equation was then obtained using this result. The deformation capacity up to the ultimate point N_{di} of various structural steels is also considered in addition to that up to fracture N_f. By defining the damage initiation (onset of crack or neck) as the ultimate point, the deformation capacity up to ultimate point of the considered structural steels (SS400, SM490A, SA440C) can be evaluated

using one N_{di} equation from 2% to 12% strains. From the variable amplitude cyclic tests, the N_{di} equation was also confirmed to be validated under the seismic loads which are typically the loading patterns consisting of more than one amplitude.

As an application of the materials' evaluation equations, the LCF performance of steel members is also discussed in Appendix 1. However, the purpose is not to precisely evaluate a member based on the material's equation; rather, to demonstrate the performance calculated by the material's equation can be used as an indicator of the desired performance of the member.

Chapter 1 Motivation and Objective of the Research

Outline for Chapter 1

1.1. Research background

The earthquake resistance of steel structural frame depends on the energy dissipation capacity of structural members (e.g., steel beams, buckling-restrained braces). The energy dissipation capacity of steel members subjected to cyclic loading is determined by the deformation capacity of the steel materials. Fig. 1.1 illustrates the schematic correlation between steel structural frame, steel members and steel materials.

To date, numerous studies have been conducted on the seismic performance of steel structural frames e.g., [1.1–1.3], plastic deformation capacity of steel members e.g., [1.4–1.7], and correlation between the deformation capacities of structural frames and members e.g., [1.8, 1.9]. In verifying the safety margin of earthquake-resistant buildings, it is important to evaluate their seismic performances under the extremely severe earthquakes. In such a case, the critical part of the member (which is associated with the behavior of the steel material) is subjected to extremely large strain amplitude.

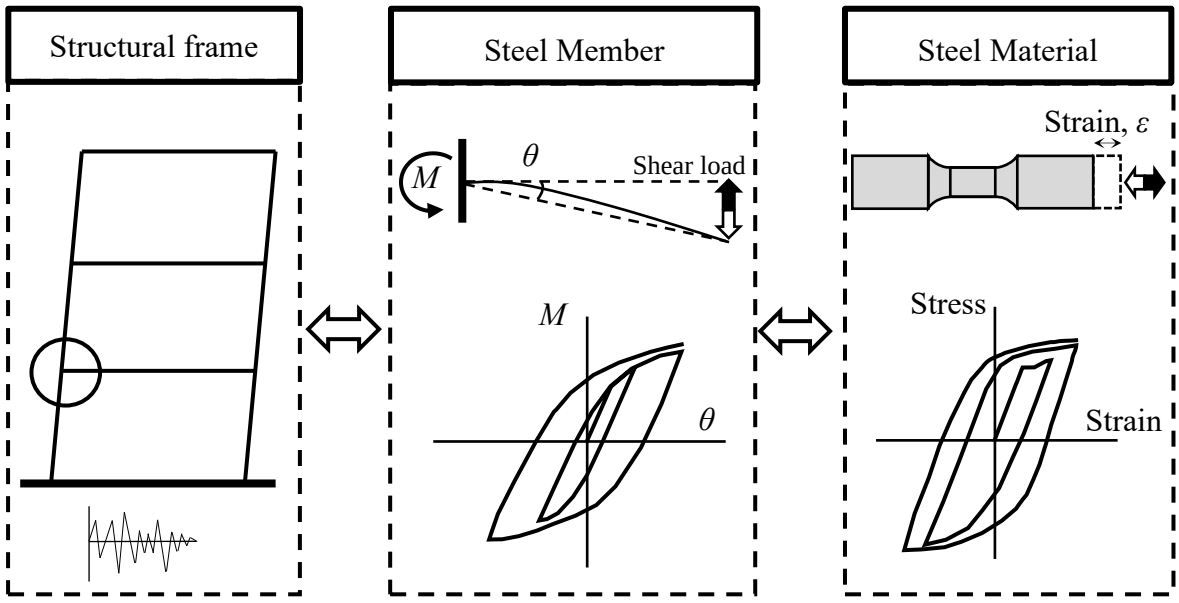

Fig. 1.1 Schematic relationship between steel structural frame, member and materials

Conducting cyclic tests on the steel materials under large strain to better understand their behaviors is crucial for determining the material's suitability for high strain applications and seismic performance. However, performing such tests presents numerous challenges, e.g., due to buckling. Therefore, there is still insufficient knowledge of the cyclic deformation capacities of structural steel materials over a wide range of amplitudes from small to large strains.

1.2. Literature review

Steel building structures are extensively used in high seismic zones. As steel is ductile, these systems are considered to have sufficient strength as well as ductile behavior themselves, which enable the structural components to resist intense lateral loads, such as generated by strong earthquakes. Under this strong earthquake, steel members susceptible to plasticity, i.e., beam ends, may fracture owing to low-cycle fatigue (LCF) or extremely low-cycle fatigue (ELCF) [1.10, 1.11]. To date, research studies on the low-cycle fatigue behaviors of structural steels have been extensively conducted, and various life-prediction models have also been proposed.

Review on LCF and ELCF life prediction models

In the case of steel materials subjected to cyclic loading in the axial direction with the number of cycles to failure ($N_f < 10^4$ cycles), it is common to evaluate the deformation performance up to fracture by employing the Manson–Coffin [1.12, 1.13] relationship, which is the empirical formula of the LCF life when the specimen is subjected to cyclic loading with constant strain amplitudes. However, it has been shown in previous studies [1.14, 1.15] that log–log plot of test data deviate from the Manson–Coffin relationship at larger strain amplitudes. Moreover, researchers [1.16, 1.17] who conducted studies on the LCF behavior of low-carbon steel also observed the deviation from the Manson–Coffin relationship at shorter life, i.e., for $N_f < 10^2$ cycles, that belong to the extremely low-cycle fatigue (ELCF) regime. In some literatures e.g. [1.18, 1.19], the ELCF (also referred to as ultra-low cycle fatigue) is defined with the number of cycles to fracture less than 20 cycles. Additionally, the study by Pereira et al. [1.20] who had conducted some cyclic tests in an effort to investigate the ELCF behavior of structural steel has shown that the Manson–Coffin relationship does not provide a satisfactory life prediction because it predicts shorter life in this regime. In other words, it can be concluded that the Manson-Coffin model can be only suitable for the LCF regime [1.14–1.17, 1.20–1.23]. This is because the fracture mechanism of steel materials subject to LCF is different from that subject to ELCF [1.24, 1.25], and thus, the prediction method used with LCF cannot be appropriate for ELCF.

To cope with the discrepancy of the aforementioned model, many extensive research studies [1.21–1.23] have been conducted to propose a method to predict the ELCF life subject to extreme load conditions or very large strains. Kuroda et al. [1.21] proposed a cumulative damage model based on the damage induced by ductility exhaustion and crack

propagation. The model was reported to exhibit a good agreement with test data of annealed low-carbon steel of S20C in extremely low-cycle fatigue regimes. Tateishi et al. [1.22] devised a new ELCF prediction model based on the concept of the damage mechanism, and the model was also validated with the test data from base and weld materials. Conversely, Nip et al. [1.23] who had conducted ELCF tests on structural low-carbon steel with a limited range of strain amplitudes—in which the chemical compositions are different from those employed in the literatures [1.21, 1.22]—has indicated that the Kuroda and Tateishi models do not show good correspondence with the test data in a broad range from LCF to ELCF, and could not accurately predict the results of tensile tests and at smaller strain amplitudes. This emphasizes a clear need to experimentally investigate the cyclic deformation capacity (herein, strain-life curve) of steel materials in a broader range of strain amplitudes from the LCF to ELCF regimes in a continuous manner.

Review on challenge in conducting LCF and ELCF tests

Nonetheless, thus far, limited test data exist on the stress–strain hysteretic curve and life of structural steel that is plastically deformed when subjected to extremely large cyclic strains. One of the possible reasons for the lack of these types of experimental studies could be attributed to the design of a test specimen that can avoid stress concentrations at the edge of the effective length section and at the same time can also prevent premature buckling until it reaches fracture when it is subjected to large compressive strain. Furthermore, it has been reported in previous studies [1.26–1.28] that only a limited range of strain-based cyclic test could be conducted owing to the restrictions on the test apparatus. Additionally, to conduct strain-based cyclic test subject to larger compressive

strains, two different specimen shapes were used in the previous studies [1.20, 1.28] to reduce instability and buckling. Regardless of the challenge, similar efforts have also been expended by other researchers to investigate the ELCF behavior of structural steels to acquire test data in this regime [1.20, 1.26–1.30]. In these studies, the cyclic tests with strain amplitudes (half amplitude, ε) up to approximately 7% were conducted. Accordingly, the strain-life curve was reported to be linear [1.20, 1.26–1.29]. However, subject to intense lateral loads, such as those generated by severe earthquakes, steel members may undergo large-strain amplitudes [1.31–1.35] and fracture after an extremely low number of cycles (in the order of 10 cycles) which this fracture could be classified in ELCF [1.18,1.36–1.38]. Besides, the experimental investigations by researchers [1.39–1.41] after the great Hanshin-Awaji earthquake in 1995 have indicated that steel members may undergo strain amplitudes of the order of 8% or larger during the earthquake, which is clearly larger than the existing (strain amplitudes up to approximately 7%) ELCF database. Also, the equivalent axial strain of the shear damper may reach 9.2%, according to a recent study by He et al. [1.42]. In other words, prior studies of the ELCF behaviors of structural steel at even larger strain amplitudes ($\geq$ 8%) have been limited (schematically illustrated in Fig. 1.6).

Hawileh et al. [1.43, 1.44] experimentally examined the plastic deformation of the different steel bars subjected to cyclic tests with peak strains up to 8%. The study in [1.43] shows that the deformation capacities of ASTM A706 and A615 carbon steels are similar. While the study in [1.44] indicates that ASTM A36 and AISI 1117 outperformed the others (AISI 8620, 1018, 1045, 1215, 4140) at 3% and 4%. Liu et al. [1.45] studied the plastic deformation capacities of Q235B and Q345B steels and their butt-welded joints with strains up to 16% and compressive strain is kept as 1%. It should be noticed that the

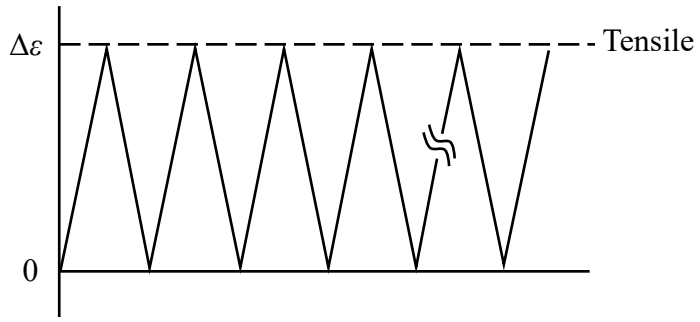

Fig. 1.2 Constant amplitude loading history with 0% compressive strain

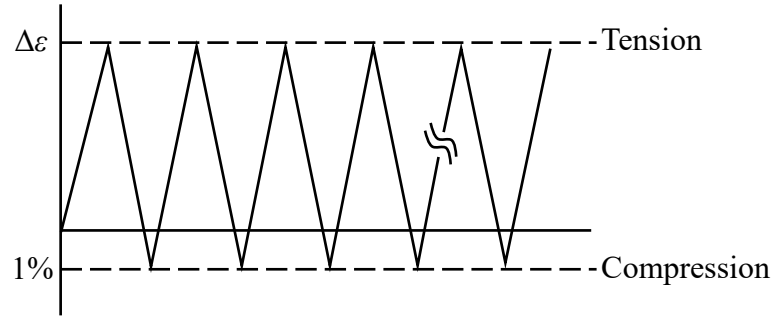

Fig. 1.3 Constant amplitude loading history with 1% compressive strain

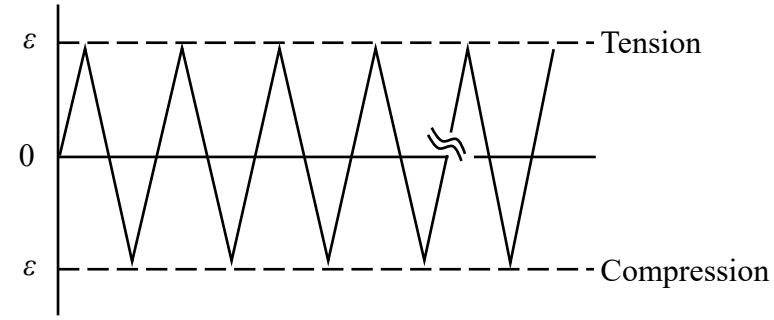

Fig. 1.4 Constant amplitude loading history with fully reversed strain

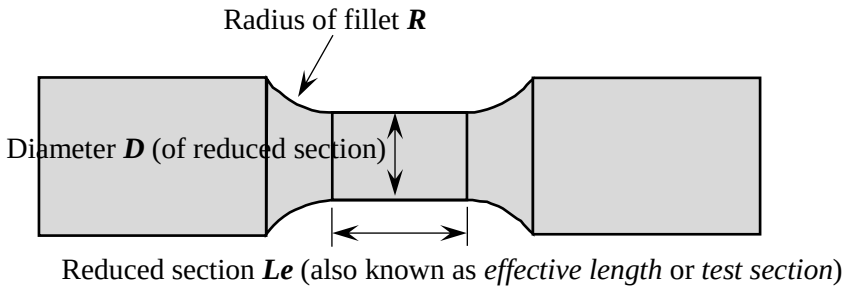

Fig. 1.5 Schematic specimen shape

studies [1.43–1.45] considered the peak strains up to 8% and 16% but the compressive strain is restrained as zero and 1%, as shown in Figs. 1.2 and 1.3 respectively, to prevent the buckling of the specimen (i.e., half-amplitude strain $\varepsilon \sim \pm 8\%$). Considering the fully reversed tensile and compressive strain, Tateishi et al. [1.22] conducted cyclic tests with strains up to ±7.5% by using a newly developed testing system reported in [1.41], in which specimens were subjected to bending deformation. Besides, in an attempt to enable the fully reversed uniaxial loadings (Fig. 1.4), Nip et al. [1.23] and Weigand et al. [1.46] conducted cyclic tests on the specimens with rectangular cross section up to strains of ±7% and ±8%, respectively, by adding the guide plate surrounding the specimen to restrain against compressive buckling. Without the aid of the buckling-restrained guide plate, Dusicka et al. [1.47] used specimens with round cross section to conduct uniaxial cyclic tests with strains up to ±7% by changing the reduced-section-to-diameter Le/D (refer to Fig. 1.5 for location) ratios of 2.0 recommended by ASTM E606 [1.48] to 1.25 to minimize the compressive buckling. Moreover, by employing the small reduced-section-to-diameter Le/D ratios of 1.17 and 1.13, recent experimental studies [1.49, 1.50] on the deformation capacities of (Q235, Q345) carbon steels subjected to uniaxial cyclic loadings can be tested with large strain amplitudes extended up to ±9%. It is clearly seen that the experimental investigations of the structural steels under large strain amplitudes (currently at ±9% or smaller) have been drawing much interest in recent years. Nevertheless, there is still insufficient knowledge of the cyclic deformation capacity of such steels over a wide range of amplitudes from small to larger strains (> ±9%). Therefore, the cyclic deformation capacities of various structural steels that ranged from LCF to ELCF regimes in a continuous manner have not been modeled comprehensively.

1.3. Objective of this study

The main objective of this study is to experimentally investigate the low cycle fatigue performances of the 400 N/mm^2 (SS400), 490 N/mm^2 (SM490A), 590 N/mm^2 (S440C) grade structural steels, specifically focus on the ELCF (strain amplitudes ≥ 8%) regime but in a continuous manner from LCF to ELCF regimes (as illustrated in Fig. 1.6) to provide a qualitative database for further researches. To enable the LCF test including large strains, first the parametric studies were conducted numerically and experimentally to obtain the optimal specimen shape for lage strain cyclic loadings. Using the specimen shape, the cyclic tests were performed on various strucural steels with strain amplitudes ranged from 2% to 12% which cover LCF and inlcuding very large plastic strain (Extremely LCF). Based on the results, the effect of steel materials on LCF performance was elucidated. As an application of the materials' evaluation equations, the LCF performance of steel members is also discussed in Appendix 1. However, the purpose is not to precisely evaluate a member based on the material's equation; rather, to demonstrate the performance calculated by the material's equation can be used as a benchmark for the performance which the members should aim for.

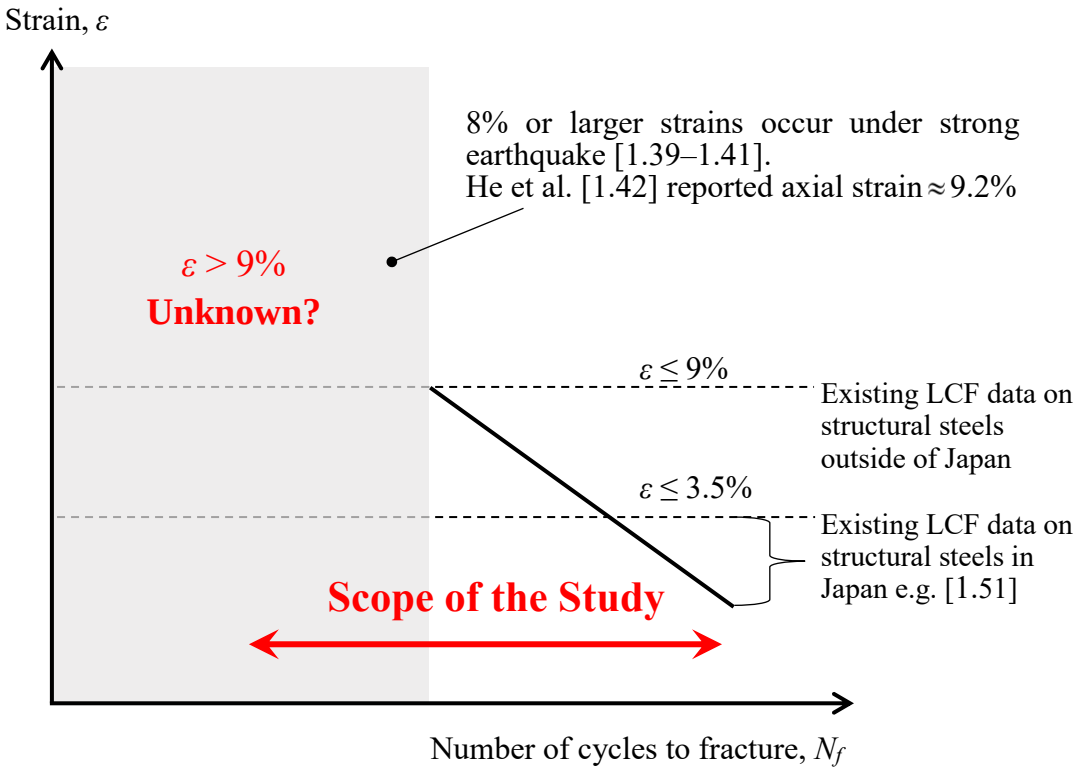

Fig. 1.6 Schematic LCF curve of current limited data and scope of the study

1.4. Structure of dissertation

This dissertation consists of 3 chapters, and method for LCF tests (refer to cyclic loading tests with constant strain amplitudes) including large strain amplitude, LCF and ELCF performances of various structural steels considering the effect of initial loading directions and steel lots. The contents and key features in each chapter are outlined as follows.

Chapter 2: The main objective of this chapter is to obtain appropriate specimen shape used for LCF and ELCF tests. The parametric studies were conducted numerically and experimentally to obtain the optimal specimen shape for LCF tests including large strain amplitudes. The reduced section to diameter (Le/D refer to Fig. 1.5 for location) ratio and radius of fillet to diameter (R/D) ratio of the specimen are deemed to have beneficial and detrimental effects on the performance of the specimen. For example, large Le/D ratios are good for tensile test but increase the slenderness ratio, making the material prone to out-of-plane deformation unuder compression. Small R/D may cause stress concentration at the corner of R section. Nevertheless, the range of the appropriate specimen's proportional ratios are not known. Therefore, Le and R are used as the parameters to investigate the influences of these ratios. Based on the analytical result, optimal proportional ratios used for large strain tests were proposed. The validation of the proportional ratios were also verified from the material tests and database from the previous studies.

Chapter 3: The objective is to investigate the LCF and ELCF performances of structural steels with different strengths. By using appropriate specimen shape discussed in Chapter

2, cyclic loading tests were conducted on structural steels with different grades which cover both small (2%) and large (12%) strain amplitudes. First, the test parameters such as steel materials, strain amplitudes and loading conditions are introduced. Based on the test results, the hysteretic curve when illustrated in the nominal stress-strain and true stress-strain curves are compared followed by the true stress-true strain curves of different structural steels. Then, the LCF performance of SS400 steel is compared with previous result to validate this study's test data. After validation, the LCF performance with large plastic strains is investigated further, taking the effects of the steel lots and initial loading direction (tension-compression and compression-tension cyclic loadings) into account. Consequently, the effect of the different structural steels on LCF performance was also examined. In addition to that up to fracture, the deformation capacity of steel materials up to the ultimate point is also investigated. The equation for evaluating the deformation capacity up to the ultimate point is proposed and validated using the result from variable amplitude cyclic loading tests.

Chapter 4: The main conclusion discussed throughout Chapters 2 and 3 will be summarized. Lastly, the limitation and suggested future studies are introduced.

References for chapter 1

[1.1] Roeder CW, Popov EP. Eccentrically braced steel frames for earthquakes. Journal of the Structural Division 1978;104:391–412. https://doi.org/10.1061/JSDEAG.0004875.

[1.2] Foutch DA, Goel SC, Roeder CW. Seismic testing of full-scale steel building—Part I. Journal of Structural Engineering 1987;113:2111–29. https://doi.org/10.1061/(ASCE)0733-9445(1987)113:11(2111).

[1.3] Yamanouchi H, Midorikawa M, Nishiyama I, Watabe M. Seismic behavior of full-scale concentrically braced steel building structure. Journal of Structural Engineering 1989;115:1917–29. https://doi.org/10.1061/(ASCE)0733-9445(1989)115:8(1917).

[1.4] Malley JO, Popov EP. Shear links in eccentrically braced frames. Journal of Structural Engineering 1984;110:2275–95. https://doi.org/10.1061/(ASCE)0733-9445(1984)110:9(2275).

[1.5] Krawinkler H. Performance assessment of steel components. Earthquake Spectra 1987;3:27–41. https://doi.org/10.1193/1.1585417.

[1.6] Wallace BJ, Krawinkler H. Small-scale model tests of structural steel assemblies. Journal of Structural Engineering 1989;115:1999–2015. https://doi.org/10.1061/(ASCE)0733-9445(1989)115:8(1999).

[1.7] Kishiki S, Lee DS, Yamada S, Ishida T, Jiao Y. Low-cycle fatigue performance assessment of current Japanese steel beam-to-column connections determined by ductile fracture. Eng Struct 2019;182:241–50. https://doi.org/10.1016/j.engstruct.2018.12.061.

[1.8] Zhou H, Wang Y, Yang L, Shi Y. Seismic low-cycle fatigue evaluation of welded

beam-to-column connections in steel moment frames through global-local analysis. Int J Fatigue 2014;64:97–113. https://doi.org/10.1016/j.ijfatigue.2014.03.002.

[1.9] Tenderan R, Ishida T, Jiao Y, Yamada S. Seismic performance of ductile steel moment-resisting frames subjected to multiple strong ground motions. Earthquake Spectra 2019;55:289–310. https://doi.org/10.1193/111217EQS235M.

[1.10] Mahin SA. Lessons from damage to steel buildings during the Northridge earthquake. Eng Struct 1998;20:261–70. https://doi.org/10.1016/S0141-0296(97)00032-1.

[1.11] Kuwamura H. Fracture of steel during an earthquake—state-of-the-art in Japan. Eng Struct 1998;20:310–22. https://doi.org/10.1016/S0141-0296(97)00030-8.

[1.12] Manson SS. Behavior of materials under conditions of thermal stress. J Appl Phys 1943;14:399–405.

[1.13] Coffin LF. A study of the effects of cyclic thermal stresses in ductile metals. Transaction of the ASME 1954;76:931–50.

[1.14] Mediratta SR, Ramaswamy V, Rama Rao P. Two stage cyclic work hardening and two slope coffin-manson relationship in dual phase steels. Scripta Metallurgica 1986. https://doi.org/10.1016/0036-9748(86)90253-X.

[1.15] Radhakrishnan VM. On the bilinearity of the Coffin-Manson low-cycle fatigue relationship. Int J Fatigue 1992;14:305–11. https://doi.org/10.1016/0142-1123(92)90481-Q.

[1.16] Shimada K, Komotori J, Shimizu M. The applicability of the Manson-Coffin law and Miner's law to extremely low cycle fatigue. Transactions of the Japan Society of Mechanical Engineers Series A 1987;53:1178–85. https://doi.org/10.1299/kikaia.53.1178.

[1.17] Kikuwa M, Ohji K, Ohkubo H, Yokoi T, Morikawa T. Damage and recovery from it in low cycle fatigue. Transactions of the Japan Society of Mechanical Engineers 1972;38:8–15. https://doi.org/10.1299/kikai1938.38.8.

[1.18] Kanvinde AM, Deierlein GG. Micromechanical Simulation of Earthquake-Induced Fracture in Steel Structures. John A Blume Earthquake Engineering Center Technical Report 2004;145.

[1.19] Zhou H, Wang Y, Shi Y, Xiong J, Yang L. Extremely low cycle fatigue prediction of steel beam-to-column connection by using a micro-mechanics based fracture model. Int J Fatigue 2013;48:90–100. https://doi.org/10.1016/J.IJFATIGUE.2012.10.006.

[1.20] Pereira JCR, de Jesus AMP, Xavier J, Fernandes AA. Ultra low-cycle fatigue behaviour of a structural steel. Eng Struct 2014;60:214–22. https://doi.org/10.1016/j.engstruct.2013.12.039.

[1.21] Kuroda M. Extremely low cycle fatigue life prediction based on a new cumulative fatigue damage model. Int J Fatigue 2002;24:699–703. https://doi.org/10.1016/S0142-1123(01)00170-0.

[22] Tateishi K, Hanji T, Minami K. A prediction model for extremely low cycle fatigue strength of structural steel. Int J Fatigue 2007;29:887–96. https://doi.org/10.1016/j.ijfatigue.2006.08.001.

[1.23] Nip KH, Gardner L, Davies CM, Elghazouli AY. Extremely low cycle fatigue tests on structural carbon steel and stainless steel. J Constr Steel Res 2010;66:96–110. https://doi.org/10.1016/J.JCSR.2009.08.004.

[1.24] Kermajani M, Ghaini FM, Miresmaeili R, Aghakouchak AA, Shadmand M. Effect of weld metal toughness on fracture behavior under ultra-low cycle fatigue loading

(earthquake). Materials Science and Engineering A 2016;668:30–7. https://doi.org/10.1016/j.msea.2016.03.086.

[1.25] Zhang Q, Zhang J, Zhao P, Huang Y, Yu Z, Fang X. Low-cycle fatigue behaviors of a new type of 10% Cr martensitic steel and welded joint with Ni-based weld metal. Int J Fatigue 2016;88:78–87. https://doi.org/10.1016/j.ijfatigue.2016.03.003.

[1.26] Dodd LL, Restrepo-Posada JI. Model for predicting cyclic behavior of reinforcing steel. Journal of Structural Engineering (United States) 1995;121:433–45. https://doi.org/10.1061/(ASCE)0733-9445(1995)121:3(433).

[1.27] Kawamoto M, Tanaka T. Completely reversed axial fatigue tests of steel in the plastic range. Journal of the Japan Society for Testing Materials 1962;11:363–73. https://doi.org/10.2472/jsms1952.11.363.

[1.28] Smith RW, Hirschberg MH, Manson SS. Fatigue behavior of materials under strain cycling in low and intermediate life range. NASA TND-1574 1963:57.

[1.29] Okashita K, Ohminami R, Michiba K, Yamamoto A, Tomimatsu M, Tanji Y, et al. Investigation of the brittle fracture at the corner of P75 rigid-frame pier in Kobe harbor highway during the hyogoken-nanbu earthquake. Journal of Japan Society of Civil Engineers 1998:243–61. https://doi.org/10.2208/jscej.1998.591_243.

[1.30] Kamaya M. Fatigue properties of 316 stainless steel and its failure due to internal cracks in low-cycle and extremely low-cycle fatigue regimes. Int J Fatigue 2010;32:1081–9. https://doi.org/10.1016/j.ijfatigue.2009.12.003.

[1.31] Amiri HR, Aghakouchak AA, Shahbeyk S, Engelhardt MD. Finite element simulation of ultra low cycle fatigue cracking in steel structures. J Constr Steel Res 2013;89:175–84. https://doi.org/10.1016/j.jcsr.2013.07.007.

[1.32] Bleck W, Dahl W, Nonn A, Amlung L, Feldmann M, Schäfer D, et al. Numerical

and experimental analyses of damage behaviour of steel moment connection. Eng Fract Mech 2009;76:1531–47. https://doi.org/10.1016/j.engfracmech.2009.03.004.

[1.33] Tong L, Huang X, Zhou F, Chen Y. Experimental and numerical investigations on extremely-low-cycle fatigue fracture behavior of steel welded joints. J Constr Steel Res 2016;119:98–112. https://doi.org/10.1016/j.jcsr.2015.12.015.

[1.34] Huang X, Zhao J. A cumulative damage model for extremely low cycle fatigue cracking in steel structure. Structural Engineering and Mechanics 2017;62:225–36. https://doi.org/10.12989/sem.2017.62.2.225.

[1.35] Algarni M, Choi Y, Bai Y. A unified material model for multiaxial ductile fracture and extremely low cycle fatigue of Inconel 718. Int J Fatigue 2017;96:162–77. https://doi.org/10.1016/j.ijfatigue.2016.11.033.

[1.36] Kanvinde AM, Deierlein GG. Cyclic void growth model to assess ductile fracture initiation in structural steels due to ultra low cycle fatigue. J Eng Mech 2007;133:701–12. https://doi.org/10.1061/(ASCE)0733-9399(2007)133:6(701).

[1.37] Huang X, Tong L, Zhou F, Chen Y. Prediction of fracture behavior of beam-to-column welded joints using micromechanics damage model. J Constr Steel Res 2013;85:60–72. https://doi.org/10.1016/j.jcsr.2013.02.014.

[1.38] Mendes LAM, Castro LMSS. A simplified reinforcing steel model suitable for cyclic loading including ultra-low-cycle fatigue effects. Eng Struct 2014;68:155–64. https://doi.org/10.1016/j.engstruct.2014.02.031.

[1.39] Sakano M, Mikami I, Takaba S. Low cycle fatigue behavior of steel pier beam-column joint. Doboku Gakkai Ronbunshu 1997:49–60. https://doi.org/10.2208/jscej.1997.563_49.

[1.40] Sakano M, Wahab MA. Extremely low cycle (ELC) fatigue cracking behaviour in

steel bridge rigid frame piers. J Mater Process Technol 2001;118:36–9. https://doi.org/10.1016/S0924-0136(01)00857-3.

[1.41] Tateishi K, Hanji T. Low cycle fatigue strength of butt-welded steel joint by means of new testing system with image technique. Int J Fatigue 2004;26:1349–56. https://doi.org/10.1016/j.ijfatigue.2004.03.016.

[1.42] He Q, Chen Y, Ke K, Yam MCH, Wang W. Experiment and constitutive modeling on cyclic plasticity behavior of LYP100 under large strain range. Constr Build Mater 2019;202:507–21. https://doi.org/10.1016/j.conbuildmat.2018.12.146.

[1.43] Hawileh R, Rahman A, Tabatabai H. Evaluation of the low-cycle fatigue life in ASTM A706 and A615 grade 60 steel reinforcing bars. Journal of Materials in Civil Engineering 2010;22:65–76. https://doi.org/10.1061/(ASCE)0899-1561(2010)22:1(65).

[1.44] Hawileh RA, Tabatabai H, Abu-Obeidah A, Balloni J, Rahman A. Evaluation of the low-cycle fatigue life in seven steel bar types. Journal of Materials in Civil Engineering 2016;28:06015015. https://doi.org/10.1061/(ASCE)MT.1943-5533.0001476.

[1.45] Liu X, Bu Y, Wang Y, Guan Y. Ultra-low cyclic fatigue fracture of Q235B and Q345B steels and their butt welded joints. International Journal of Steel Structures 2022;22:430–49. https://doi.org/10.1007/s13296-022-00583-5.

[1.46] Weigand JM, Berman JW. Behavior of butt-welds and treatments using low-carbon steel under cyclic inelastic strains. J Constr Steel Res 2012;75:45–54. https://doi.org/10.1016/j.jcsr.2012.03.007.

[1.47] Dusicka P, Itani AM, Buckle IG. Cyclic response of plate steels under large inelastic strains. J Constr Steel Res 2007;63:156–64.

https://doi.org/10.1016/j.jcsr.2006.03.006.

[1.48] E 606-92: Standard practice for strain-controlled fatigue testing. ASTM international; 1998.

[1.49] Fang C, Wang W, Ji Y, Yam MCH. Superior low-cycle fatigue performance of iron-based SMA for seismic damping application. J Constr Steel Res 2021;184:106817. https://doi.org/10.1016/j.jcsr.2021.106817.

[1.50] Guo Y, Fang C, Zheng Y. Post-fire hysteretic and low-cycle fatigue behaviors of Q345 carbon steel. J Constr Steel Res 2021;187:106991. https://doi.org/10.1016/j.jcsr.2021.106991.

[1.51] Ono T, Kako Y, Sato A, Iwata M. A study on low cycle fatigue characteristics of metallic material. Journal of Structural and Construction Engineering (Transactions of AIJ) 2000;65:193–9. https://doi.org/10.3130/aijs.65.193_1.

Chapter 2 Determination of optimal round specimens under small and large tensile and compressive strains

Outline for Chapter 2

2.1. Introduction

When experiencing a large earthquake, the structural steel material (which controls the performance of the structural members) is subjected to large plastic strain [2.1, 2.2]. Conducting cyclic tests on the steel materials under large strain to better understand their behaviors is crucial for determining the material's suitability for high strain applications and seismic performance. However, performing such loading tests presents numerous challenges, e.g., due to buckling [2.3, 2.4].

To mitigate buckling of flat cross-section specimens tested under large strain cyclic loadings, buckling-restrained devices have been used in previous studies, e.g. [2.5–2.9]. When compared to round cross-section, flat specimens are thought to have less buckling resistance. Therefore, most studies employed round cross-section specimens cut from steel plates for the large strain cyclic loading tests.

In case of round specimens subjected to cyclic loading tests, standard practice for strain-controlled fatigue testing ASTM E606 [2.10] suggest a minimum reduced section to diameter *Le/D* ratio of 2.0. However, it has been reported that the ASTM E606 standard's recommended ratios must be modified to prevent plastic buckling under high compressive strain [2.11, 2.12]. For example, Dusicka et al. [2.12] discovered that buckling became more prominent at about 6% compressive strain (half amplitude) after a few tests with incremental amplitude cyclic loading using the recommended *Le*/*D* ratio. After changing the ratio to 1.25 and using radius of fillet to diameter *R*/*D* ratio of 2.0, the cyclic tests up to 7% could be performed. By using the specimens with the same *Le*/*D* ratio (1.25) but smaller *R*/*D* (=1.1 in [2.13], and =1.6 in [2.14]), the cyclic tests could be conducted up to 8%. Moreover, by employing the small *Le*/*D* ratios of 1.17 and 1.13, the cyclic loadings can be tested with large strain amplitudes extended up to 9% [2.15–2.17].

This suggests that not only the reduced section to diameter ratio (*Le*/*D*) but other proportional relationships, i.e., radius of fillet as well as the diameter of the gripping sections to diameter ratios, also have beneficial and detrimental effects on the specimen's performance.

These studies demonstrate that carrying out cyclic tests under large strain amplitudes without buckling presents numerous challenges. Rather than using standard test specimens, the ratios recommended by the standards had to be modified to determine the specimen shapes subjected to large strain. Besides, it is assumed that the *Le/D* ratio was set to 2.0 by ASTM E606 [2.10] with a margin such that the restricted area of the fillet section and the local elongation in the reduced section do not interfere with each other, thereby allowing stress to spread evenly at the *Le*. This means that *Le*/*D* ratios less than 2.0 may improve the buckling resistance while it may also have adverse effect, e.g. on the stress distribution which is difficult to observe in the tests. In addition to *Le*/*D*, the appropriate ratios of *R*/*D* and *Dg*/*D* should be strictly maintained to improve the buckling resistance of the specimen and to avoid the stress concentration which may arise at sections (from *R* to *Le*) where the cross-sectional area suddenly changes. However, the effect of these ratios on the buckling resistance and stress distribution of the specimen tested under large strains has not been thoroughly investigated thus far.

Given that the majority of previous studies have primarily focused on the effects of reduced section to diameter ratio, the effects of other proportional ratios (such as grip section, radius of fillet, reduced section to diameter) on the performances of specimens subjected to large strain will be also examined in this study. Since the stress distribution is difficult to observe in the tests, finite element analysis (FEA) will be also performed to investigate the influences of the specimen’s proportional ratios on stress and strain

distributions, neck, as well as buckling restraint. The primary goal is to determine optimal proportional ratios of the specimen for large amplitude tests. The findings of the study could lead to more numerical and experimental research on the steel materials (governing structural member performance) subjected to large plastic strain in order to improve understanding of seismic performance.

2.2. Analytical methods

2.2.1 Objective

To obtain optimal proportional ratios (Le/D, R/D) of round specimens subjected to both small and large strain tests considering the effect on strain as well as stress distributions, necking and buckling resistance.

2.2.2 Analytical parameters

The reduced section to diameter (*Le*/*D*) and radius of fillet to diameter (*R*/*D*) are deemed to have beneficial and detrimental effects on the performances of the specimen (see Fig. 2.2 for location of *Le*, *D*, *R*). As buckling due to compression is not of concern, ISO 6892-1 [2.18], ASTM E8/E8M [2.19], JIS Z 2201 [2.20] recommend *R/D* ratio with a minimum of 0.75, 0.8, 1.0 and *Le/D* ratio with a minimum of 5.5, 4.0 and 4.0, respectively, for the tensile specimens with round cross-sections. Large *Le*/*D* ratios are generally employed for a tensile specimen to assure the uniform stress distribution, necking, as well as fracture inside the reduced section.

Since buckling under compression concerns, standard practice for strain-controlled fatigue testing ASTM E606 [2.6] suggests a minimum *Le*/*D* ratio of 2.0 for round cross-section specimen. It is considered that *Le/D* ratio was set to 2.0 with a margin so that the restricted area of the *R* part and the local elongation do not interfere with each other, and therefore it allows stress to distribute freely throughout the reduced section. However, previous studies [2.11, 2.12] have indicated that the *Le*/*D* ratio should be reduced lower than the limit (minimum of 2.0) recommended by ASTM E606 [2.10] in order to conduct the cyclic loadings under large compressive strain. In addition to *Le*/*D*, *R*/*D* ratio may also influence the buckling resistance. For example, a low *R/D* ratio may improve the buckling resistance. Large *R*/*D*, on the other hand, is not ideal for high compressive strains,

as it increases the slenderness ratio to some extent and may contribute to premature buckling.

Nevertheless, the range of the appropriate specimen's proportional ratios (*Le*/*D* and *R*/*D*) are not known. In this study, *Le* and *R* are used as the parameters to investigate the influences of these ratios. According to the survey by previous study [2.21] as shown in Fig. 2.1, specimens with various *Le*/*D* (0.5 ~ 4.0) ratios were employed for the low-cycle fatigue tests. When testing under strain greater than 1%, specimens with ratios less than the ASTM E606 recommended value were mostly used to avoid buckling (Fig. 2.1). Besides, the effect of *R*/*D* was not elucidated. In this study, the *Le*/*D* ratio is reduced up to 0.25 to examine its influences over a broader range. To investigate the effect of *R*/*D*, the ratio is changed from 0.36 (narrow rounded edge at *R*) to 3.0 (large rounded edge at *R*), which also covers those recommended by the standards for the tensile tests [18–20]. Table 1 tabulates the analytical parameters, *Le*/*D* and *R*/*D* (hereafter, proportional ratios) considered in this study. Diameter of reduced section *D*, diameter of gripping section *Dg*, and overall length *L* are set as 17mm, 30mm, and 160mm, respectively (Fig. 2.2). It should be noted the specimen shape considered in this study is limited to the uniform-gage test section as shown in Fig. 2.2.

2.2.3 Analytical model

To investigate the effect of the specimen's proportional ratios, numerical analyses are performed on various specimen shapes imposed with tensile and compressive displacements. Revolution of solid element with element type of C3D8R (: An 8-node linear brick, reduced integration, hourglass control) is modelled using Abaqus/CAE 2021. Analytical model including section parameters (*Le*, *R*, *D*, *Dg*) and mesh sizes are shown in Fig. 2.2. In this study, only the results of the Z-plane view cut without gripping sections will be illustrated to examine what happens inside the specimen (although the complete model is analyzed). The specimen is fixed at the bottom, and the axial displacement is imposed at another top end to simulate the real test setup. The Poisson ratio of 0.3, Young modulus of 205000 N/mm^2 and true stress - plastic true strain of 400 N/mm^2 grade structural steel (Fig. 2.3) are input as the material property.

Since it is difficult to conduct the test under ideal conditions, initial imperfections in practice are unavoidable. Therefore, the initial imperfection is also included in the analytical model. Buckling analyses are first performed, and the obtained Eigenmode or buckling mode is used to introduce the initial imperfection in the main analytical models. The scale factor of the initial imperfection is taken as 0.1% of the overall length of the specimen (i.e., *L*/1000) which is in accordance with the ANSI/AISC 360-16 [2.22] for structural steel buildings for global imperfection (i.e., out-of-plane deformation, out-of-straightness of the column).

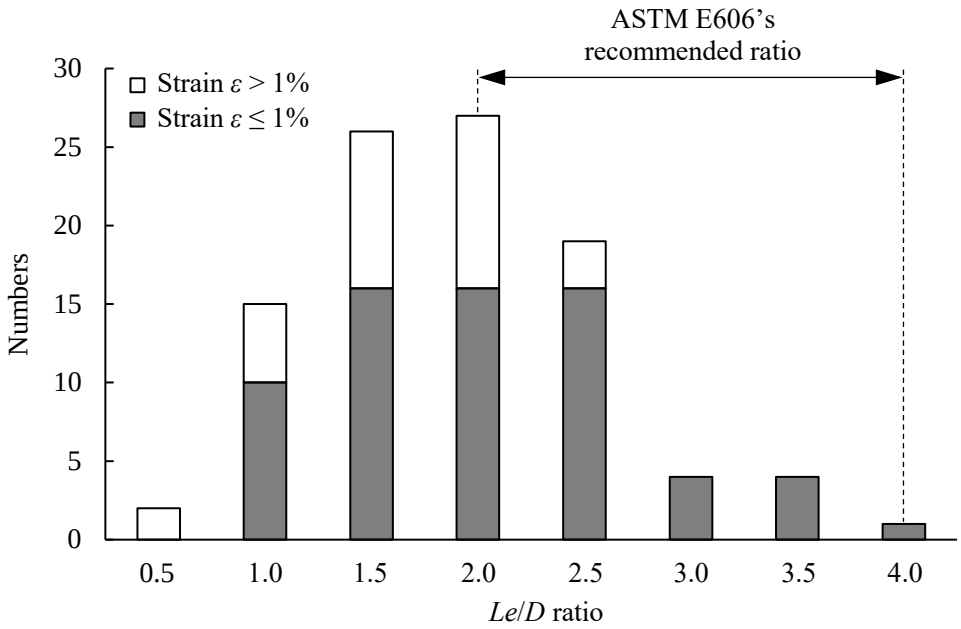

Fig. 2.1 Survey of specimens with different *Le*/*D* ratios used for low-cycle fatigue test (reprinted from [2.21]), effect of *R/D* was not examined

Table 1. Analytical parameters in this study (D = 17 mm)

Le/*D*	0.25	0.5	1.0	1.5	2.0	2.5	3.0	3.5	4.0
R/*D*	0.36	0.36	0.36	0.36	0.36	0.36	0.36	0.36	0.36
	0.5	0.5	0.5	0.5	0.5	0.5	0.5	0.5	0.5
	0.75	0.75	0.75	0.75	0.75	0.75	0.75	0.75	0.75
	1.0	1.0	1.0	1.0	1.0	1.0	1.0	1.0	1.0
	1.5	1.5	1.5	1.5	1.5	1.5	1.5	1.5	1.5
	2.0	2.0	2.0	2.0	2.0	2.0	2.0	2.0	2.0
	2.5	2.5	2.5	2.5	2.5	2.5	2.5	2.5	2.5
	3.0	3.0	3.0	3.0	3.0	3.0	3.0	3.0	3.0

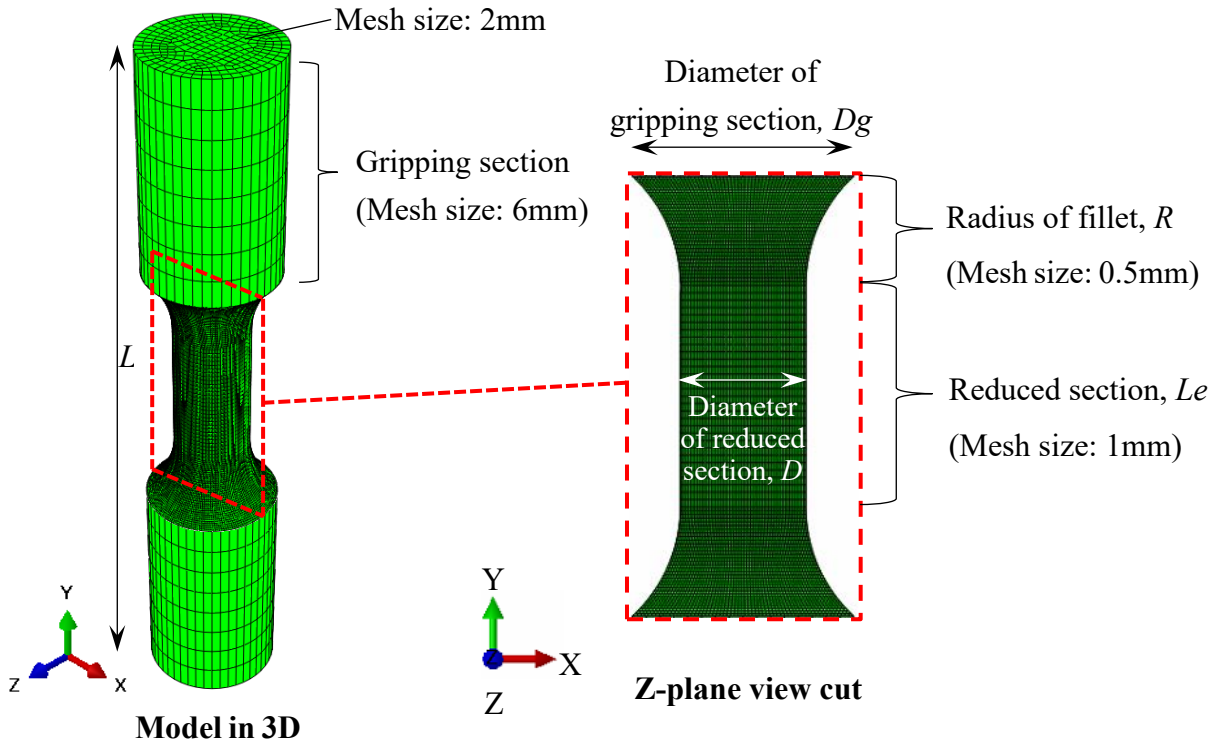

Fig. 2.2 Analytical model

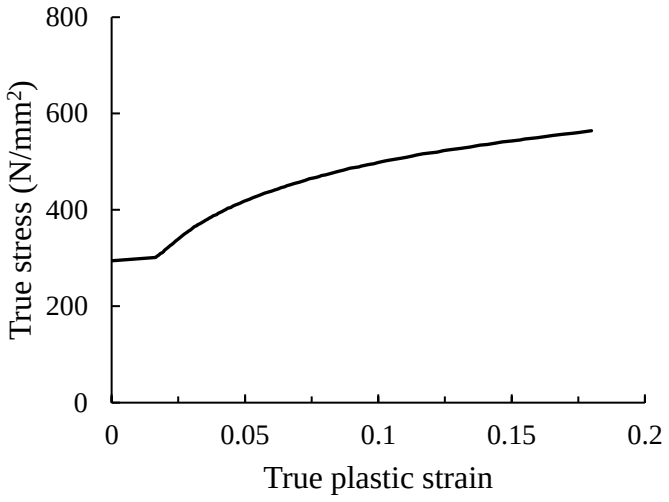

Fig. 2.3 True stress-true plastic strain used in Abaqus

2.3. Analytical results

2.3.1 Influence on strain and stress distributions

To examine the effects on the strain and stress distributions, the representative contours of different Le/D ratios when R/D = 2.0 and different R/D ratios when Le/D = 2.0 at yield strain and 6% true axial strain under tension or compression are illustrated in Figs. 2.4 and 2.5.

It is observed that the specimen with Le/D=4.0 already buckled at -6% true axial strain owing to its high Le/D ratio. Figs. 2.4 and 2.5 also show that for specimens with $Le/D \geq$ 0.25 (except for Le/D=4.0 at -6%) and $R/D \geq$ 0.36, the strain concentrates and stress spreads almost uniformly inside the reduced section Le. It should be noted that the asymmetric strain distribution is contributed by the initial imperfection. Besides, as shown in Fig. 2.5 the reduction in cross-section is also observed at the corner (R section) for the specimen with R/D=0.36 under compressive strain which may affect the deformation capacity under cyclic loadings. Nevertheless, the reduction in cross-section seems to be less significant when $R/D \geq$ 0.75.

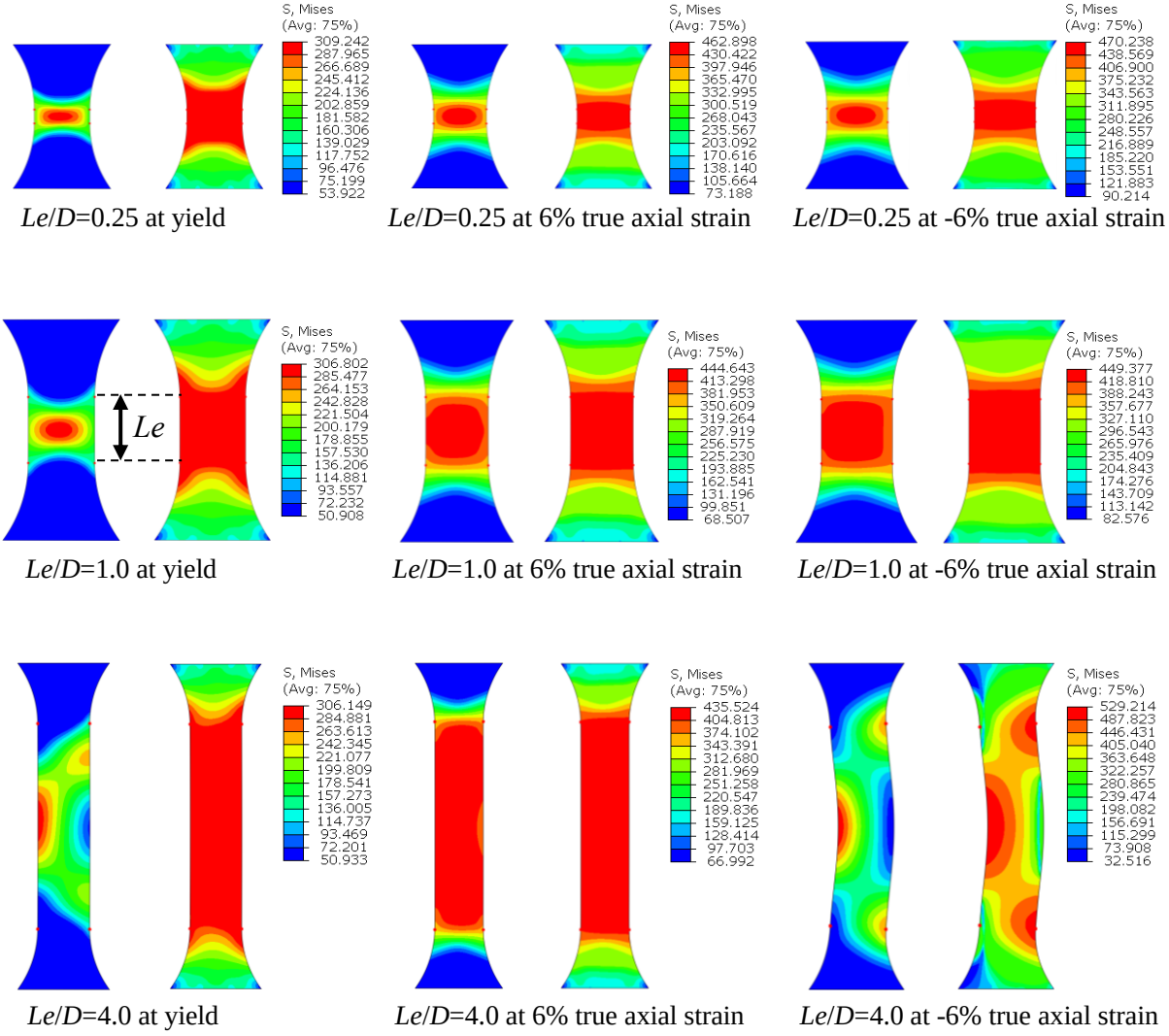

Le/*D*=0.25 at yield | *Le*/*D*=0.25 at 6% true axial strain | *Le*/*D*=0.25 at -6% true axial strain

Le/*D*=1.0 at yield | *Le*/*D*=1.0 at 6% true axial strain | *Le*/*D*=1.0 at -6% true axial strain

Le/*D*=4.0 at yield | *Le*/*D*=4.0 at 6% true axial strain | *Le*/*D*=4.0 at -6% true axial strain

Fig. 2.4 Strain and stress distributions of specimens with different *Le*/*D* (*R*/*D*=2.0)

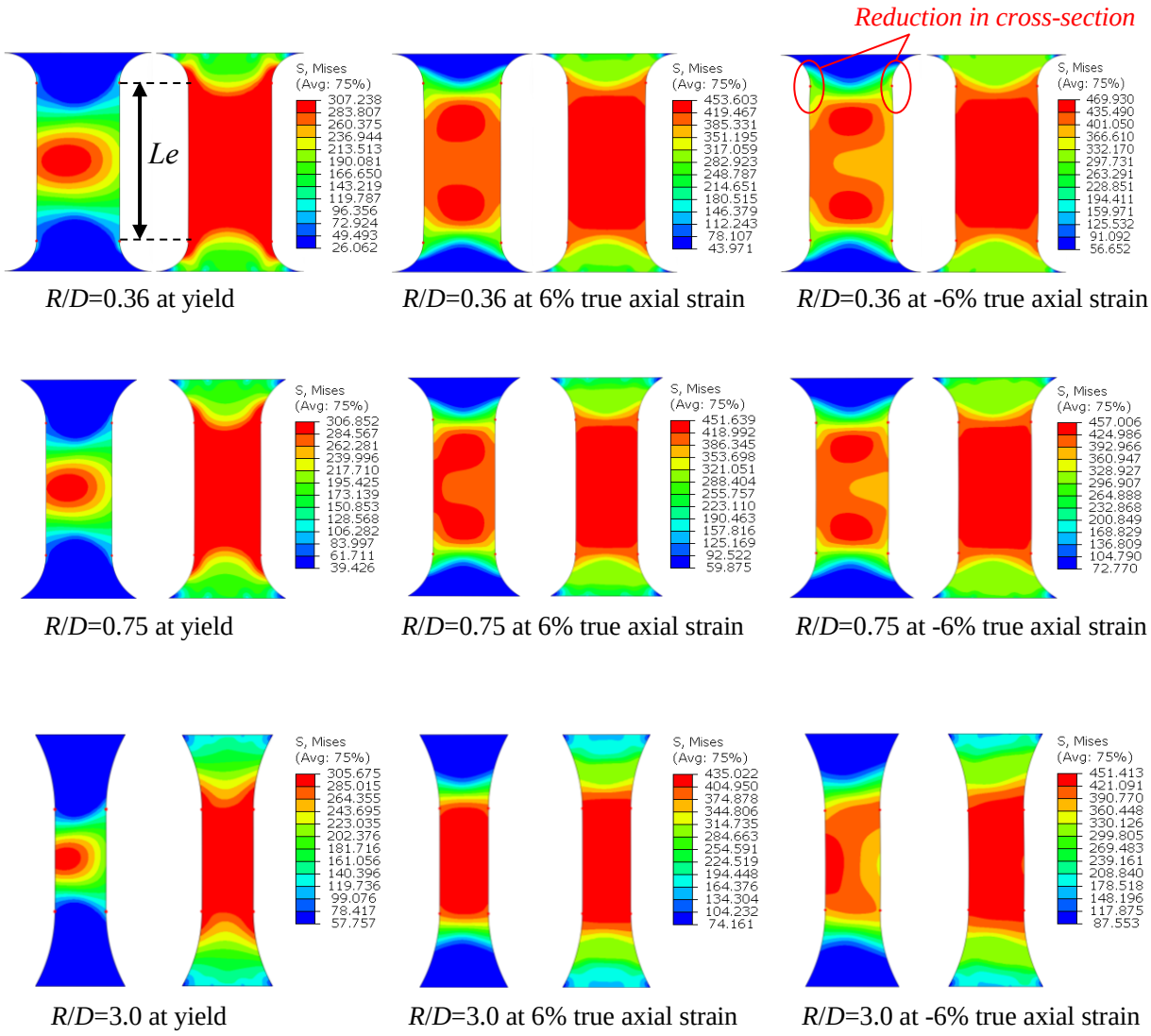

R/*D*=0.36 at yield | *R*/*D*=0.36 at 6% true axial strain | *R*/*D*=0.36 at -6% true axial strain

R/*D*=0.75 at yield | *R*/*D*=0.75 at 6% true axial strain | *R*/*D*=0.75 at -6% true axial strain

R/*D*=3.0 at yield | *R*/*D*=3.0 at 6% true axial strain | *R*/*D*=3.0 at -6% true axial strain

Fig. 2.5 Strain and stress distributions of specimens with different *R*/*D* (*Le*/*D*=2.0)

2.3.2 Influence on neck

This section investigates the effect on the neck of various proportional ratios. Previous studies, e.g., [2.23, 2.24] have indicated that specimens tested cyclically under large strains (3% or greater) tend to appear neck before fracture. In case of using specimen with short reduced section *Le* to expect high buckling resistance, there may be insufficient region for neck to fully form which may affect the plastic deformation capacity. So, it should be confirmed to what extent the *Le* can be shortened without affecting the localization of plastic strain (i.e., necking).

Fig. 2.6 depicts the necking configuration (shown with stress distribution) of representative specimens with varying *Le*/*D* and *R*/*D* at 75% reduction in area (%RA). This percentage was chosen in accordance with the previous report [2.25], which stated that the reduction in area of round specimens is typically between 75% and 80%. *Ln* in this figure indicates neck length. From Fig. 2.6, it is observed that the specimens with $Le/D \leq 2$ have symmetric neck region inside the reduced section *Le*.

Fig. 2.7 shows the relationship between neck length to reduced section (*Ln*/*Le*) ratio and reduced section to diameter (*Le*/*D*) ratio at different *R*/*D*. Here, *Ln*/*Le* greater than unity means that the neck length *Ln* is longer than the reduced section, indicating that necking region extend to the *R* section. This may affect the deformation capacity.

From Figs. 2.6 and 2.7, when $Le/D \geq 1.0$, neck can fully form inside the reduced section (since $Ln/Le \leq 1$), regardless of *R*/*D*. This could be the reason the ASTM E606 [2.6] and the tensile test standards [2.18–2.20] recommend the minimum *Le*/*D* ratios of 2.0 and 4.0, respectively. However, when $Le/D < 1.0$, neck length is longer than the reduced section ($Ln/Le > 1$). This finding is also consistent with Matic et al. [2.26], who indicated that *Le*/*D* must be 1.0 or greater in order for neck to fully develop inside the *Le* section.

Besides, it is also observed neck length tends to increase with the increase in *R*/*D*. The trend, on other hand, is less significant when *Le*/*D* ≥ 1.0.

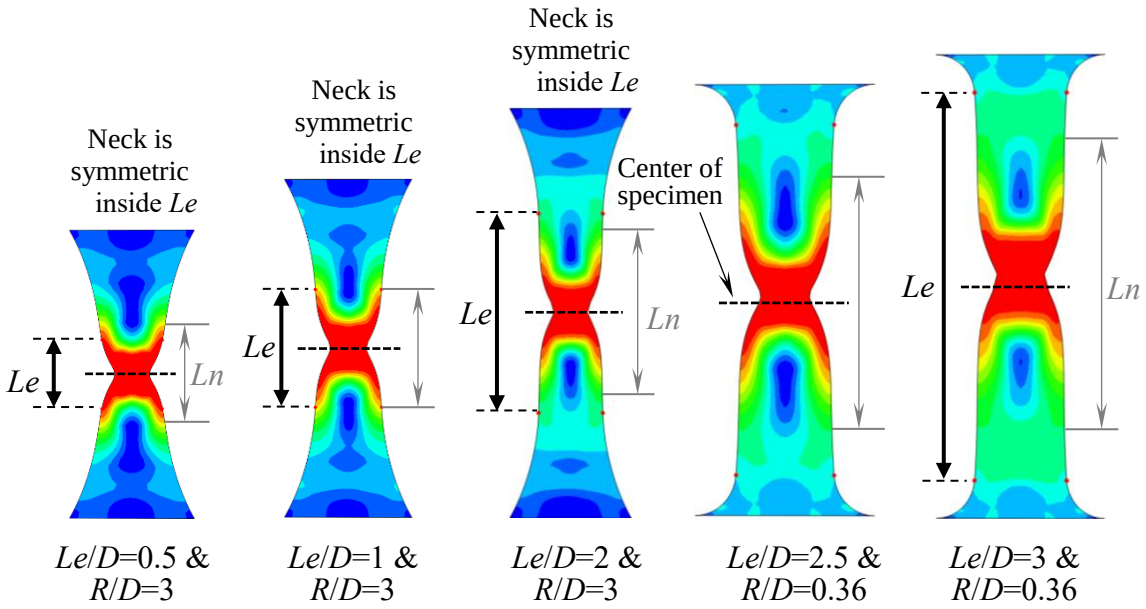

Fig. 2.6 Necking configuration (shown with stress distribution) of specimens with different *Le*/*D* and *R*/*D* ratios (*D* = 17 mm, *Le*: reduced section, *Ln*: neck length)

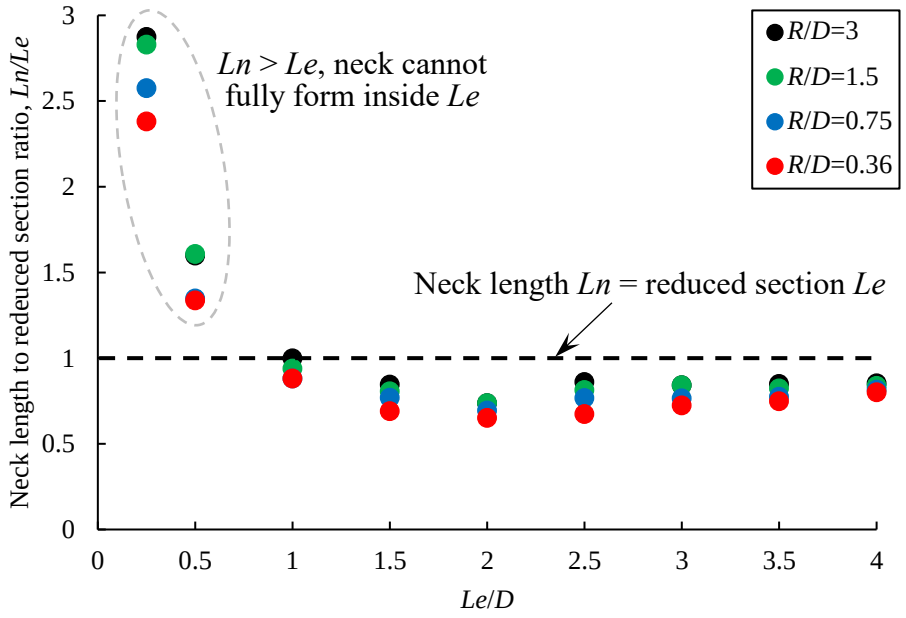

Fig. 2.7 Relationship between *Ln*/*Le* and *Le*/*D* (*D*=17mm, *R*/*D* = 0.36, 0.75, 1.5, 3)

2.3.3 Influence on buckling resistance

To examine the influence of the *Le*/*D* ratio on buckling resistance, the relationship between true axial strain at buckling and *Le*/*D* (with *R*/*D* of 0.36, 0.75, 1.5 and 3.0) is shown in Fig. 2.8. It is noticed that strain at buckling decreases as the *Le*/*D* ratio becomes higher. The buckling resistance, on the other hand, tends to be excellent when $Le/D \leq 2.0$. This trend is in accordance with the previous studies [2.11,2.12,2.21], which stated the ratio should be reduced lower than the limit (minimum of 2.0) recommended by ASTM E606 [2.10] in order to improve the buckling resistance.

This figure shows that specimens with larger *R*/*D* ratio tend to have lower buckling resistance. This is because large *R* contributes to large transitional region from *R* to *Le* section, resulting in high slenderness ratios and easy buckling. On the other hand, specimens with smaller *R*/*D* ratios tend to have higher buckling resistance. However, this small *R* may lead to reduction in cross-section (Fig. 2.4 for *R*/*D*=0.36 specimen) which may affect the cyclic deformation capacity. Therefore, this ratio should be 0.75 or larger to avoid reduction in cross-section at *R*. Besides, the relationship between *Le*/*D* and *R*/*D* at different strains (without buckling) is shown in Fig. 2.9. Specimens with lower *Le*/*D* and *R*/*D* ratios than the desired limit line can be tested at higher strains without buckling. It should be noted the limit lines are obtained from linear interpolation of the current available data.

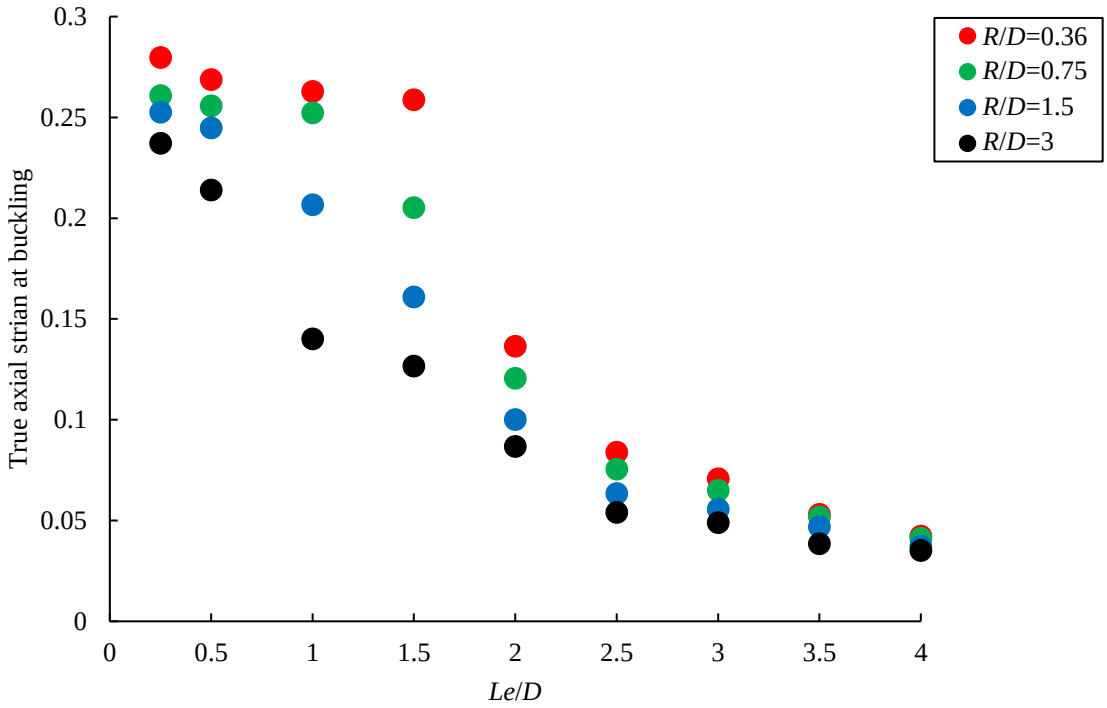

Fig. 2.8 Effect of *Le*/*D* on buckling resistance

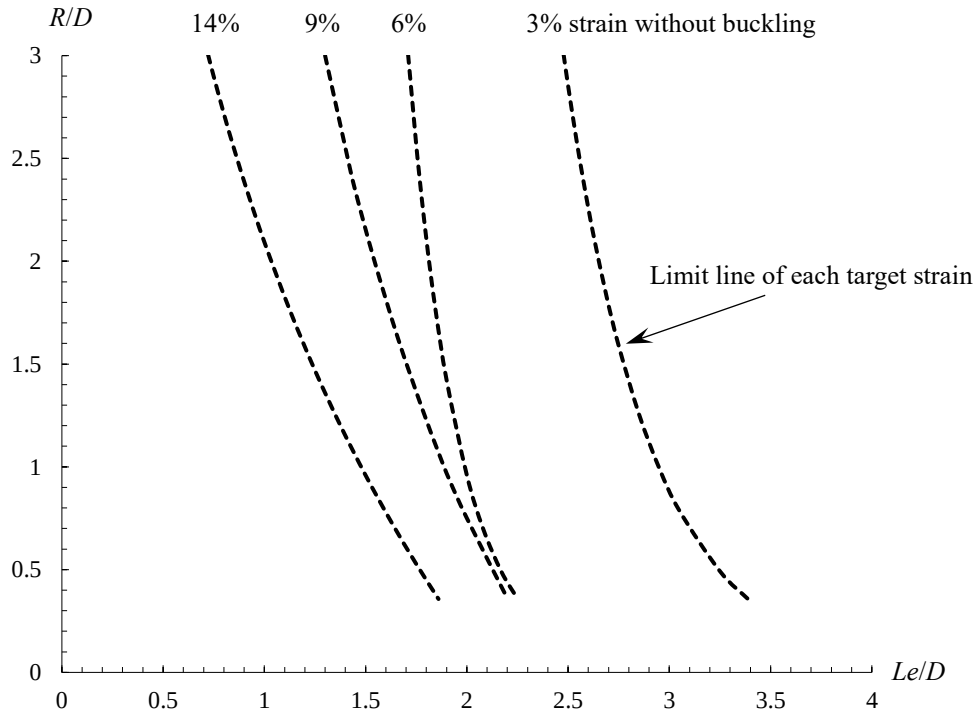

Fig. 2.9 Relationship between *Le*/*D* and *R*/*D*
at different target strains (without buckling)

2.4. Optimal proportional ratios

2.4.1 Optimal proportional ratios

The main objective of this section is to determine the optimal proportional ratios of specimens subjected to both small and large strain tests based on parameters considered in this study. The results in Section 2.3.1 indicate the stress distributes almost uniformly and strain concentrates inside the reduced section *Le* when $Le/D \geq 0.25$ and $R/D \geq 0.36$. Moreover, when $Le/D \leq 2.0$ buckling resistance is good (Section 2.3.3), and when $1.0 \leq Le/D < 2.5$ symmetric neck fully forms inside the reduced section, regardless of R/D (Section 2.3.2). By lowering the R/D ratio, the improvement of buckling resistance is confirmed (Section 2.3.3). However, the small ratio may also lead to reduction in cross-section at *R* under compressive strain which may affect the cyclic deformation capacity (Section 2.3.1). Therefore, this R/D ratio should be 0.75 or larger to avoid reduction in cross-section at *R* and simultaneously enhance the buckling performance.

Fig. 2.10 illustrates the optimal ratios of R/D and Le/D. The ratios of the specimens can be determined based on the target strains to be tested using the limit line of 9% strains without buckling. Since the specimen that can be tested under large strain is desired in this study, only the limit line of 9% strain is presented in the figure. It should be noted specimens with Le/D and R/D ratios lower than the desired limit line can be tested at higher strains without buckling.

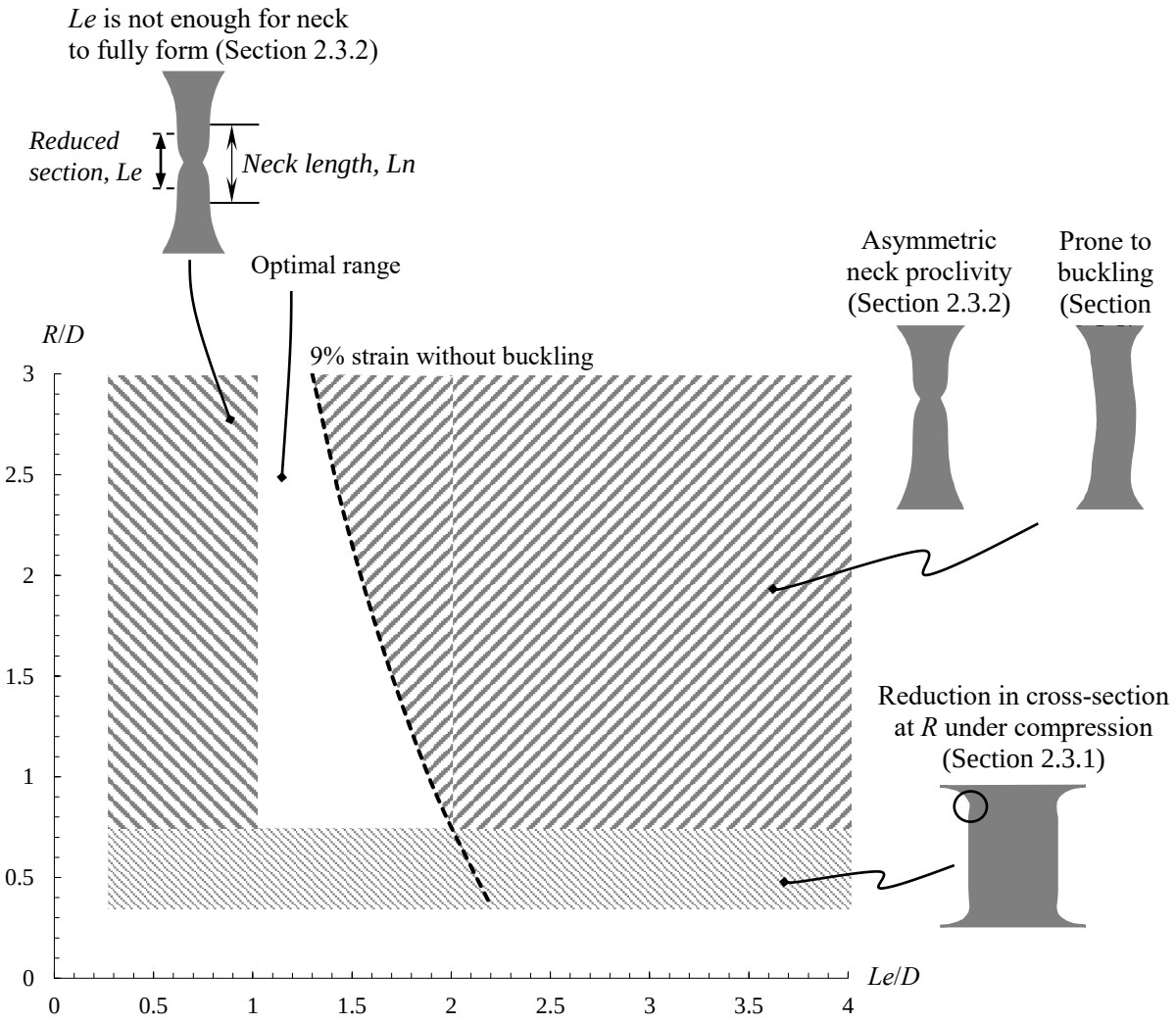

Fig. 2.10 Optimal proportional ratios for small and large strain tests

2.4.2 Validation of the proposed ratios

2.4.2.1 Material tests

To validate the proposed proportional ratios, cyclic tests on different specimen shapes were conducted. The specimens were machined from the 400 N/mm^2 grade steel plate followed the rolling direction into round coupons with the dimensions as shown in Table 2.2. These specimen shapes were chosen in such a way that it satisfies and fails to satisfy the proposed ratios.

To measure the axial strain of specimens, two strain gauges and an electronic extensometer with gauge length of *Le* were employed as shown in Fig. 2.11. Nominal stress was calculated by dividing the axial force measured by the load cell by the area of the reduced section's original cross-section. The nominal strain was calculated by dividing the reduced section's axial deformation by its original length. True stress (${}_t\sigma$) and true strain (${}_t\varepsilon$) were calculated from the nominal stress (${}_n\sigma$) and nominal strain (${}_n\varepsilon$) results under the assumption of a constant volume of the reduced section, and these parameters can be derived using Eqs. 2.1 and 2.2. The calibration coefficients of extensometer and load cells are 0.000558 (mm) and 500/50000 (kN), respectively.

$$ {}_t\sigma = {}_n\sigma(1 + {}_n\varepsilon) \tag{2.1} $$

$$ {}_t\varepsilon = \ln(1 + {}_n\varepsilon) \tag{2.2} $$

To reproduce the test result and validate the analytical method, FEA with Abaqus was also performed on these specimens, using the same analytical method described in Section 2.2. In Table 2.2, true axial strains at buckling of specimen from the analytical results are determined in such a way that the nominal strain ${}_n\varepsilon$ or the axial elongation

calculated from four controlling points (e.g. red dot marks in Fig. 2.13) at the edge of *Le* section and converted to true strain $_t\varepsilon$ using Eq. (2.2). Therefore, this strain corresponds to that measured in the test by the extensometer. The results in Table 2.2 indicate that for the same *Le*/*D*, specimens with lower *R*/*D* have higher buckling resistances. However, cracks as shown in Fig. 2.16 were also observed on Type B specimens (with low *R*/*D*) tested under 2% constant strain cyclic loading. These results are in line with the discussion in Section 2.4.1, which stated that a lower *R*/*D* ratio tends to enhance the buckling resistance, but a minimum of 0.75 should be used.

2.4.2.2 Validation of the FEA model

Nominal stress and nominal strain curves of Type A, B, C, D, F, G specimens obtained from monotonic tensile test and analytical results are shown in Fig. 2.13. Also, the comparison of cyclic tests and analytical results are illustrated in Fig. 2.14. Table 2.3 lists the kinematic hardening and isotropic hardening parameters used for cyclic analysis in Abaqus. These figures show that overall Abaqus can well reproduce the stress – strain curves if compared to the test result. Furthermore, Table 2.2 indicates that the strains at buckling obtained from the test and analysis are found to be in good agreement. Also, the comparison of buckling configurations in Fig. 2.12 suggests that Abaqus can reproduce the result well. Therefore, the analytical model and results are said to be validated. (For further discussion on influences of element types and mesh sizes, refer to Appendix 4).

2.4.2.3 Validation of the proposed ratios and limit strains

2.4.2.3.1 Effect of initial imperfection on monotonic compression and cyclic loadings

The specimen under monotonic compression is thought to be more prone to buckling than the specimen under (tension-compression and compression-tension) cyclic loadings. This is because the specimen under cyclic loading is compressed with smaller imperfections due to the tensile strain applied to the specimens, which may help reduce the imperfection. To investigate the influences of initial imperfection, Type A and B were employed to perform analyses with monotonic compression and tension-compression cyclic loadings. Data of Type G is also used as input for Type A and B specimens to investigate the effect of stress-strain relationship. Despite the minor differences due to the effect of stress-strain curves, the analytical results in Fig. 2.15 show that tension-compression is less likely to buckle than monotonic compression. In this regard, it can be said that pulling the specimen may have the effect of reducing the initial imperfection. This also implies that monotonic compression analyses can be used to reasonably investigate the optimal proportional ratios for large amplitude cyclic tests. To demonstrate this, the proposed ratios are compared in the following section to the analytical and test results obtained from the cyclic loadings.

2.4.2.3.2 Comparison with cyclic loadings

To validate the limit strain line and proposed ratios, the specimens with different geometries from previous studies [2.12–2.16, 2.24, 2.27] are also employed for comparison. Specimens' proportional ratios from previous studies are listed in Table 2.4. Fig. 2.17 shows the comparison of specimen with different proportional ratios. The (◆, ■, ●) marks indicate the results of previous studies, this study and analyses. The red marks in Fig. 2.17 are lower than the limit strain line, but it is not stated in the literature whether the specimen buckles at higher strain. From this figure, it can be seen that the proposed limit strain line and optimal ratios correspond well with the database. This implies that

the optimal specimen geometry under cyclic loading can be reasonably examined in a monotonic analysis considering initial imperfections. Also, the proposed limit strain line and proportional ratios can be said to be validated using the specimens with different geometries considered in this study.

Besides, the previous studies which conducted LCF tests using *Le*/*D* of 0.5, 1.0, 1.5 and 2.0 (with the maximum 2% constant strain amplitude) have indicated that the LCF performances of specimens with *Le*/*D* = 1.5 and 2.0 are similar and concluded that *Le*/*D* of 1.5 or greater should be employed in order to obtain the correct fatigue behavior[2.21]. Also, given the measurable range of the extensometer, Type G with *Le*/*D*=1.76 and *R*/*D* = 1.18 will be used for further discussion on the low-cycle fatigue (LCF) and extremely LCF (ELCF) performances of various structural steels in the following chapters.

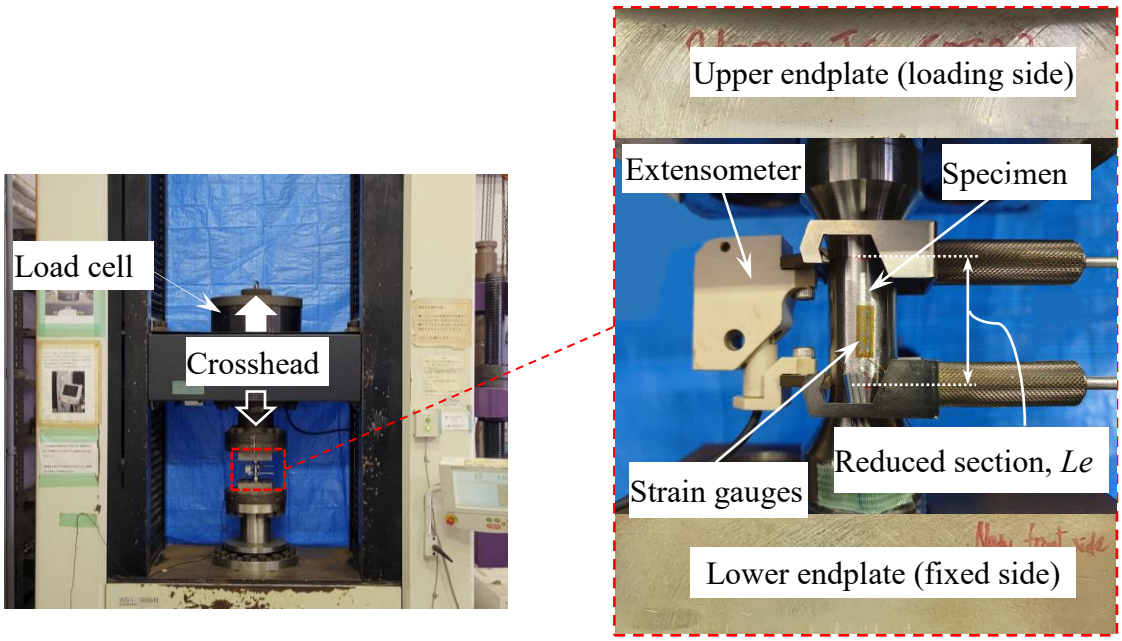

Fig. 2.11 Test setup

Table 2.2 Dimension of specimens and true axial strains at buckling of each specimen

Specimen name	*D* (mm)	*Le*/*D* ratio	*R*/*D* ratio	True axial strains at buckling (test) [No buckling]	True axial strains at buckling (FEA)
Type A_3%※	14	2.14	1.43	4.5%	4.14%
Type B_9%	14	2.14	0.36	10.5%	9.65%
Type C_2%	14	2.86	1.43	3%	3.11%
Type D_3%	14	2.86	0.36	4%	3.53%
Type F_12%	11.5	1.30	1.74	[12%]	20.1%
Type G_12%	17	1.76	1.18	[12%]	14.2%

※Type A_3% refers to specimen name_tested strain (without buckling)

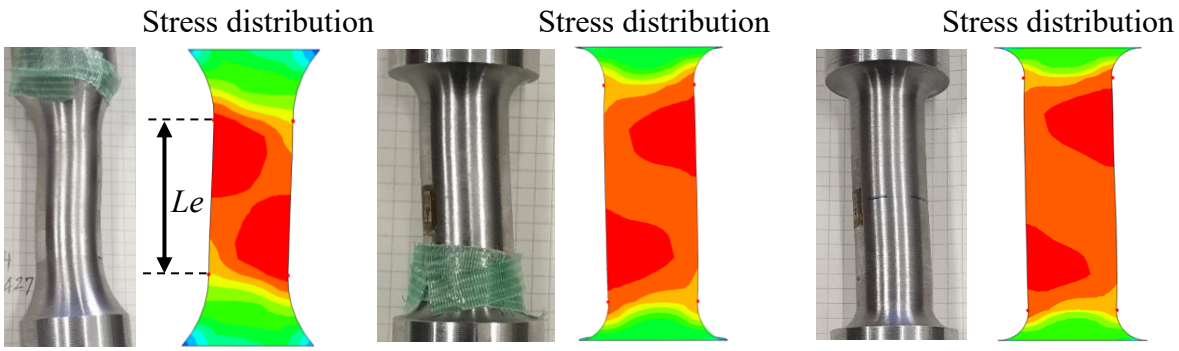

Fig. 2.12 Comparison of buckling configurations

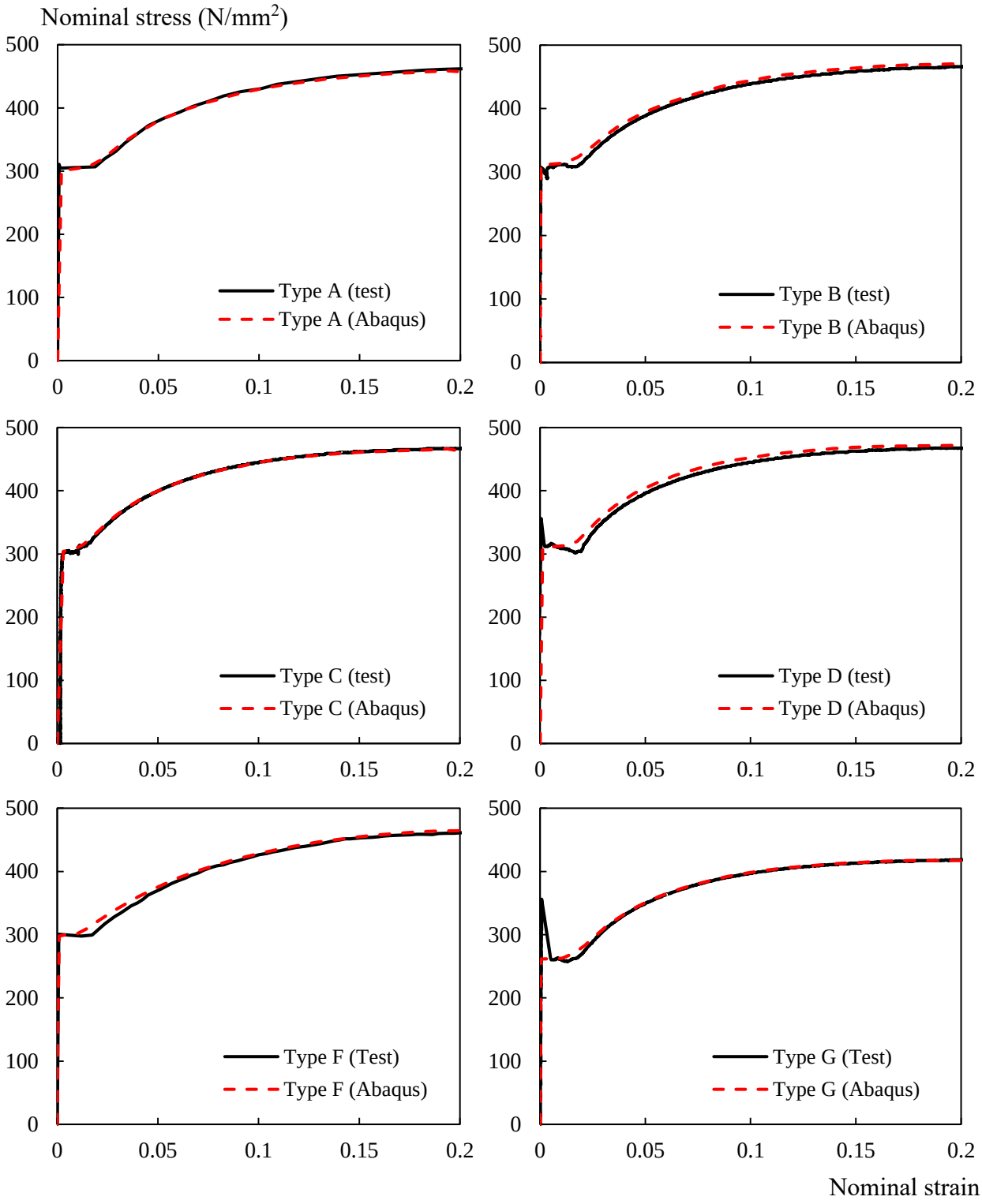

Fig. 2.13 Comparison of nominal stress-nominal strain curves up to 20% nominal strain from test and analytical results

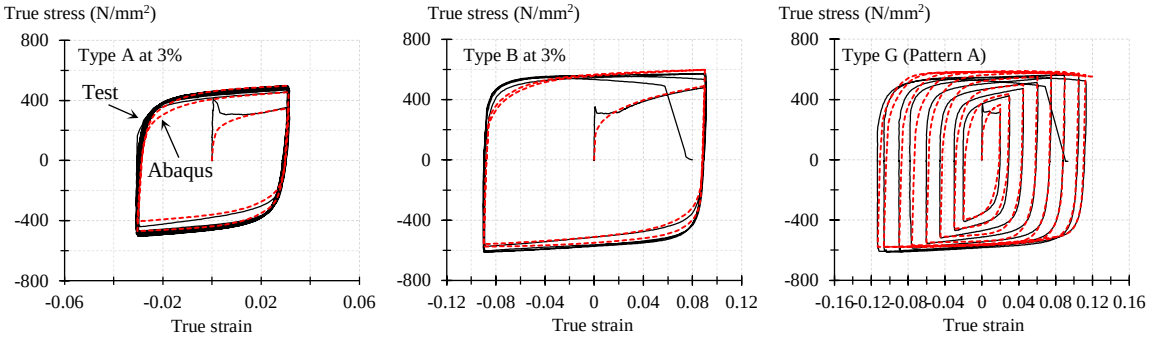

Fig. 2.14 Comparison of true stress-true strain curves from test and analytical results

Table 2.3 Kinematic hardening and isotropic hardening used in Abaqus

Kinematic hardening parameters used in Abaqus

Specimen	Yield Stress at Zero Plastic Strain	Kinematic hard	Gamma 1	Kinematic hard Parameter C2	Gamma 2	Kinematic hard Parameter C3	Gamma 3
Type A (4%)	97.1	184218	1881	14373	160	532	0
Type B (9%)	164	28003	457	6479	71	360	0
Type G (PatternA)	167	33640	310	10540	134	125	0

Isotropic hardening parameters used in Abaqus

Specimen	Equiv Sress	Q-infinity	Hardening Param b
Type A (4%)	97.1	230	10
Type B (9%)	164	271	10
Type G (PatternA)	167	235.1	4.47

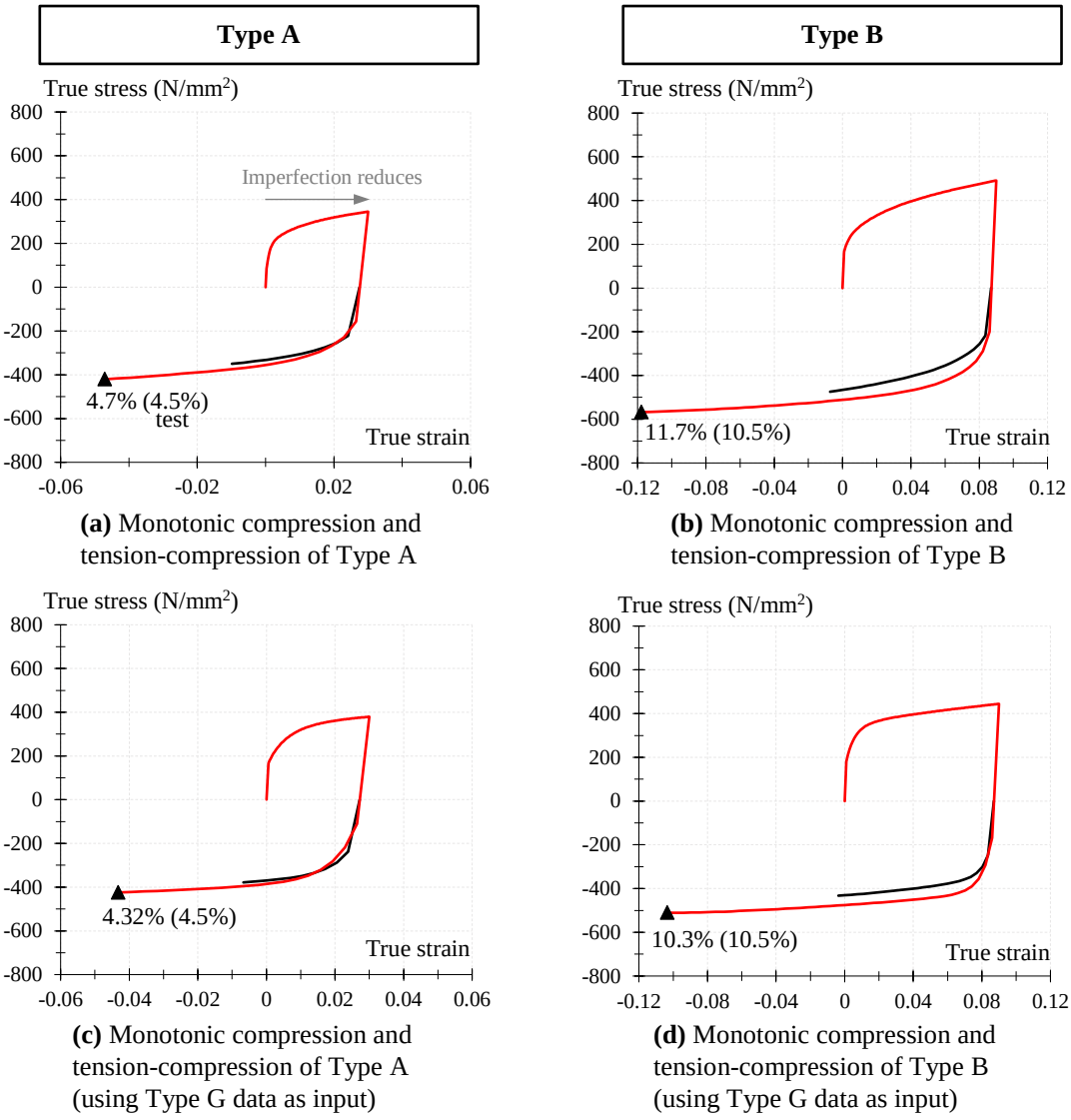

(a) Monotonic compression and tension-compression of Type A

(b) Monotonic compression and tension-compression of Type B

(c) Monotonic compression and tension-compression of Type A (using Type G data as input)

(d) Monotonic compression and tension-compression of Type B (using Type G data as input)

Fig. 2.15 Effect of initial imperfection on monotonic compression and cyclic loading

Table 2.4 Specimens' proportional ratios from previous studies

Specimen name	*D* (mm)	*Le*/*D* ratio	*R*/*D* ratio	Tested strain	Steel materials used	Literatures
[2.27] _3.5%※	14	2.14	1.79	3.5%	SN400B, SN490B, LYP100, HT780, SCM435, SUS304, A6061-T6	[2.27]
[2.24] _6%	13	1.08	1.92	6%	LY100, LY160, LY225	[2.24]
[2.12] _7%	20	1.25	2.0	7%	GR345, HPS485, HT440, LYP100, LYP225	[2.12]
[2.28] _8%	15	1.73	1.67	8%	350WT (CSA)	[2.28]
[2.14] _8%	12	1.25	1.67	8%	LYP100	[2.14]
[2.13] _8%	10	1.25	1.1	8%	Q235B, Q345B	[2.13]
[2.15] _9%	15	1.13	2.0	9%	Q235, Fe-SMA	[2.15]
[2.16] _9%	12	1.17	2.0	9%	Q345	[2.16]
[2.11] _9.5%	14	1.14	2.07	9.5%	Q235B	[2.11]

※ [2.27] _3.5% refers to literature _tested true axial strain (without buckling)

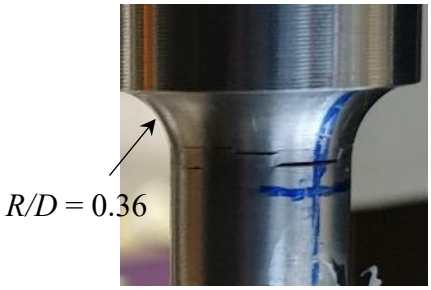

Fig. 2.16 Cracks at the corner of Type B under 2% constant amplitude cyclic tests

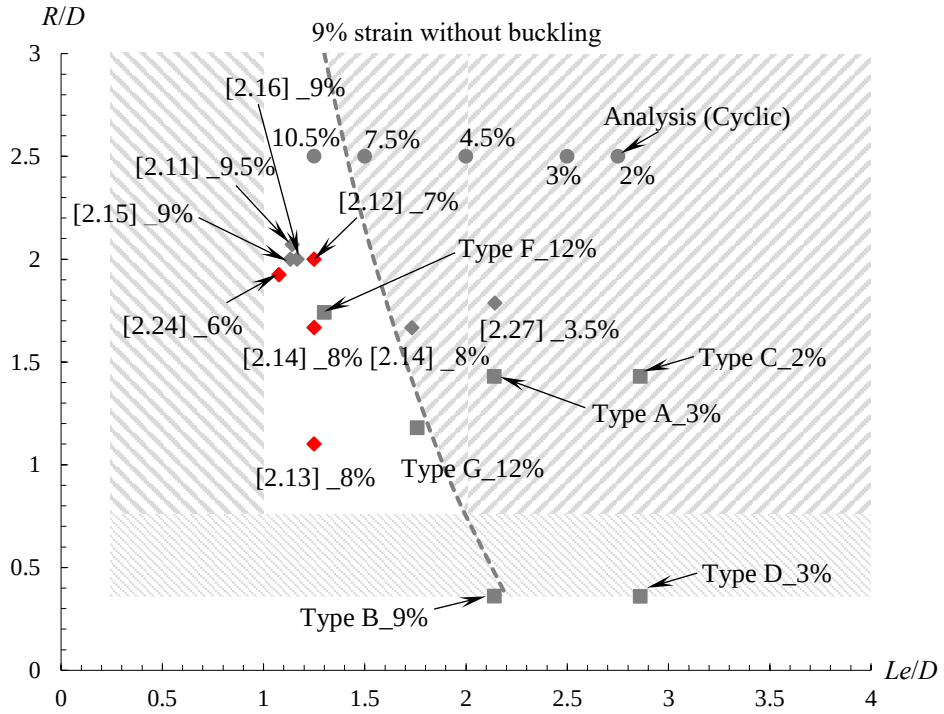

Fig. 2.17 Comparison of specimens with different proportional ratios

2.5. Summary

This chapter examined the optimal round specimens under small and large tensile and compressive strains. The following is the main conclusions.

- For specimens with $Le/D \geq 1.0$ and $R/D \geq 0.36$, the strain concentrates and stress distribute almost uniformly inside the reduced section *Le*.
- When $Le/D \geq 1.0$, neck can fully form inside the reduced section (since $Ln/Le \leq 1$), regardless of R/D. However, when $Le/D < 1.0$, neck length is longer than the reduced section ($Ln/Le > 1$). Besides, it is also observed neck length tends to increase with the increase in R/D. The trend, on other hand, is less significant when $Le/D \geq 1.0$.
- As Le/D ratios increase the bucking resistance of the specimen decreases. Specimens with small R/D ratios tend to have higher buckling resistance. Nevertheless, small R/D (< 0.75) may also lead to reduction in cross section at the corner under compressive strain which may affect the deformation capacity.
- Given stress & strain distributions, reduction in cross-section at *R*, neck and buckling resistance, the optimal range of Le/D and R/D ratios with the limit strain line of 9% are proposed. Consequently, the applicability of the proposed ratios and limit strain is also confirmed according to cyclic analyses, several material tests (using Type A-G specimens) and specimen shapes employed in previous studies.

Given the measurable range of the extensometer, Type G will be used for further discussion on the low-cycle fatigue (LCF) and extremely LCF (ELCF) performances of various structural steels in the following chapters.

References for chapter 2

[2.1] Shi G, Wang M, Bai Y, Wang F, Shi Y, Wang Y. Experimental and modeling study of high-strength structural steel under cyclic loading. Eng Struct 2012;37:1–13. https://doi.org/10.1016/j.engstruct.2011.12.018.

[2.2] Jia C, Shao Y, Guo L, Liu H. Cyclic behavior and constitutive model of high strength low alloy steel plate. Eng Struct 2020;217:110798. https://doi.org/10.1016/J.ENGSTRUCT.2020.110798.

[2.3] Dodd LL, Restrepo-Posada JI. Model for predicting cyclic behavior of reinforcing steel. Journal of Structural Engineering (United States) 1995;121:433–45. https://doi.org/10.1061/(ASCE)0733-9445(1995)121:3(433).

[2.4] Smith RW, Hirschberg MH, Manson SS. Fatigue behavior of materials under strain cycling in low and intermediate life range. NASA TND-1574 1963:57.

[2.5] Nip KH, Gardner L, Davies CM, Elghazouli AY. Extremely low cycle fatigue tests on structural carbon steel and stainless steel. J Constr Steel Res 2010;66:96–110. https://doi.org/10.1016/J.JCSR.2009.08.004.

[2.6] Weigand JM, Berman JW. Behavior of butt-welds and treatments using low-carbon steel under cyclic inelastic strains. J Constr Steel Res 2012;75:45–54. https://doi.org/10.1016/j.jcsr.2012.03.007.

[2.7] Zhou F, Li L. Experimental study on hysteretic behavior of structural stainless steels under cyclic loading. J Constr Steel Res 2016. https://doi.org/10.1016/j.jcsr.2016.03.006.

[2.8] Chen L, Yao X, Sun Z, Wang D. Study seismic performance of duplex stainless steel under large strain amplitude by cyclic loading test. J Constr Steel Res 2022;194:107332. https://doi.org/10.1016/j.jcsr.2022.107332.

[2.9] Zheng S, Zhou F, Cheng J, Li HT, Rong R. Experimental study on cyclic hardening characteristics of structural stainless steels. J Constr Steel Res 2022;191:107196. https://doi.org/10.1016/J.JCSR.2022.107196.

[2.10] E 606-92: Standard practice for strain-controlled fatigue testing. ASTM international; 1998.

[2.11] Zhong Y-L, Wang Y-B, Xiang Y, Li G-Q. Constitutive model for cyclic behavior of mild steel under various strain amplitudes. J Constr Steel Res 2022;196:107396.

https://doi.org/10.1016/J.JCSR.2022.107396.

[2.12] Dusicka P, Itani AM, Buckle IG. Cyclic response of plate steels under large inelastic strains. J Constr Steel Res 2007;63:156–64. https://doi.org/10.1016/j.jcsr.2006.03.006.

[2.13] Liu X, Bu Y, Wang Y, Guan Y. Ultra-low cyclic fatigue fracture of Q235B and Q345B steels and their butt welded joints. International Journal of Steel Structures 2022;22:430–49. https://doi.org/10.1007/s13296-022-00583-5.

[2.14] He Q, Chen Y, Ke K, Yam MCH, Wang W. Experiment and constitutive modeling on cyclic plasticity behavior of LYP100 under large strain range. Constr Build Mater 2019;202:507–21. https://doi.org/10.1016/j.conbuildmat.2018.12.146.

[2.15] Fang C, Wang W, Ji Y, Yam MCH. Superior low-cycle fatigue performance of iron-based SMA for seismic damping application. J Constr Steel Res 2021;184:106817. https://doi.org/10.1016/j.jcsr.2021.106817.

[2.16] Guo Y, Fang C, Zheng Y. Post-fire hysteretic and low-cycle fatigue behaviors of Q345 carbon steel. J Constr Steel Res 2021;187:106991. https://doi.org/10.1016/j.jcsr.2021.106991.

[2.17] Zhou F, Chen Y, Wu Q. Dependence of the cyclic response of structural steel on loading history under large inelastic strains. J Constr Steel Res 2015;104:64–73. https://doi.org/10.1016/j.jcsr.2014.09.019.

[2.18] ISO 6892-1 Metallic materials - Tensile testing - Part 1: Method of test at room temperature 2009.

[2.19] E8/E8M-13a: Standard Test Methods for Tension Testing of Metallic Materials. ASTM international; 2013.

[2.20] JIS (Japanese Industrial Standards) Z 2201 - Test pieces for tensile test for metallic materials 1998.

[2.21] Morino K, Nisitani H, Nishimura F, Beppu T. Problems Related to the Shape of Central Part of Specimens on Low Cycle Fatigue Behavior under Axial Loading and the Measures. TRANSACTIONS OF THE JAPAN SOCIETY OF MECHANICAL ENGINEERS Series A 1994;60:682–9. https://doi.org/10.1299/kikaia.60.682.

[2.22] ANSI/AISC 360-16: Specification for Structural Steel Buildings. American

Institute of Steel Construction; 2016.

[2.23] Yamada S, Touch T, Jiao Y, Ishida T, Kishiki S. Deformation capacity of 400 N/mm^2 class structural steel under extremely large strains. J Constr Steel Res 2021;182:106678. https://doi.org/10.1016/j.jcsr.2021.106678.

[2.24] Yang L, Gao Y, Shi G, Wang X, Bai Y. Low cycle fatigue property and fracture behavior of low yield point steels. Constr Build Mater 2018;165:688–96. https://doi.org/10.1016/j.conbuildmat.2018.01.075.

[2.25] Isao N, Akiyoshi M, Yoshihiro I, Tadashi I, Mitsumasa F, Kazuyoshi F, et al. Effect of dimensions of specimen on elongation of structural steel (joint research report on the elongation of structural steel for determination of standard strength). Technical Note of National Institute for Land and Infrastructure Management 2011:1–109.

[2.26] Matic P, Kirby GC, Jolles MI. The relationship of tensile specimen size and geometry effects to unique constitutive parameters for ductile materials. Proc R Soc Lond A Math Phys Sci 1988;417:309–33. https://doi.org/10.1098/rspa.1988.0063.

[2.27] Ono T, Kako Y, Sato A, Iwata M. A study on low cycle fatigue characteristics of metallic material. Journal of Structural and Construction Engineering (Transactions of AIJ) 2000;65:193–9. https://doi.org/10.3130/aijs.65.193_1.

[2.28] Dehghani M, Tremblay R, Leclerc M. Fatigue failure of 350WT steel under large-strain seismic loading at room and subfreezing temperatures. Constr Build Mater 2017;145:602–18. https://doi.org/10.1016/j.conbuildmat.2017.03.183.

Chapter 3 Low and Extremely Low Cycle Fatigue Performances of Structural Steels with Different Strengths

Outline for Chapter 3

3.1. Introduction

To date, research studies e.g., [3.1–3.5] on the low cycle fatigue (LCF) performances of steel materials have been extensively conducted. However, only the limited strain amplitudes of 3.5% or smaller were studied for LCF performance of various structural steels used in Japan [3.6]. When subjected to intense lateral loads, such as those generated by severe earthquakes, steel members may experience significant strain amplitudes [3.7–3.11] and fracture after an extremely low number of cycles (in the order of 10 cycles) which this fracture could be categorized in extremely LCF (ELCF) [3.12–3.15]. Besides, the experimental investigations by researchers [3.16–3.18] after the great Hanshin-Awaji earthquake in 1995 have indicated that steel members may undergo 8% or greater during the earthquake. In other words, prior studies of the ELCF behaviors of structural steel at even larger strain amplitudes have been limited.

Therefore, the cyclic deformation capacities that ranged from LCF to ELCF regimes in a continuous manner have not been modeled comprehensively. One of the possible reasons for the lack of these types of experimental studies could be attributed to the design of a test specimen that can avoid stress concentrations at the edge of the effective length section and at the same time can also prevent premature buckling until it reaches fracture when it is subjected to large compressive strain. The buckling issue for specimen tested under large compressive strain was also pointed out in the previous studies [3.19, 3.20].

By using the appropriate specimen shape discussed in Chapter 2, LCF tests including large strain amplitudes could be conducted. In this chapter, to investigate LCF and ELCF performances of various structural steels, cyclic loading tests were performed on steel with different grades which cover both small (2%) and large (12%) strain amplitudes.

The structure of this chapter is followed by first the test parameters such as steel

materials, strain amplitudes and loading conditions will be introduced in Section 3.2. Next, in Section 3.3, the hysteretic curves when illustrated in the nominal and true stress-strain curves are compared followed by the true stress-true strain curves of different structural steels. The LCF performance of SS400 steel is then compared with the previous result to validate this study's test data. After validation, the LCF performance with large plastic strains is investigated further, taking the effects of initial loading excursions into account. Consequently, the effect of the different structural steels on LCF and ELCF performances was also examined, and the LCF equation of the structural steels is proposed. In addition to that until fracture, the deformation capacity of steel materials up to the ultimate point is also investigated. The equation for evaluating the deformation capacity up to ultimate point is proposed and validated using the result from variable amplitude cyclic loading tests. Finally, the conclusions of the chapter are summarized.

3.2. Test parameters

3.2.1 Steel materials

SS400 is a hot-rolled carbon steel used in common structures and comparable to ASTM A36. SM490A is a hot rolled high-strength low-alloy steel to be used for welded structures and comparable to high-strength low-alloy steel ASTM A572 grade 50. High-strength low-alloy steel SA440C is heat-treated steel developed with sufficient ductility and weldability and especially used for tall buildings in Japan. SA440C is comparable to high-strength low-alloy steel ASTM A709 grade 65. Although SS400, SM490A, SA440C structural steels have different strength levels, their chemical compositions are not so different. Table 3.1 presents the chemical compositions and mechanical properties of these steels which were obtained from mill certificates, monotonic tensile tests using Type G, and specifications. The monotonic stress-strain relationships of Type G are depicted in Fig. 3.1. The solid circles indicate the points of uniform elongations (strains corresponding to tensile strength). The yield strength of SA440C is the stress when the residual strain equals 0.2% after unloading. The chemical compositions and mechanical properties of Type A and B are shown in Table 3.2. The tensile stress-strain curves of Type A and B are shown in Fig. 3.2. It should be noted that Type A was the first test in the series, and the extensometer was removed when the specimen reached tensile strength due to concerns that it would be broken if left in place until fracture.

3.2.2 Loading conditions

To obtain test data of SS400, SM490A and SA440C in the LCF and ELCF regions, constant-amplitude strain-controlled cyclic loading tests were conducted. In the test, strain amplitudes (ε) were set as $\pm$2%, $\pm$3%, $\pm$4.5%, $\pm$6%, $\pm$7.5%, $\pm$9%, $\pm$10.5%, $\pm$11.25%, and $\pm$12%. In addition, in the event of an earthquake, either a large tensile or a large compressive strain may be applied. Therefore, both tensile and compressive excursions were set in the tests. Considering the scatter of test results and the effect of the initial loading directions on the cyclic deformation capacity of each steel, two series of tension–compression cyclic tests and one series of compression–tension cyclic tests were conducted. Table 3.3 presents a list of steels and loading conditions used in this study. In Table 3.3, T and C indicate the tension–compression and compression–tension cyclic tests, respectively. Here, T2 refers to the second tension–compression cyclic test, and T2' indicates the second steel lot of SS400.

Table 3.1 Mechanical properties and chemical compositions of SS400, SM490A, and SA440C

Steels		SS400 T	SS400 T2'	SM490A T	SA440C T
Mechanical properties	σ_y, N/mm^2	347 (≥ 235)	374 (≥ 235)	368 (≥ 325)	475 (440 - 540)
	σ_u, N/mm^2	451 (400 - 510)	452 (400 - 510)	529 (490 – 610)	634 (590 - 740)
	ε_u, %	22.1	23.8	16.7	8.4
Chemical compositions (%)	C	0.13	0.13	0.14 (≤ 0.20)	0.08 (≤ 0.18)
	Si	0.21	0.2	0.25 (≤ 0.55)	0.02 (≤ 0.55)
	Mn	0.55	0.49	1.42 (≤ 1.65)	1.49 (≤ 1.60)
	P	0.021 (≤ 0.05)	0.017 (≤ 0.05)	0.014 (≤ 0.035)	0.003 (≤ 0.02)
	S	0.019 (≤ 0.05)	0.021 (≤ 0.05)	0.005 (≤ 0.035)	0.001 (≤ 0.008)

Note: Numbers in the bracket () indicate the values stipulated by the specification JIS G 3101 [3.21] for SS400, JIS G 3106 [3.22] for SM490A, and JISF [3.23] for SA440C with the thickness of 16-40mm. σ_y and σ_u indicate the yield and tensile strengths, respectively. ε_u defines the nominal strain at the tensile strength (known as uniform elongation).

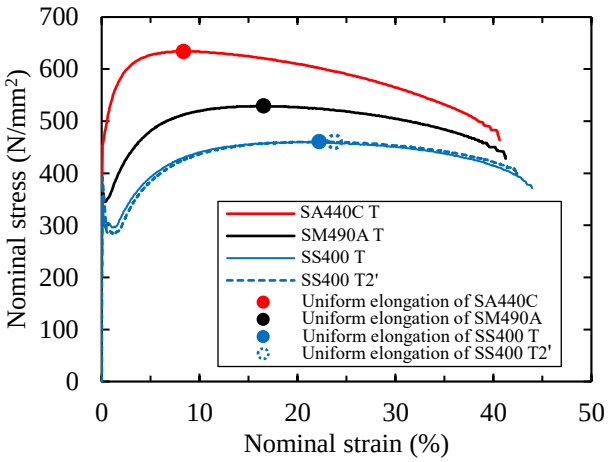

Fig. 3.1 Monotonic nominal stress vs. nominal strain curve of various structural steels with Type G

Table 3.2 Mechanical properties and chemical compositions of Type A and B

Specimens	Mechanical properties		Chemical compositions (%)				
	Yield strength (N/mm^2)	Tensile strength (N/mm^2)	C	Si	Mn	P	S
Type A	313	462	0.13	0.19	0.50	0.018	0.020
Type B	312	467					
Specification JIS G3101 [3.21] (16 mm – 40 mm)	≥235	400 - 510	-	-	-	<0.050	<0.050

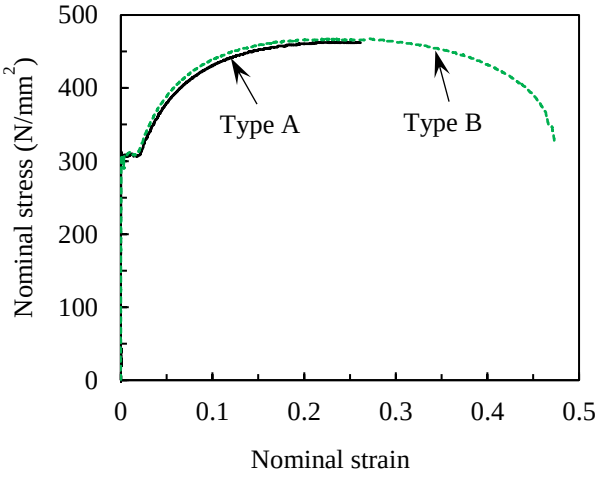

Fig. 3.2 Monotonic nominal stress vs. nominal strain curve of SS400 steel with Type A and B

Table 3.3 List of steels and loading conditions

Loading conditions		SS400 (400 N/mm^2 grade)					SM490A (490 N/mm^2 grade)			SA440C (590 N/mm^2 grade)		
		Type		Type G			Type G			Type G		
		A	B	T	T2'※	C※	T	T2	C	T	T2	C
Constant amplitude cyclic loading tests	2%	1	1	1	1	1	1	1	1	1	1	1
	3%	1	1	1	1	1	1	1	1	1	1	1
	4.5%	-	1	1	1	1	1	1	1	1	1	1
	6%	-	1	1	1	1	1	1	1	1	1	1
	7.5%	-	1	1	1	1	1	1	1	1	1	1
	9%	-	1	1	1	1	1	1	1	1	1	1
	10.5%	-	-	1	1	1	1	1	1	1	1	1
	11.25%	-	-	1	1	1	1	1	1	1	1	1
	12%	-	-	1	1	1	1	1	1	1	1	1
Monotonic tensile tests		1	1	1	1	-	1	-	-	1	-	-

Note: ※T and C indicate the cyclic tests starting with tension and compression, respectively. T2 refers to the second tension–compression cyclic test, and T2' indicates the second steel lot.

3.3. Hysteretic curves

Nominal and true stress-strain curves of tension-compression cyclic tests

Fig. 3.3 shows the stress–strain hysteretic curve of Lot I and II specimens tested with strain amplitudes of ±2%, ±3%, ±4.5%, and ±12%. (×) in the figures indicates the fracture point of the corresponding specimens. In the case of the hysteretic curve, the nominal stress and strain values vary as shown in Figs. 3.3a–3.3d. As indicated, both tensile and compressive stresses are almost symmetrical at 3% or smaller strain amplitudes. This has been also reported in previous researches such as Ono et al. [3.6] who conducted tests with strain amplitudes of 3% or smaller and stated that tensile and compressive stresses of all specimens are almost symmetry in the plot of nominal stress and nominal strain relationship. However, cyclic stress appears to lose its symmetry at larger strains ($\varepsilon \geq$ 4.5%) as it can be observed from Figs. 3.3c and 3.3d. In this regard, stress–strain hysteretic curves were replotted in true stress vs. true strain relationship, as shown in Figs. 3.3e–3.3h.

From these figures, stresses in both tension and compression sides are close to symmetry in a broader range of both small and large-strain amplitudes. Thus, it can be inferred that the relationship of the true stress and true strain is more appropriate in expressing the stress–strain hysteretic curve.

Comparison of true stress-strain curves of compression-tension cyclic tests of various structural steels

Hysteretic curves of SS400, SM490A, and SA440C derived from the compression–tension cyclic tests at strain amplitudes of ∓3%, ∓4.5%, ∓7.5%, and ∓12% were plotted

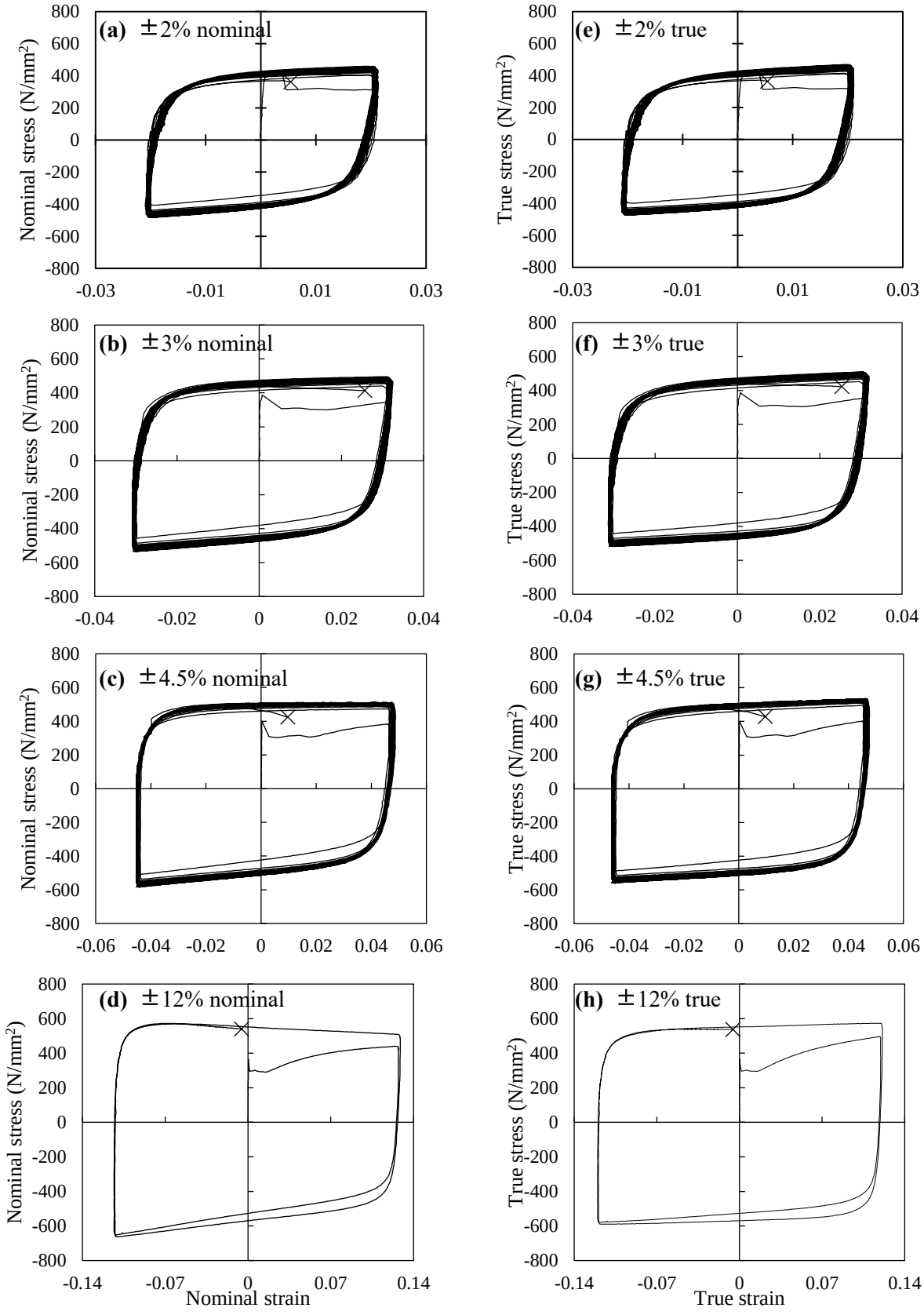

Fig. 3.3 Comparison of nominal and true stress-strain curves of SS400 steel

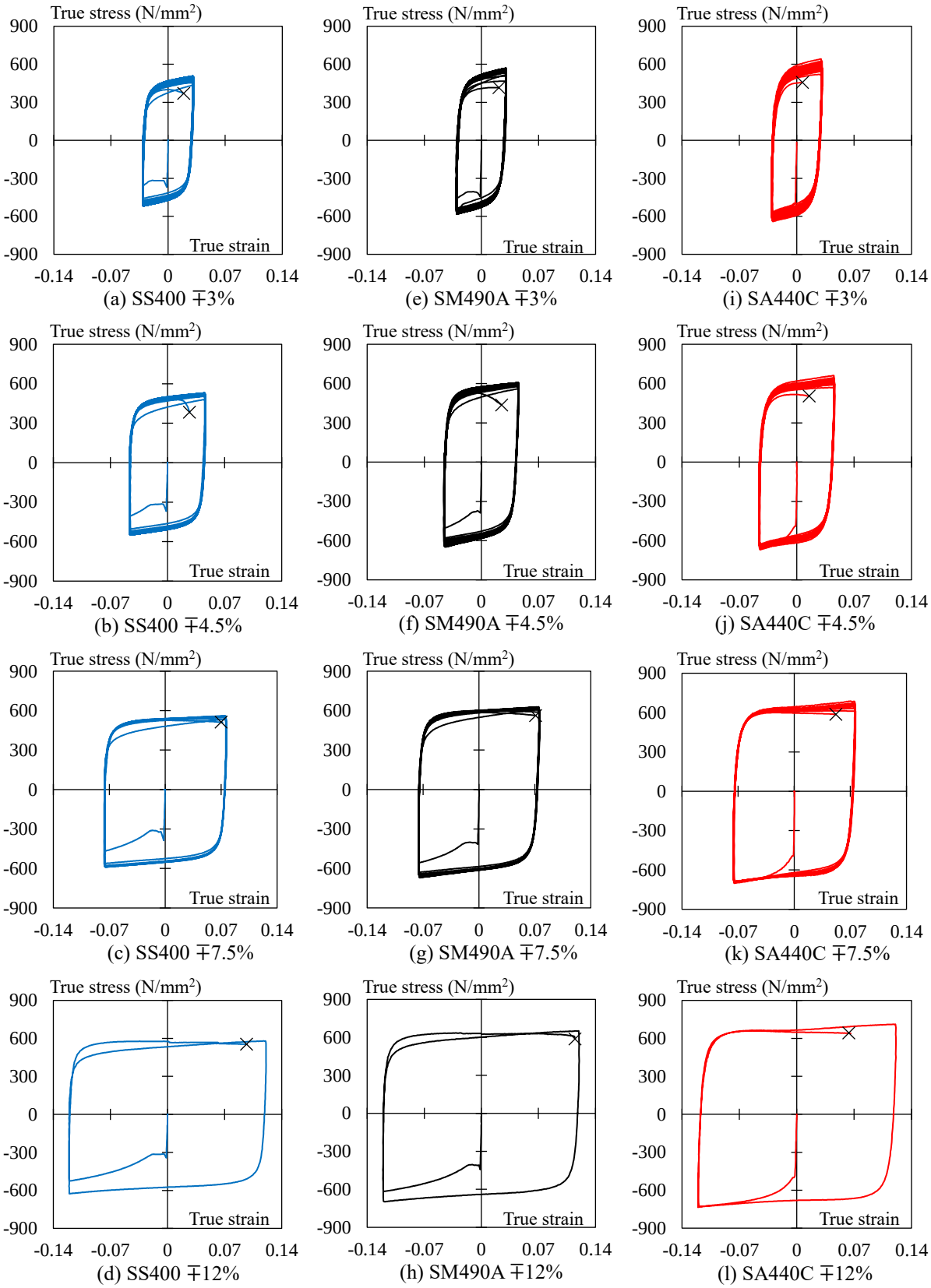

Fig. 3.4 True stress-true strain curves of various structural steels

in the true stress and true strain relationship (Fig. 3.4).

Fig. 3.4 indicates that the true stress–true strain hysteretic curves of the considered steels exhibit excellent symmetric behaviors between the tensile and compressive stresses, irrespective of the increase in the strain amplitudes.

3.4. LCF and ELCF performances of 400 N/mm^2 grade structural steel

Table 3.4 shows the number of cycles to fracture together with their corresponding strain amplitudes considered in this study.

Table 3.4 List of loading conditions and their corresponding number of cycles to fracture

Loading conditions		Number of cycles to fracture, N_f				
		Type		Type G		
		A※[1]	B※[1]	T※[2]	C※[2]	T2'※[2]
Constant amplitude cyclic	2%	168	153	215	176	186
	3%	55	47	82	81	80
	4.5%	-	18	24	23	26
	6%	-	10	12	11	12
	7.5%	-	6	7	6	7
	9%	-	4	4	3	4
	10.5%	-	-	3	2	3
	11.25%	-	-	2	2	2
	12%	-	-	1	1	1

※[1] Type A and B specimens are both tested only under tension as initial loading direction.
※[2] T and C refer to cyclic tests starting with tensile and compressive excursions, respectively. T2 refers to the second tension-compression cyclic test, and T2 indicates the second steel lot.

3.4.1 Comparison with previous study in LCF regime

In this section, the effects of specimen configurations and different lots on the strain-life curve will be investigated. Moreover, the comparison between the Type A specimen and the findings from a previous study [3.6] related to 400 N/mm^2 grade structural steel in which the specimen shape was similar to the Type A specimen, will be also taken into consideration. The marks (□) and (▲) in Fig. 3.5a illustrate test data of tension as the initial loading direction obtained from previous test results and the Type A specimen, respectively. From this figure, it is evident that the test results of the Type A specimen in conjunction with data from a previous study exhibit a linear relationship together for strain amplitudes up to 3.5%. This means that the reliability of test data of this study can be verified.

3.4.2 Strain–life curve in LCF and ELCF regimes

The marks (△), (●), and (○) in Fig. 3.5b indicate the strain-life curve of Type B for the specimens Lot I and II subject to tension as initial loading excursion. Even for larger strains, it can be observed from the test data of Type B in conjunction with data from specimen Type A as well as data from a previous study, that Type G specimens exhibit continuous linear relationships for strain amplitudes up to approximately 10%. Additionally, it is worth noting that there are almost no significant effects related with specimen configurations as well as different lot productions on the strain-life curve based upon the range of specimens and strain amplitudes considered in this study. It is inferred that the deformation capacity of steel materials can be evaluated in a unified manner regardless of the differences in lot productions.

Furthermore, during the test, it is observed that the scatter of the test results is likely to

become slightly prominent in the case of specimens tested for small-strain amplitudes ($\varepsilon \leq 4.5\%$) despite the fact that the overall test result appears to be somewhat stable. Specimen fractures are due to the development of cracks and their propagation in this range ($\varepsilon \leq 4.5\%$). For this reason, test results may vary owing to these different crack developing locations. By contrast, the scatter became smaller at larger strain amplitudes where necking in the center of the effective length section became more dominant.

3.4.3 Strain–life curve of compression–tension cyclic tests

The (●) mark in Fig. 3.5c indicates the strain life curve of Lot I specimens tested with compression as initial loading excursion. Likewise, a good linear relationship can be obtained for strain amplitudes up to approximately 10%. Additionally, it is noteworthy that the life of specimens tested with compressive loading as the initial loading tend to be slightly shorter than those tested with tensile loading. Similar loading direction influences were also observed in [3.24] who investigated the effects of tensile and compressive loading sequences as a part of their study.

This cycle life difference is attributed to the difference of the cumulative strain up to fracture. The cumulative strain of the specimens tested with compression-tension cyclic test might be half-cycle larger than that tested with tension-compression test. Since specimen fractures under tensile load, there is a possibility that the cumulative strain with the half-cycle larger may cause this 1 cycle difference. In this study, only small difference appears at large strain amplitudes. However, the difference caused by the initial loading direction can be considered negligible.

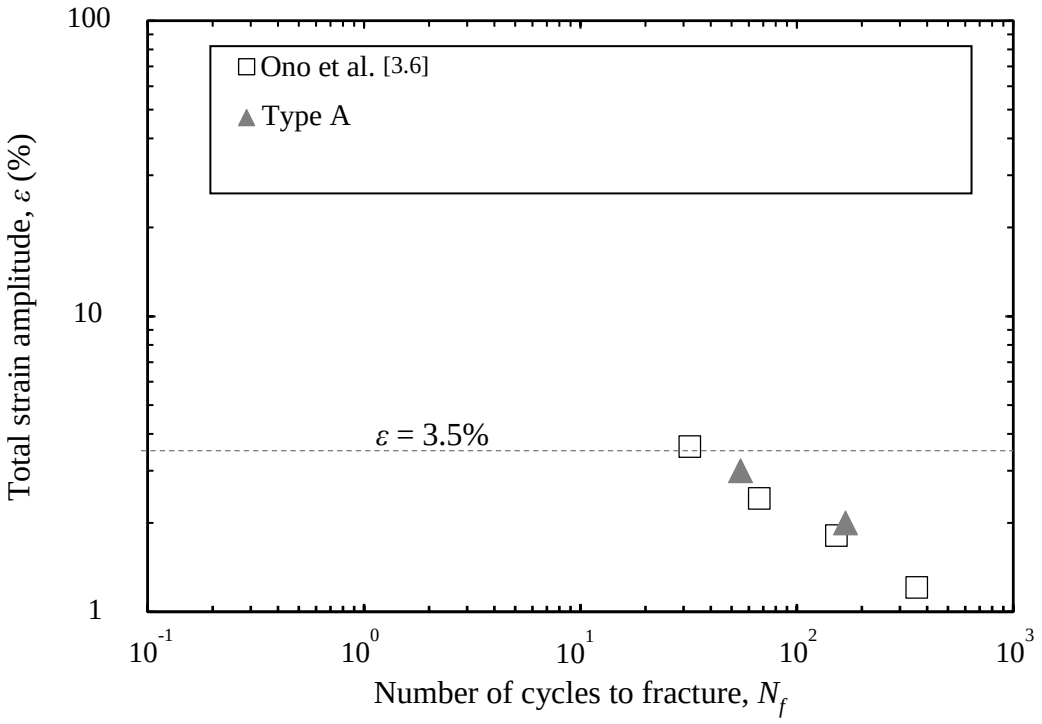

(a) Comparison between Type A specimen and previous study [6] specimen shapes are similar) in low-cycle fatigue (LCF) regime

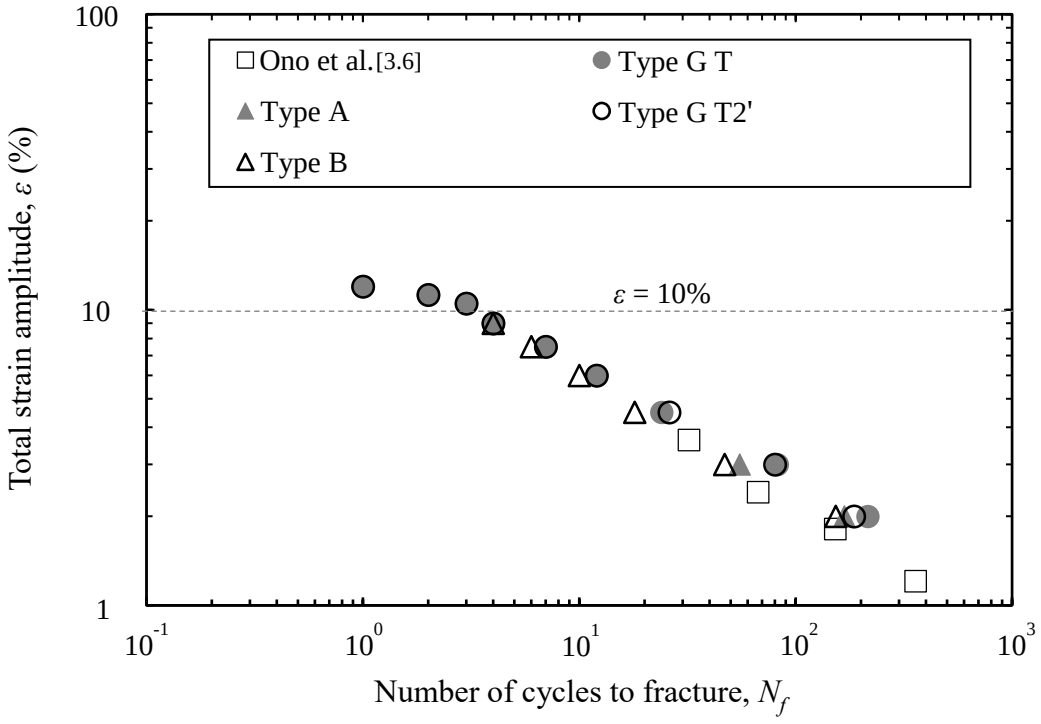

(b) Strain-life curve in LCF and extremely LCF (ELCF) regimes

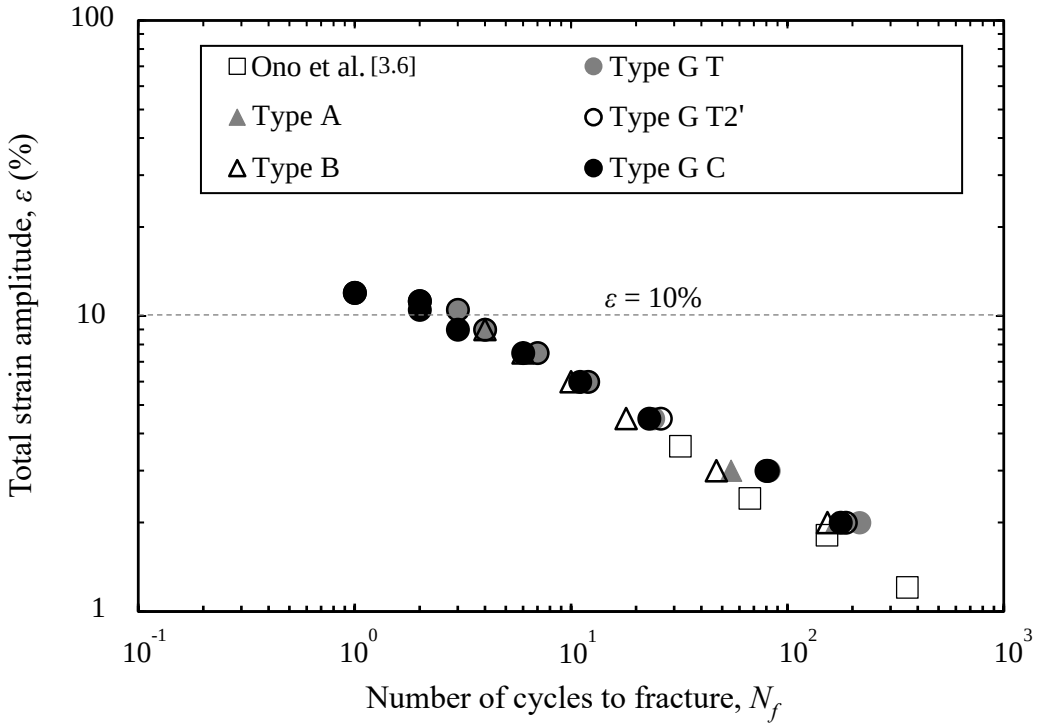

(c) Strain-life curve of cyclic tests that started with compression as the initial loading

Fig. 3.5 Relationships between strain amplitudes and number of cycles to fracture

3.5. Effects of different steel grades on the LCF and ELCF performances

To examine the low and extremely low cycle fatigue performances of various steel grades, the relationship between strain amplitude, ε, and the number of cycles to fracture, N_f, (strain–life curve up to fracture) of SS400, SM490A and SA440C were plotted (Fig. 3.6). Strain amplitudes and their corresponding number of cycles to fracture of each steel are listed in Table 3.5.

Fig. 3.6 shows that the overall strain–life curves of the considered steels exhibit a linear relationship up to approximately 10%. Furthermore, despite the minor individual differences, the cyclic deformation capacities up to the fracture point under small to large strain regions can be evaluated in a unified manner for the loading conditions and steel grades presented in this study.

Data regression using a power function was conducted to obtain the overall life-prediction curve according to the Manson[3.1] – Coffin[3.2] relation (superimposed as a dashed line as shown in Fig. 3.6), as described by Eq. 3.1.

$$\varepsilon = 0.168\left(N_f\right)^{-0.4}, (2\% \le \varepsilon \le 10\%) \tag{3.1}$$

Fig. 3.6 shows that the Manson–Coffin relation fits well with the test data under strains of approximately 2–10%. However, the value of N_f at strains greater than 10% would be overestimated if the scope of application of Eq. 3.1 was enlarged to 12%. This discrepancy in the Manson–Coffin prediction of other steel materials has been reported in previous studies [3.25–3.28].

Table 3.5 Strain amplitudes and their corresponding number of cycles to fracture

Strain amplitude, ε	Number of cycles to fracture, N_f								
	SS400 (400 N/mm^2 grade) Type G			SM490A (490 N/mm^2 grade) Type G			SA440C (590 N/mm^2 grade) Type G		
	T	T2'※	C※	T	T2	C	T	T2	C
2%	186	215	176	223	204	169	179	176	200
3%	81	82	82	90	98	92	86	82	81
4.5%	23	24	23	30	32	27	30	30	29
6%	11	12	11	14	14	15	15	15	14
7.5%	7	7	6	8	8	8	10	10	9
9%	4	4	3	6	5	5	6	6	5
10.5%	3	3	2	4	4	3	4	4	3
11.25%	2	2	2	3	3	2	3	3	2
12%	1	1	1	2	2	1	1	1	1

Note: ※T and C indicate the cyclic tests starting with tension and compression, respectively. Here, T2 refers to the second tension–compression cyclic test, and T2' indicates the second steel lot.

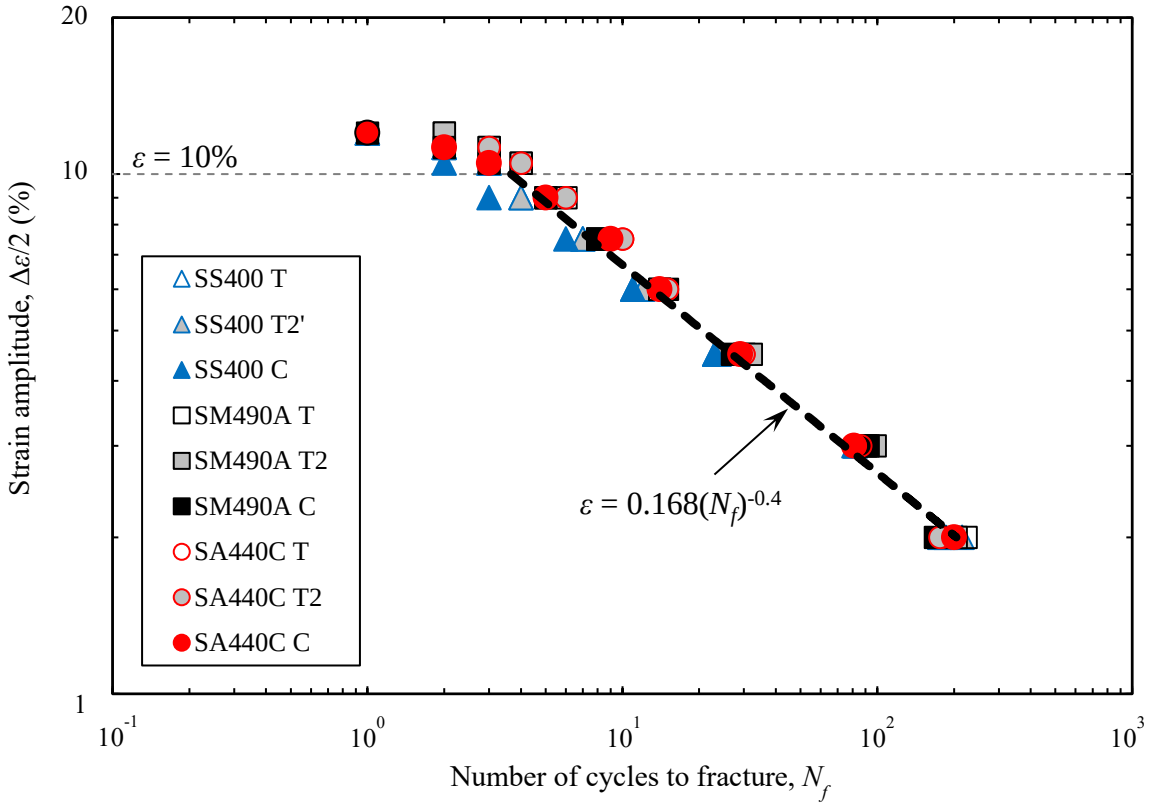

Fig. 3.6 Strain–life curve up to fracture of SS400, SM490A, and SA440C steels

3.6. Deformation capacity to ultimate point of different structural steels

3.6.1 Correlation between steel member and material

In contrast to the material test subjected to uniaxial loading, the structural member of the steel frame, such as the steel beam, is generally subjected to moment gradient (Fig. 3.7a). In this case, the strain distributes nonuniformly and inelastically inside the yielding region, which easily leads to the concentration of damage at the beam end flange, i.e., portion *A* of the critical section (Fig. 3.7b). Once portion *A* reaches the maximum stress (point T_1), necking forms, large plastic strain concentrates at this portion, and stress decreases (Figs. 3.7c, 3.7d and 3.7e). Whereas other parts outside portion *A*, such as portion *B*, start to unload (Fig. 3.7f) at point T_1. As a result, the overall strength of the steel member deteriorates rapidly after reaching the maximum value (Fig. 3.7g), and finally the member fractures within small deformation.

In case of the cyclic loadings, the behavior of the flange at the critical section (portion A), which determines the deformation capacity of the beam, can be thought to be in association with the material test results up to the maximum strength. However, after the maximum strength, the loading cycle until fracture of the beam decreases dramatically compared with that of the material test. Therefore, the point up to the maximum strength should be also considered as an additional index related to the evaluation of the plastic deformation capacity of steel members.

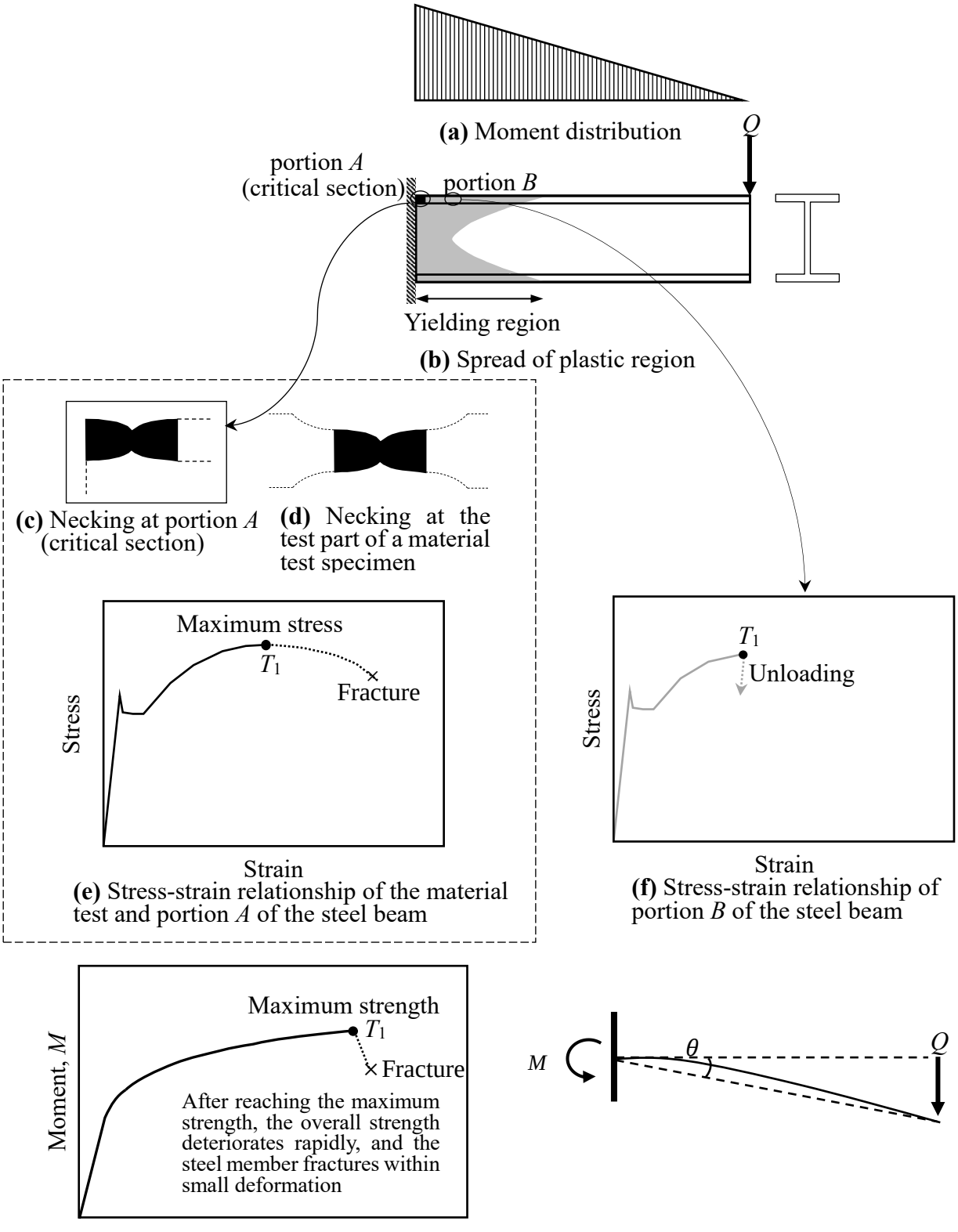

Fig. 3.7. Schematic drawing of a cantilever beam subjected to monotonic load

3.6.2 Definition of ultimate point

As discussed in section 3.6.1, the local behavior of steel members, such as the critical part of the steel beam flange end, can be associated with the behavior of the steel material up to the ultimate point or maximum strength. After this ultimate point, due to damage concentration caused by moment gradient, the strengths of the members drop rapidly, and the members fracture within a small number of loading cycles. Therefore, the evaluation of the deformation capacity up to the ultimate point should be considered in addition to deformity up to the fracture.

To obtain the unified evaluation of ultimate point for the considered steels, three definitions of ultimate points (based on negative secondary stiffness (or tangent modulus), peak stress N_p, and damage initiation (onset of crack or necking) N_{di}) are discussed. Fig. 3.8 exhibits the nominal stress and cumulative strain relationships obtained from the tension side of the nominal stress-nominal strain hysteretic curves at strains of 4.5% and 6%. The symbols (O), (◆) and (▽) in the figure represent the onset of negative secondary stiffness, peak stress N_p, and damage initiation N_{di}. Fig. 3.8 demonstrates that negative secondary stiffness occurs mostly a few cycles before fracture for all the studied steels when strain is 4.5% or less. While it develops near the peak stress N_p at strain of 6% or greater. This indicates that the negative secondary stiffness is strain amplitude dependent, which is not suitable for unified evaluation of the ultimate point for both small and large strain amplitudes. Besides, for SA440C, the ultimate point is predicted in the first cycle based on N_p. Nevertheless, due to the material feature of SA440C (Figs. 3.8, 3.9c and 3.9f), the stress reaches its peak in the first cycle, but after that the stress is almost stable, and cyclic deformation capacity can still be demonstrated. This means that it is not

reasonable to consider N_p (=1) as the ultimate point. In other words, peak stress N_p is dependent on material feature and not appropriate for the unified evaluation of ultimate point for the considered steels. In contrast to negative secondary stiffness and peak stress, damage initiation N_{di} is thought to be independent of strain amplitudes and material features. Therefore, in this study, damage initiation (onset of crack or necking) point N_{di} is considered as the ultimate point of the steel materials.

In this study, the number of cycles to damage initiation, N_{di}, was obtained from the test observations on the surface of the specimens within the limits of the studied specimen shapes, loading conditions, and structural steels. Here, N_{di} is defined as the crack initiation for specimens tested at smaller amplitudes ($\varepsilon \leq 3\%$) and as the onset of necking for those tested at larger amplitudes ($\varepsilon \geq 4.5\%$), provided that fractures due to crack and neck were more dominant in relatively small and large strain amplitudes, respectively. To identify the necking initiation, the loading tests were paused at each peak tensile strain to check the condition of the specimens. Although observing necking and cracking during the tests is difficult and may result in some discrepancies when compared to N_p, these damage initiations have also been considered the ultimate point in previous studies [3.29–3.32] to examine the ductile fracture models. Besides, the previous studies by [3.13, 3.33] have indicated that, in many cases, crack initiation is considered as a reasonable limit state to evaluate structural performance. The number of cycles to damage initiation, N_{di}, and the corresponding strain amplitudes of each steel are presented in Table 3.6. This N_{di} is also marked as symbols (▼) and (▽) for cracking and necking points in Fig. 3.9, respectively.

Table 3.6 Number of cycles to damage initiation at the corresponding strains

Strain amplitude, ε	Number of cycles to damage initiation, N_{di}									Number of cycles to
	SS400 (400 N/mm^2 grade)			SM490A (490 N/mm^2 grade)			SA440C (590 N/mm^2 grade)			
	T	T2'※	C※	T	T2	C	T	T2	C	
2%	94	109	95	110	100	78	87	85	98	Crack
3%	39	40	40	47	48	47	50	45	41	Crack
4.5%	10	10	9	17	15	17	9	9	9	Neck
6%	5	5	4	7	7	7	5	5	5	Neck
7.5%	3	3	3	4	4	4	3	3	3	Neck
9%	2	2	2	3	3	3	2	2	2	Neck
10.5%	2	2	1	2	2	2	2	2	2	Neck
11.25%	1	1	1	2	2	1	1	1	1	Neck
12%	1	1	1	1	1	1	1	1	1	Neck

Note: ※T and C indicate the cyclic tests starting with tension and compression, respectively. T2 refers to the second tension–compression cyclic test, and T2' indicates the second steel lot.

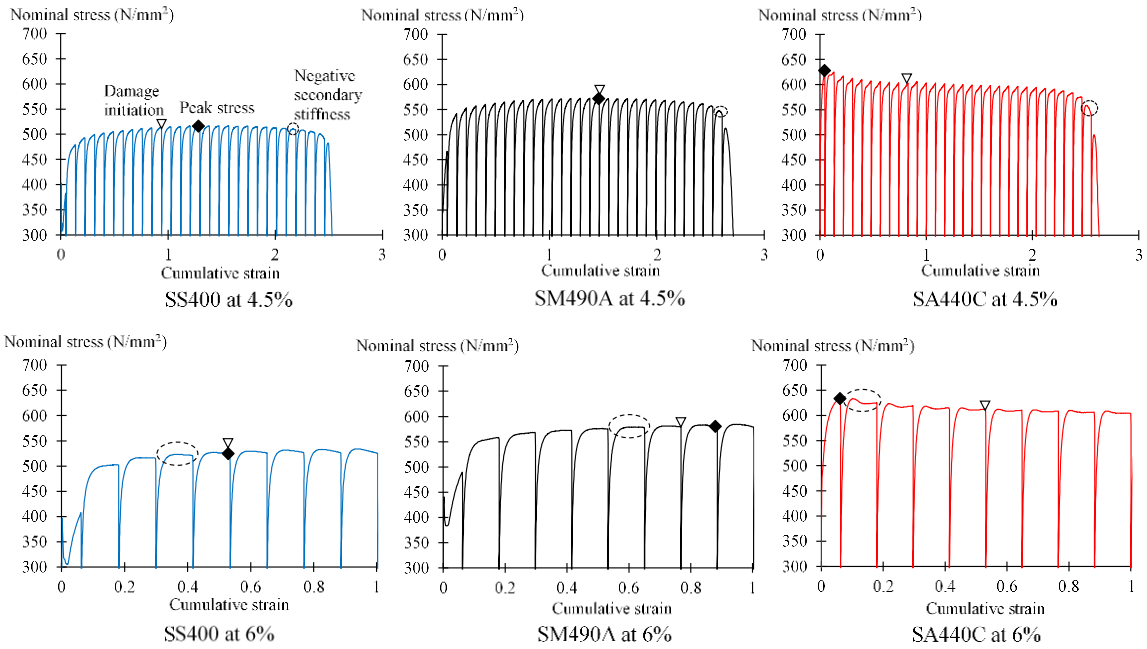

Fig. 3.8 Relationship between nominal stress and cumulative strains at ±4.5% and ±6%

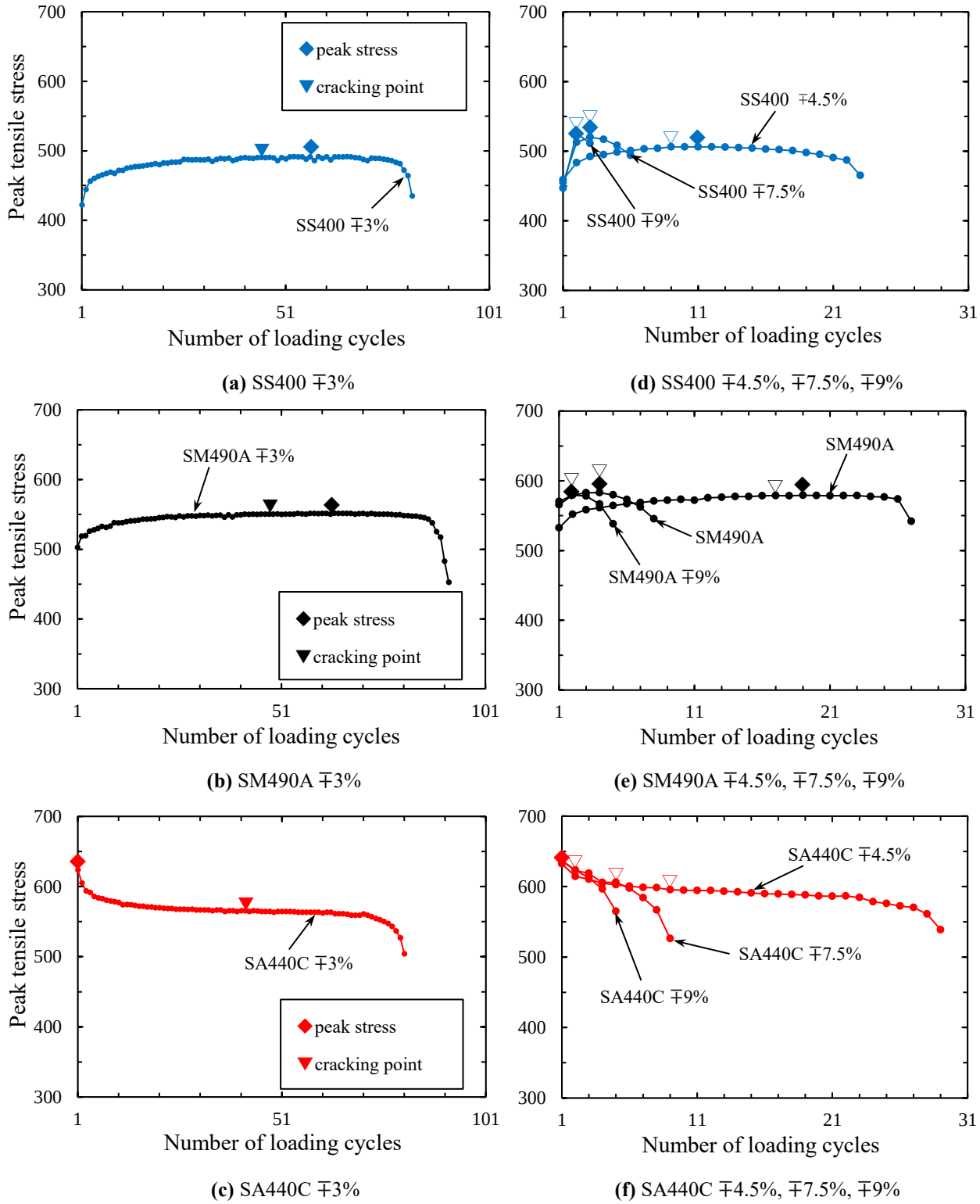

(a) SS400 ∓3%

(d) SS400 ∓4.5%, ∓7.5%, ∓9%

(b) SM490A ∓3%

(e) SM490A ∓4.5%, ∓7.5%, ∓9%

(c) SA440C ∓3%

(f) SA440C ∓4.5%, ∓7.5%, ∓9%

Fig. 3.9 Relationship between peak tensile stress and loading cycles at ∓3%, ∓4.5%, ∓7.5%, ∓9%

3.6.3 Validation of the definition

From Fig. 3.9, it is observed that the N_{di} happened at almost the same points in time for the considered steels. While this trend is observed only for N_p of SS400 and SM490A. Also, this figure shows that N_p and N_{di} occurred at quite similar points in time for SS400 and SM490A. For comparison and examining their correlations, the N_{di} and N_p of SS400 and SM490A are plotted as shown in Fig. 3.9. N_p is used to compare with N_{di} because it is directly derived from the test data and thus accurate when applicable. In Fig. 3.10, the blue triangles and black squares indicate the N_{di} versus N_p relationship of SS400 and SM490A, respectively. This figure reveals that N_{di} exhibits an excellent correspondence with N_p. Thus, the number of cycles to damage initiation, N_{di}, can be used as the ultimate point for SS400 and SM490A. For further discussion, the number of cycles up to damage initiation, N_{di} is also used for SA440C as N_p is not applicable for this steel.

3.6.4 Deformation capacity to ultimate point

According to previous studies e.g., [3.34–3.40], there are two fracture modes - that is, fracture due to surface cracks (known as fatigue fracture) and internal cracks (void growth lead to neck which is categorized into ductile fracture), that cause fatigue damages. The surface cracks are more dominant at small amplitudes (±3% or less, considered as crack-dominated region in this study). The internal cracks are more predominant at the large strain region (±4.5% or greater, considered as neck-dominated region in this study). This observation is also consistent with [3.34, 3.35, 3.39]. In accordance with the transition of dominant fracture modes, the strain-life curves show either bilinear or linear relationship in some steel materials [3.26, 3.38, 3.40]. Nevertheless, for the structural steels considered in this study, Fig. 3.11 shows that despite the minor individual differences, the

ε–N_{di} and ε–N_f relationships show linear relationships (at strain amplitudes of ±2–±12% for N_{di} and 2–10% for N_f), irrespective of the differences in the presented steel lots, and initial loading directions. In the figure, the uniform elongation of SA440C high-performance steel is lower when compared to others. This may be contributed by the effect of heat treatment to achieve high strength. The regression equation of deformation capacity up to the ultimate point can be expressed as follows:

$$\varepsilon = 0.117(N_{di})^{-0.39}, (2\% \leq \varepsilon \leq 12\%) \quad (3.2)$$

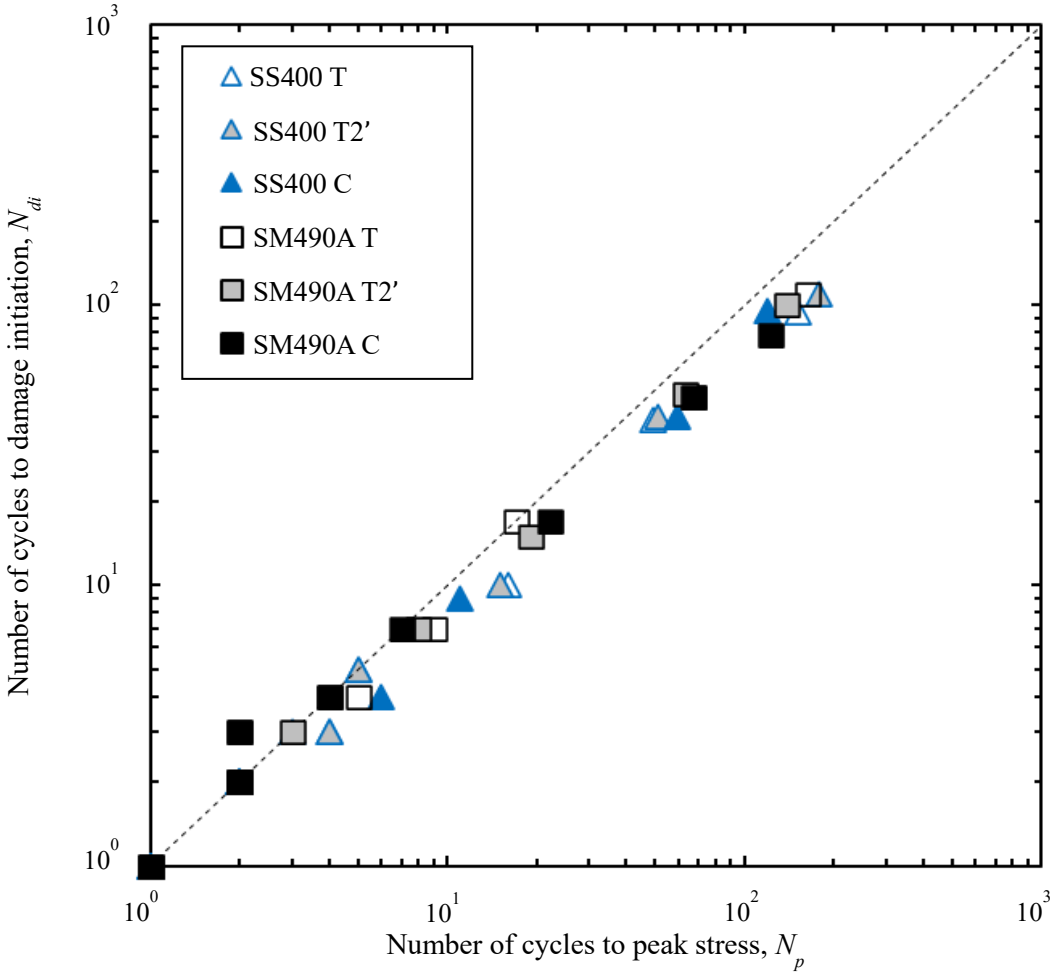

Fig. 3.10 Relationship between N_{di} and N_p.

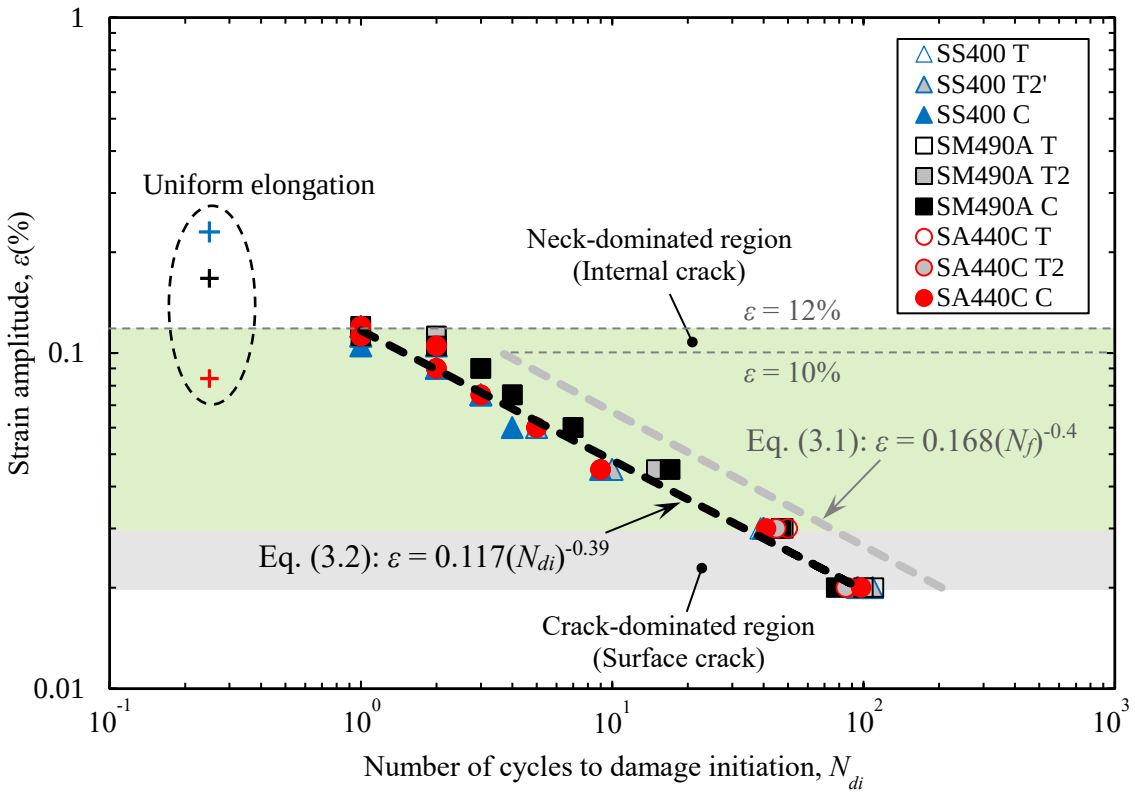

Fig. 3.11 Strain-life curve up to ultimate point

3.6.5 Variable amplitude cyclic loading tests

Objective

The seismic loads are typically the loading patterns consisting of more than one amplitude. Given the combination of amplitudes imposed by such lateral loads, the variable amplitude cyclic loading tests were conducted. The obtained test results are discussed using the evaluation method (Eq. 3.1) and (Eq. 3.2) together with Miner [41]'s rule to further investigate its applicability under seismic actions.

Variable amplitude loading histories

Three patterns of loading histories are used to conduct the variable amplitude cyclic tests on SS400, SM490A and SA440C steels. These three patterns are shown in Fig. 3.12.

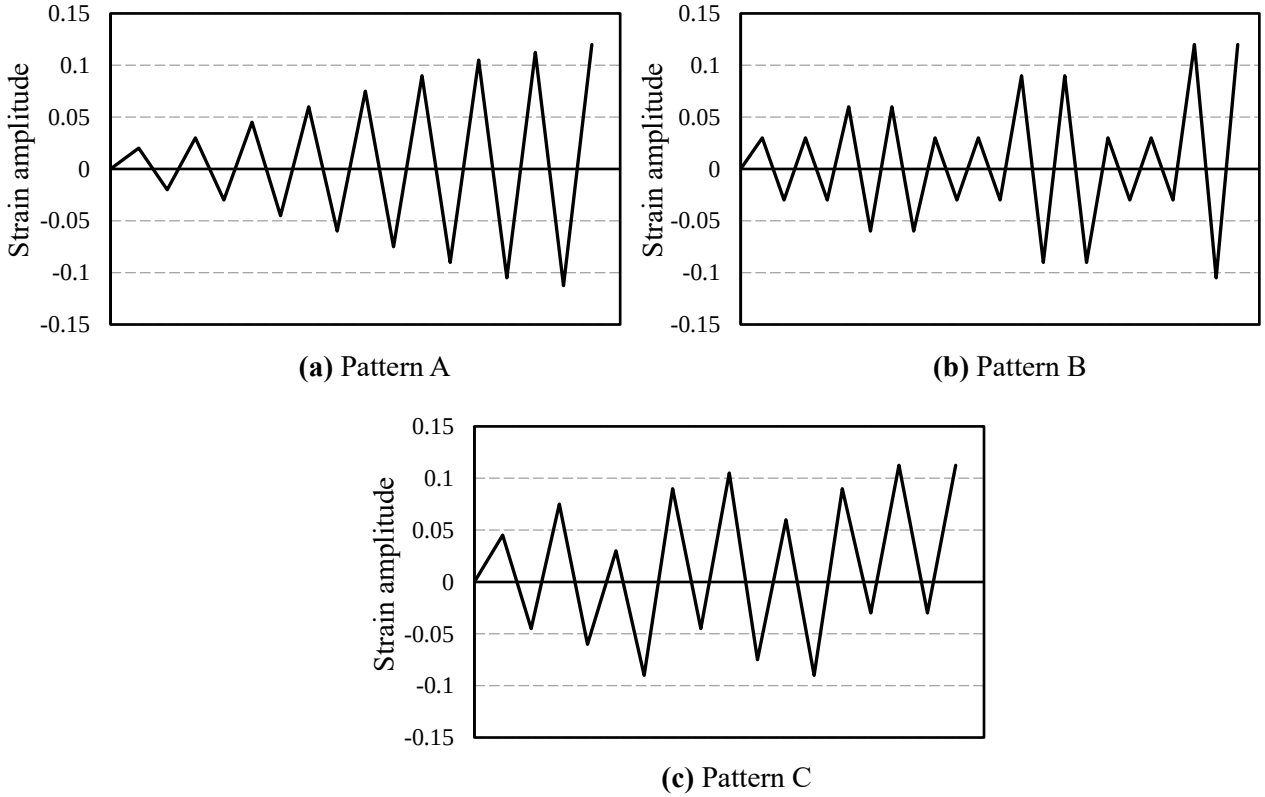

(a) Pattern A

(b) Pattern B

(c) Pattern C

Fig. 3.12 Variable amplitude cyclic loading histories

Cumulative damage evaluation based on Miner's rule

In addition to fracture, the cumulative damage to ultimate point is also discussed. During the tests, the ultimate points (points of crack or necking initiation) were observed. However, only necks appeared in these loading patterns owing to the dominance of large strain amplitudes. The cumulative damage values up to fracture and ultimate points were calculated using Miner's rule (Eqs. 3.3 and 3.4).

$$D_{Nf} = \sum_i \frac{n_i}{N_f} \tag{3.3}$$

$$D_{Ndi} = \sum_i \frac{n_i}{N_{di}} \tag{3.4}$$

where n_i is the number of cycles of the corresponding strain amplitudes, N_f and N_{di} are calculated using Eqs. 3.1 and 3.2. D_{Nf} and D_{Ndi} indicates the cumulative damage, which is evaluated as fracture and ultimate point when they reach 1. The test results (Fig. 3.13) reveal that the ultimate point could be evaluated within an error range of approximately 20% by applying Miner's rule even under the condition of variable amplitudes. Besides the cumulative damage up to fracture can be also evaluated with a similar range of error (Fig. 3.14).

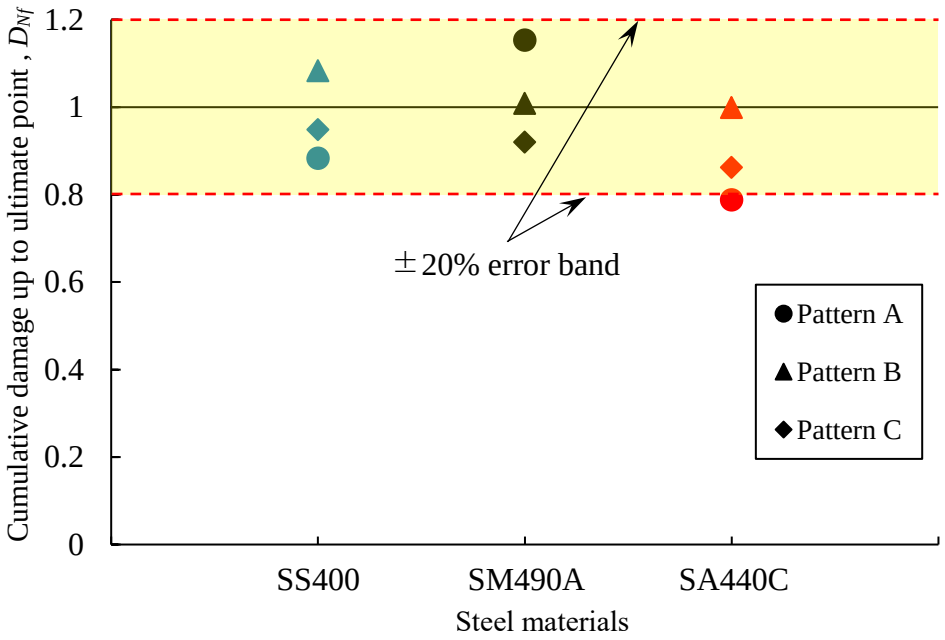

Fig. 3.13 Cumulative damage up to ultimate points of the corresponding structural steels

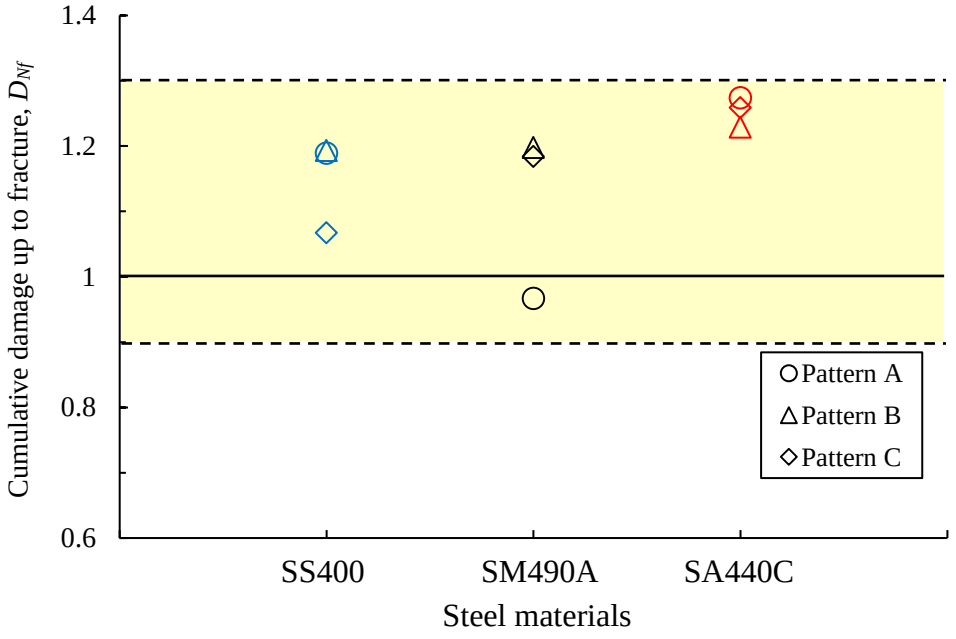

Fig. 3.14 Cumulative damage up to fracture of the corresponding structural steels

3.7. Summary

In this chapter, experimental investigations were performed on the low-cycle fatigue (LCF) and extremely low-cycle fatigue (ELCF) performances of structural steels of different strength levels with nominal tensile strengths of 400 N/mm^2 (SS400), 490 N/mm^2 (SM490A) and 590 N/mm^2 (SA440C). To obtain test data of the studied steels in both small (±2%) and large (±12%) strain regions, constant amplitude strain-controlled cyclic loadings with tensile and compressive excursions were carried out. Although these structural steels have different strength levels, their chemical compositions are not much different. For the steels and loading conditions considered in this study, the key conclusions can be drawn as follows:

- In case of plotting the hysteretic curve in the nominal stress-strain relationship, the tensile and compressive stresses appear to lose their symmetry at strain of 4.5% or greater. By plotting in the true stress-strain relationship, stresses in both tension and compression sides are close to symmetry in a broader range of both small and large strain amplitudes. It can be said that the relationship of true stress and true strain is more appropriate in expressing the stress-strain hysteretic curves.
- A linear relationship was obtained for strains with amplitudes up to 3.5%. Additionally, the strain-life curve of two different lots of specimens tested with tension as the initial loading yielded a linear relationship in comparison with the specimen tested with compressive loading with small and large strain amplitudes, despite the minimal dispersion at moderate strains. In other words, one can consider that there are almost no significant effects of initial loading direction, specimen configuration, as well as different lots on the strain-life curve in the case of specimens and strain amplitudes considered in this study

- The low-cycle fatigue (LCF) and extremely LCF (ELCF) performances of the considered (SS400, SM490A and SA440C) structural steels can be evaluated in a unified manner up to a strain amplitude of approximately 10%. Based on this result, data regression using a power function was conducted to obtain the LCF equation for the considered structural steels.
- By defining the damage initiation (onset of crack or neck) as the ultimate point, the deformation capacity up to ultimate point of the considered structural steels (SS400, SM490A, SA440C) can be evaluated using one N_{di} equation from 2% to 12% strains.
- From the variable amplitude cyclic tests, the N_{di} equation was also confirmed to be validated under the seismic loads which are typically the loading patterns consisting of more than one amplitude.
- As an application of the materials' evaluation equations, the LCF performance of steel members (steel beam and Buckling-Restrained Brace) is also discussed in Appendix 1. However, the purpose is not to accurately evaluate a member based on the material's equation; rather, to domonstrate the performance calculated by the material's equation can be used as an indicator of the desired performance of the member. The result in Appendix 1 shows that material's N_{di} can be used as a benchmark for the performance that Buckling-Restrained Brace should aim for.

References for chapter 3

[3.1] Manson SS. Behavior of materials under conditions of thermal stress. J Appl Phys 1943;14:399–405.

[3.2] Coffin LF. A study of the effects of cyclic thermal stresses in ductile metals. Transaction of the ASME 1954;76:931–50.

[3.3] Radhakrishnan VM. On the bilinearity of the Coffin-Manson low-cycle fatigue relationship. Int J Fatigue 1992;14:305–11. https://doi.org/10.1016/0142-1123(92)90481-Q.

[3.4] Mediratta SR, Ramaswamy V, Rama Rao P. Two stage cyclic work hardening and two slope coffin-manson relationship in dual phase steels. Scripta Metallurgica 1986. https://doi.org/10.1016/0036-9748(86)90253-X.

[3.5] Pereira JCR, de Jesus AMP, Xavier J, Fernandes AA. Ultra low-cycle fatigue behaviour of a structural steel. Eng Struct 2014;60:214–22. https://doi.org/10.1016/j.engstruct.2013.12.039.

[3.6] Ono T, Kako Y, Sato A, Iwata M. A study on low cycle fatigue characteristics of metallic material. Journal of Structural and Construction Engineering (Transactions of AIJ) 2000;65:193–9. https://doi.org/10.3130/aijs.65.193_1.

[3.7] Amiri HR, Aghakouchak AA, Shahbeyk S, Engelhardt MD. Finite element simulation of ultra low cycle fatigue cracking in steel structures. J Constr Steel Res 2013;89:175–84. https://doi.org/10.1016/j.jcsr.2013.07.007.

[3.8] Bleck W, Dahl W, Nonn A, Amlung L, Feldmann M, Schäfer D, et al. Numerical and experimental analyses of damage behaviour of steel moment connection. Eng Fract Mech 2009;76:1531–47. https://doi.org/10.1016/j.engfracmech.2009.03.004.

[3.9] Tong L, Huang X, Zhou F, Chen Y. Experimental and numerical investigations on extremely-low-cycle fatigue fracture behavior of steel welded joints. J Constr Steel Res 2016;119:98–112. https://doi.org/10.1016/j.jcsr.2015.12.015.

[3.10] Huang X, Zhao J. A cumulative damage model for extremely low cycle fatigue cracking in steel structure. Structural Engineering and Mechanics 2017;62:225–36. https://doi.org/10.12989/sem.2017.62.2.225.

[3.11] Algarni M, Choi Y, Bai Y. A unified material model for multiaxial ductile fracture and extremely low cycle fatigue of Inconel 718. Int J Fatigue 2017;96:162–77. https://doi.org/10.1016/j.ijfatigue.2016.11.033.

[3.12] Kanvinde AM, Deierlein GG. Micromechanical Simulation of Earthquake-Induced Fracture in Steel Structures. John A Blume Earthquake Engineering Center Technical Report 2004;145.

[3.13] Kanvinde AM, Deierlein GG. Cyclic void growth model to assess ductile fracture initiation in structural steels due to ultra low cycle fatigue. J Eng Mech 2007;133:701–12. https://doi.org/10.1061/(ASCE)0733-9399(2007)133:6(701).

[3.14] Huang X, Tong L, Zhou F, Chen Y. Prediction of fracture behavior of beam-to-column welded joints using micromechanics damage model. J Constr Steel Res 2013;85:60–72. https://doi.org/10.1016/j.jcsr.2013.02.014.

[3.15] Mendes LAM, Castro LMSS. A simplified reinforcing steel model suitable for cyclic loading including ultra-low-cycle fatigue effects. Eng Struct 2014;68:155–64. https://doi.org/10.1016/j.engstruct.2014.02.031.

[3.16] Sakano M, Mikami I, Takaba S. Low cycle fatigue behavior of steel pier beam-column joint. Doboku Gakkai Ronbunshu 1997:49–60. https://doi.org/10.2208/jscej.1997.563_49.

[3.17] Sakano M, Wahab MA. Extremely low cycle (ELC) fatigue cracking behaviour in steel bridge rigid frame piers. J Mater Process Technol 2001;118:36–9. https://doi.org/10.1016/S0924-0136(01)00857-3.

[3.18] Tateishi K, Hanji T. Low cycle fatigue strength of butt-welded steel joint by means of new testing system with image technique. Int J Fatigue 2004;26:1349–56. https://doi.org/10.1016/j.ijfatigue.2004.03.016.

[3.19] Dodd LL, Restrepo-Posada JI. Model for predicting cyclic behavior of reinforcing steel. Journal of Structural Engineering (United States) 1995;121:433–45. https://doi.org/10.1061/(ASCE)0733-9445(1995)121:3(433).

[3.20] Dusicka P, Itani AM, Buckle IG. Cyclic response of plate steels under large inelastic strains. J Constr Steel Res 2007;63:156–64.

https://doi.org/10.1016/j.jcsr.2006.03.006.

[3.21] JIS (Japanese Industrial Standards) G 3101. Rolled steels for general structure 2010.

[3.22] JIS (Japanese Industrial Standards) G 3106. Rolled steels for welded structure 2015.

[3.23] JISF (the Japan Iron and Steel Foundation). High performance 590 N/mm^2 steel for building structures (SA440). JISF Specification No. MDCR 0013-2004 2004.

[3.24] Kondo Y. Fatigue under variable amplitude loading. In: I. M, RO. R, B. K, editors. Comprehensive Structural Integrity. 1st ed., Hoboken, NJ, USA: Elsevier; 2003, p. 253–79. https://doi.org/10.1016/B0-08-043749-4/04029-5.

[3.25] Tateishi K, Hanji T, Minami K. A prediction model for extremely low cycle fatigue strength of structural steel. Int J Fatigue 2007;29:887–96. https://doi.org/10.1016/j.ijfatigue.2006.08.001.

[3.26] Shimada K, Komotori J, Shimizu M. The applicability of the Manson-Coffin law and Miner's law to extremely low cycle fatigue. Transactions of the Japan Society of Mechanical Engineers Series A 1987;53:1178–85. https://doi.org/10.1299/kikaia.53.1178.

[3.27] Kuroda M. Extremely low cycle fatigue life prediction based on a new cumulative fatigue damage model. Int J Fatigue 2002;24:699–703. https://doi.org/10.1016/S0142-1123(01)00170-0.

[3.28] Xue L. A unified expression for low cycle fatigue and extremely low cycle fatigue and its implication for monotonic loading. Int J Fatigue 2008;30:1691–8. https://doi.org/10.1016/j.ijfatigue.2008.03.004.

[3.29] Usami T, Ge H. A performance-based seismic design methodology for steel bridge systems. Journal of Earthquake and Tsunami 2009;03:175–93. https://doi.org/10.1142/S179343110900055X.

[3.30] Jia LJ, Kuwamura H. Ductile fracture simulation of structural steels under monotonic tension. Journal of Structural Engineering 2014;140:04013115. https://doi.org/10.1061/(ASCE)ST.1943-541X.0000944.

[3.31] Kang L, Ge H. Predicting ductile crack initiation in steel bridge piers with unstiffened box section under specific cyclic loadings using detailed and simplified evaluation methods. Advances in Structural Engineering 2015;18:1427–42. https://doi.org/10.1260/1369-4332.18.9.1427.

[3.32] Kang L, Ge H, Fang X. An improved ductile fracture model for structural steels considering effect of high stress triaxiality. Constr Build Mater 2016;115:634–50. https://doi.org/10.1016/J.CONBUILDMAT.2016.04.083.

[3.33] Kanvinde AM, Deierlein GG. Void growth model and the stress modified critical strain model to predict ductile fracture in structural steels. Journal of Structural Engineering 2006;132:1907–18. https://doi.org/10.1061/(asce)0733-9445(2006)132:12(1907).

[3.34] Hasunuma S, Miyata Y, Nita Y, Ogawa T. Low Cycle Fatigue Damage Developed on the Surface and Interior of Steels. TRANSACTIONS OF THE JAPAN SOCIETY OF MECHANICAL ENGINEERS Series A 2012;78:161–70. https://doi.org/10.1299/kikaia.78.161.

[3.35] Kamaya M, Kawakubo M. Damage due to Low-Cycle Fatigue of Type 316 Stainless Steel : Fatigue Life under Variable Loading and Influence of Internal Cracks. Transactions of the Japan Society of Mechanical Engineers Series A 2010;76:1048–58. https://doi.org/10.1299/kikaia.76.1048.

[3.36] Komotori J, Shimizu M. Grain size effect in low cycle fatigue of steel under mean strain. Proceedings of The 7th International Conference On Fracture (ICF7) 1989:1213–20. https://doi.org/10.1016/B978-0-08-034341-9.50135-2.

[3.37] Komotori J, Shimizu M. Fracture mechanism of ferritic ductile cast iron in extremely low cycle fatigue. Low Cycle Fatigue and Elasto-Plastic Behaviour of Materials 1998:39–44.

[3.38] Komotori J, Yokoyama M, Shimizu M. Microstructual effect on extremely low cycle fatigue of dual phase steel. Mechanical Behaviour of Materials VI, Proceedings of the Sixth International Conferrence, Kyoto, Japan 1993:517–23. https://doi.org/10.1016/b978-0-08-037890-9.50201-5.

[3.39] Kuwamura H. Transition between fatigue and ductile fracture in steel.

Journal of Structural Engineering 1997;123:864–70. https://doi.org/10.1061/(ASCE)0733-9445(1997)123:7(864).

[3.40] Shimada K, Komotori J, Shimizu M. Fracture Mode Transition and Damage in Extremely Low Cycle Fatigue. Low Cycle Fatigue and Elasto-Plastic Behaviour of Materials 1987:680–6. https://doi.org/10.1007/978-94-009-3459-7_105.

[3.41] Miner MA. Cumulative damage in fatigue. J Appl Mech 1945;12:159–64.

Chapter 4 Conclusions and Future Study

Outline for Chapter 4

4.1 Conclusions

This study experimentally investigates the low-cycle fatigue performances (LCF) of the 400 N/mm^2 (SS400), 490 N/mm^2 (SM490A), 590 N/mm^2 (SA440C) grade structural steels, specifically focus on the ELCF (strain amplitudes ≥ 8%) regime but in a continuous manner from LCF to ELCF regimes to provide a qualitative database for further researches. To enable the LCF test including large strains, first the parametric studies were conducted to obtain the optimal specimen shape for lage strain cyclic loadings. Using the specimen shape, the cyclic tests were performed on various strucural steels with strain amplitudes ranged from 2% to 12% which cover LCF and inlcuding very large plastic strain (Extremely LCF). Based on the results, the effect of steel materials on LCF performance was elucidated. In addition to that until fracture, the deformation capacity of steel materials up to the ultimate point is also investigated. The main conclusions of each chapter can be summarized as follows.

Summary for Chapter 2

The main objective of this chapter is to obtain the appropriate specimen shape used for LCF and ELCF tests. The parametric studies were conducted numerically and experimentally to obtain the optimal specimen shape for LCF tests including large strain amplitudes. It has been discovered that not only the reduced section to diameter ratio *Le*/*D*, but also the fillet radius to diameter *R*/*D* has beneficial and detrimental influences on the specimens. The following is the main conclusion.

- For specimens with $Le/D \geq 1.0$ and $R/D \geq 0.36$, the strain concentrates and stress distribute almost uniformly inside the reduced section *Le*.

- When $Le/D \geq 1.0$, neck can fully form inside the reduced section (since $Ln/Le \leq 1$), regardless of R/D. However, when $Le/D < 1.0$, neck length is longer than the reduced section ($Ln/Le > 1$). Besides, it is also observed neck length tends to increase with the increase in R/D. The trend, on other hand, is less significant when $Le/D \geq 1.0$.
- As Le/D ratios increase the bucking resistance of the specimen decreases. Specimens with small R/D ratios tend to have higher buckling resistance. Nevertheless, small R/D (< 0.75) may also lead to reduction in cross section at the corner under compressive strain which may affect the deformation capacity.
- Given stress & strain distributions, reduction in cross-section at R, neck and buckling resistance, the optimal range of Le/D and R/D ratios with the limit strain line of 9% are proposed. Consequently, the applicability of the proposed ratios and limit strain is also confirmed according to cyclic analyses, several material tests (using Type A-G specimens) and specimen shapes employed in previous studies.

Given the measurable range of the extensometer, Type G was used for further discussion on the low-cycle fatigue (LCF) and extremely LCF (ELCF) performances of various structural steels in the following chapters.

Summary for Chapter 3

The objective of chapter 3 is to investigate the low-cycle fatigue (LCF) and extremely low-cycle fatigue (ELCF) performances of structural steels with different strengths. In addition to that until fracture, the deformation capacity of steel materials up to the ultimate point is also investigated. By using appropriate specimen shape discussed in Chapter 2,

cyclic loading tests were conducted on structural steels with nominal tensile strengths of 400 N/mm^2, 490 N/mm^2 (SM490A) and 590 N/mm^2 (SA440C). To obtain test data of the studied steels in both small (2%) and large (12%) strain regions, constant amplitude strain-controlled cyclic loadings with tensile and compressive excursions were carried out. Although these structural steels have different strength levels, their chemical compositions are not much different. For the steels and loading conditions considered in this study, the key conclusions can be drawn as follows:

- In case of plotting the hysteretic curve in the nominal stress-strain relationship, the tensile and compressive stresses appear to lose their symmetry at strain of 4.5% or greater. By plotting in the true stress-strain relationship, stresses in both tension and compression sides are close to symmetry in a broader range of both small and large strain amplitudes. It can be said that the relationship of true stress and true strain is more appropriate in expressing the stress-strain hysteretic curves.
- A linear relationship was obtained for strains with amplitudes up to 3.5%. Additionally, the strain-life curve of two different lots of specimens tested with tension as the initial loading yielded a linear relationship in comparison with the specimen tested with compressive loading with small and large strain amplitudes, despite the minimal dispersion at moderate strains. In other words, one can consider that there are almost no significant effects of initial loading direction, specimen configuration, as well as different lots on the strain-life curve in the case of specimens and strain amplitudes considered in this study
- The LCF and ELCF performances of the considered (SS400, SM490A and SA440C) structural steels can be evaluated in a unified manner up to a strain amplitude of approximately 10%. Based on this result, data regression using a

power function was conducted to obtain the LCF equation for the considered structural steels.

- By defining the damage initiation (onset of crack or neck) as the ultimate point, the deformation capacity up to ultimate point of the considered structural steels (SS400, SM490A, SA440C) can be evaluated using one N_{di} equation from 2% to 12% strains.
- From the variable amplitude cyclic tests, the N_{di} equation was also confirmed to be validated under the seismic loads which are typically the loading patterns consisting of more than one amplitude.
- As an application of the materials' evaluation equations, the LCF performance of steel members (steel beam and Buckling-Restrained Brace) is also discussed in Appendix 1. However, the purpose is not to accurately evaluate a member based on the material's equation; rather, to demonstrate the performance calculated by the material's equation can be used as an indicator of the desired performance of the member. The result in Appendix 1 shows that material's N_{di} can be used as a benchmark for the performance that Buckling-Restrained Braces (BRBs) should aim for.

4.2 Future studies

Based on the discussion throughout chapters 2-3, future studies to advance the related research topic are discussed as follows.

Future study #1: Limitation of application of steel material test data onto the steel members.

As an application of the material's performance equations, the LCF performance of steel beam was discussed in Appendix 1. The performance of the steel beam is investigated by getting the strain at the critical part of the beam from the member in-plane analysis and applying it to material's N_{di} equation. The comparison of performance of the steel beams (with weld access hole connected to thick end plate) between test and calculated results based on N_{di} equation indicates both performance curves have the same slope. However, the performance of the beams is lower than that calculated using the material's equation. It should be noted that the strain at critical section obtained from the numerical analysis used is limited to average strain rather than the localized one. In this regard, the localized strain associated with more complicated constraints cannot be fully captured. Therefore, as a future study, it is necessary to quantitatively elucidate the rate of reduction or local strain concentration ratio of beam members due to effects such as local combined stresses using advanced finite element analysis program (e.g., Abaqus).

Future study #2: Simplified prediction model for steel members using Abaqus and material test data

In case of steel material tests, uniaxial LCF tests are typically conducted. However, for steel members, the stress states are more complicated. To apply the material test data to the steel members, some ductile fracture prediction models such as Johnson-Cook model [4.1], void growth model (VGM) [4.2], cyclic void growth model (CVGM) [4.3], stress

modified critical strain (SMCS) [4.2] have been proposed and widely used thus far. However, these methods necessitate highly skilled FEA users who can perform such analyses in conjunction with user subroutines (UMAT or VUMAT), which are not desired by engineers as general. For this reason, a more simplified model based solely on Abaqus's built-in function should be considered. For example, consider an evaluation method based on the quantification of the correlation between equivalent plastic strain (PEEQ) and stress triaxiality (TRIAX) at the critical part and material test data. The cumulative plastic strain of the skeleton part or overall should be considered for material test data. Additionally, the cumulative plastic strain up to the ultimate point should be considered in addition to that up to the fracture.

Future study #3: Optimal flat specimen shape subjected to large tensile and compressive strain should be investigated.

Although only round specimen with uniform-gauge test section (in Chapter 2) is considered in this study, there are chances that specimens with rectangular cross-section are employed more for it is easy to be manufactured. For this reason, the optimal specimen shape of such specimens should be also clarified in the future studies.

References for Chapter 4

[4.1] Johnson GR, Cook WH. Fracture characteristics of three metals subjected to various strains, strain rates, temperatures and pressures. Eng Fract Mech 1985;21:31–48. https://doi.org/10.1016/0013-7944(85)90052-9.

[4.2] Kanvinde AM, Deierlein GG. Void growth model and the stress modified critical strain model to predict ductile fracture in structural steels. Journal of Structural Engineering 2006;132:1907–18. https://doi.org/10.1061/(asce)0733-9445(2006)132:12(1907).

[4.3] Kanvinde AM, Deierlein GG. Cyclic void growth model to assess ductile fracture initiation in structural steels due to ultra low cycle fatigue. J Eng Mech 2007;133:701–12. https://doi.org/10.1061/(ASCE)0733-9399(2007)133:6(701).

Appendices

Appendix 1 Investigation of Steel Members Using Performance Calculated from the Material Evaluation Equation as a Benchmark

A1.1 Introduction

In this chapter, the low-cycle fatigue (LCF) performance of steel members (i.e., Buckling-Restrained Brace and steel beam) will be investigated in terms of the materials' performance equations as an application of the materials' data. It is worth noting that the main goal of the dissertation is to investigate the LCF performances of various structural steels, including very large plastic strains. As a result, the purpose of this chapter is not to accurately evaluate steel member performance based on the material's equation; rather, to demonstrate the performance calculated by the material's equation can be used as a benchmark for the performance for which the members should aim.

A1.2 Comparison with LCF performance of Buckling-Restrained Brace

When compared to normal steel braces, which buckle under significant lateral loads induced by earthquakes and wind, the instability-suppressed BRB (Buckling-Restrained Brace) can attain nearly the same strength and stiffness under tension and compression. Therefore, BRB have enhanced energy dissipation capacity and are commonly employed as seismic members. A thorough understanding of low-cycle fatigue performance of BRB will enable structural designers to estimate the remaining life of BRB after the earthquake. Although BRB is said to be buckling suppressed, there are still high-mode buckling patterns between clearances inside the plastic zone. This reduces the performance of the BRB compared to that of the material under the same uniaxial loading condition. For the time being, it is challenging to precisely evaluate the performance of BRB using material evaluation equations. However, for future studies on improving the performance of BRB, the material evaluation equations obtained in this study can be used as an indicator of the desired performance of the member. In this section, the LCF of several BRBs used in

previous studies [A1.1–A1.12] is compared to that of steel materials to examine the performances when different shapes, width-to-thickness ratios, and plastic zones are considered.

Table A1.1 shows the BRB database considered in this study. The data is arranged in the order of small to large width-to-thickness (B/t or D/t) ratios and renamed as Groups A – J including reference numbers.

The LCF performances of BRBs and steel materials are shown in Fig. A1.1. For comparison, the LCF equations for BRB available in the recommended provisions for seismic damping systems applied to steel structures (Seshinsekkei) [A1.10] are also plotted in this figure. Seishinsekkei (Average) refers to the Eq. A1.1. In this equation, ε_a indicates the half amplitude of axial strain. Seishinsekkei (Upper) and (Lower) represents the 3 and 1/3 times the LCF curve of Eq. A1.1, respectively. Since the number of cycles up to 95% ultimate strength are primarily considered in the provision [A1.10], N_{di} equation of material is also shown.

LCF performance equation for BRB [A1.10]:

$$\varepsilon_a = 0.05108\left(N_f / 2\right)^{-0.385} \tag{A1.1}$$

Table A1.1 List of BRB database used

Name	**Steel material**	**BRB shape**	***D*/*t* or *B*/*t***	**Plastic zone (mm)**
Group A1 [A1.11]	SN400B	―	7	1176
Group A2 [A1.11]	SN400B	―	7, 11	1251
Group B [A1.12]	SN490B	―	7	2054, 2174
Group C [A1.1]	LY225	|	7, 11	1445
Group D [A1.2]	SN490B	H	7.5	1300
Group E [A1.3]	SN400B	+	9.4	2400
Group F[A1.4]	SN400	=	9.7	1330
Group G [A1.5]	SN400B	―	10	700
Group H [A1.6, A1.7]	SKTM13A (400 N/mm^2 grade)	◎	19, 24	N.A.※
Group I [A1.8]	SN400B, SN490B	|	N.A.	N.A.
Group J [A1.9]	SN400B, SN490B	―, +	N.A.	N.A.

※ N.A. indicates Not Available

The comparison between BRB and material in Fig. A1.1 indicates that the LCF performances of the considered database are scattered over the upper and lower limits of the Seshinsekkei equations for BRB. Also, the LCF performances of BRB are lower than those of N_{di} and N_f for material. It is also observed from Fig. A1.1 that the slopes of LCF curves of materials and Seshinsekkei are identical. While Seshinsekkei (Average) equation for BRBs is typically 9.5%—15% ${}_{material}N_f$ and 23%—27% ${}_{material}N_{di}$. Previous study [A1.11] has indicated the LCF performance of BRB is approximately 10% to 25%when compared to LCF crack of the steel material. The LCF performance of the BRB tends to be lower than the experimental results for the material due to the effects of uneven waveform, strain concentration and local buckling. As a result, the BRB's performance is regarded as excellent when approaching 1.0.

Figs. A1.2 and A1.3 illustrate the difference between the performances of BRBs from database and steel materials. When n_f ($={}_{BRB}N_f / {}_{material}N_f$) and n_{di} ($={}_{BRB}N_f / {}_{material}N_{di}$) are equal to one, it means that the LCF performance of BRB is the same as that of steel. From Figs. A1.2 and A1.3, it is observed that the difference is ranged from 4% to 32% for n_f and 9% to 71% for n_{di}. This difference may be contributed to the presence or absence of welds, the setting of the unbonded material and clearance, and the width-to-thickness ratios as well as the plastic zone of the core material, which was also reported in [A1.10]. According to this result, it can be said the closer the performance of BRB is to the material's equation, the better. Compared to N_f, the N_{di} of material was found to be a better benchmark when investigating the performance of BRB.

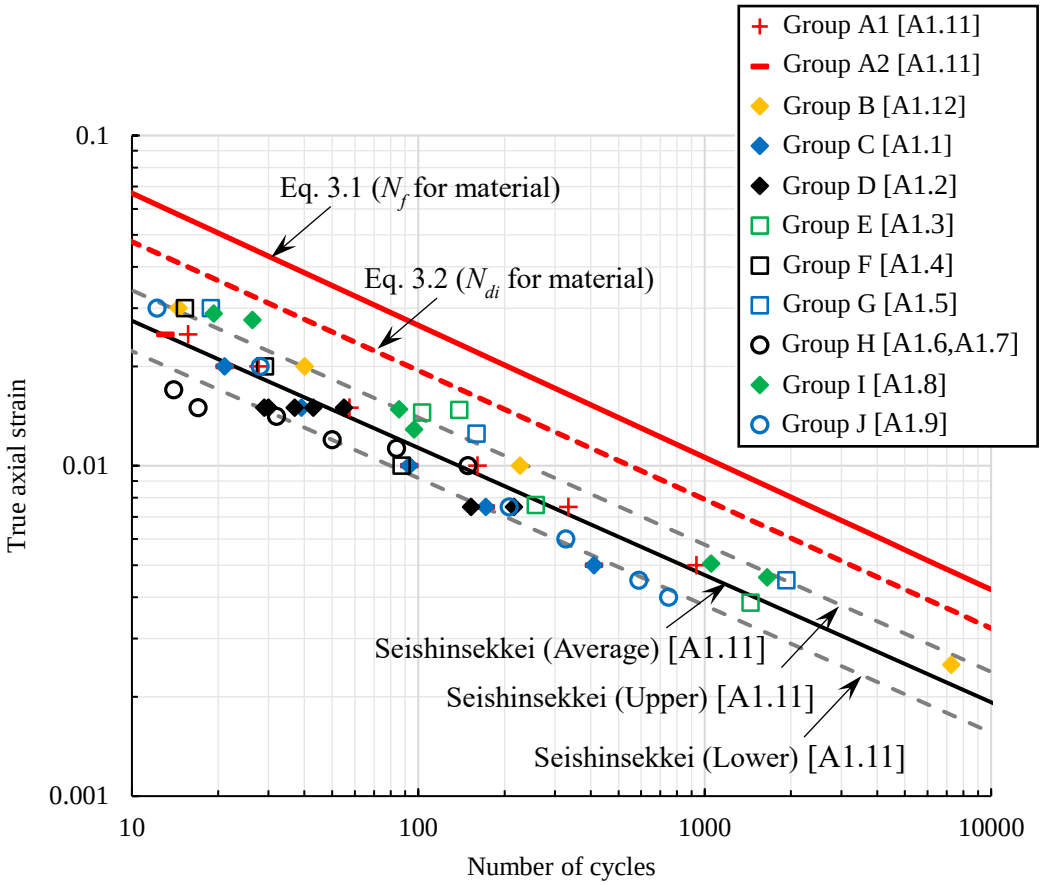

Fig. A1.**1** LCF performances of BRBs and steel material

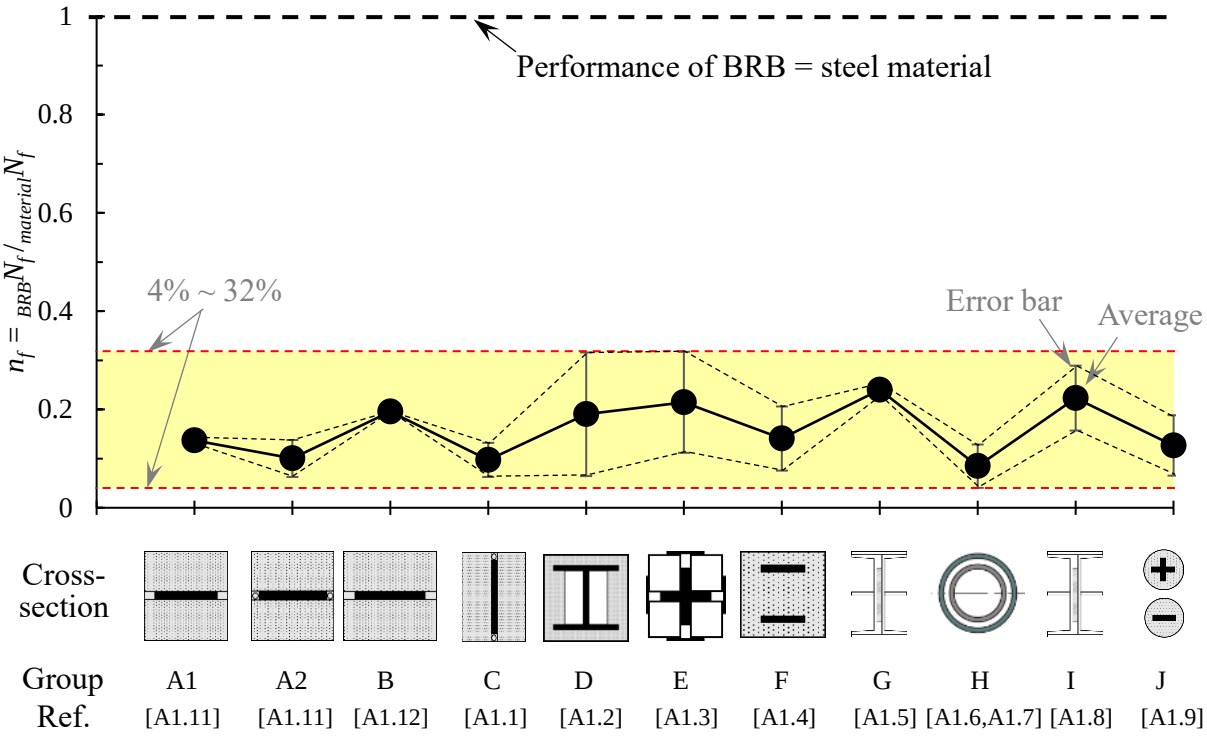

Fig. A1.2 Difference between N_f of BRBs and N_f of materials

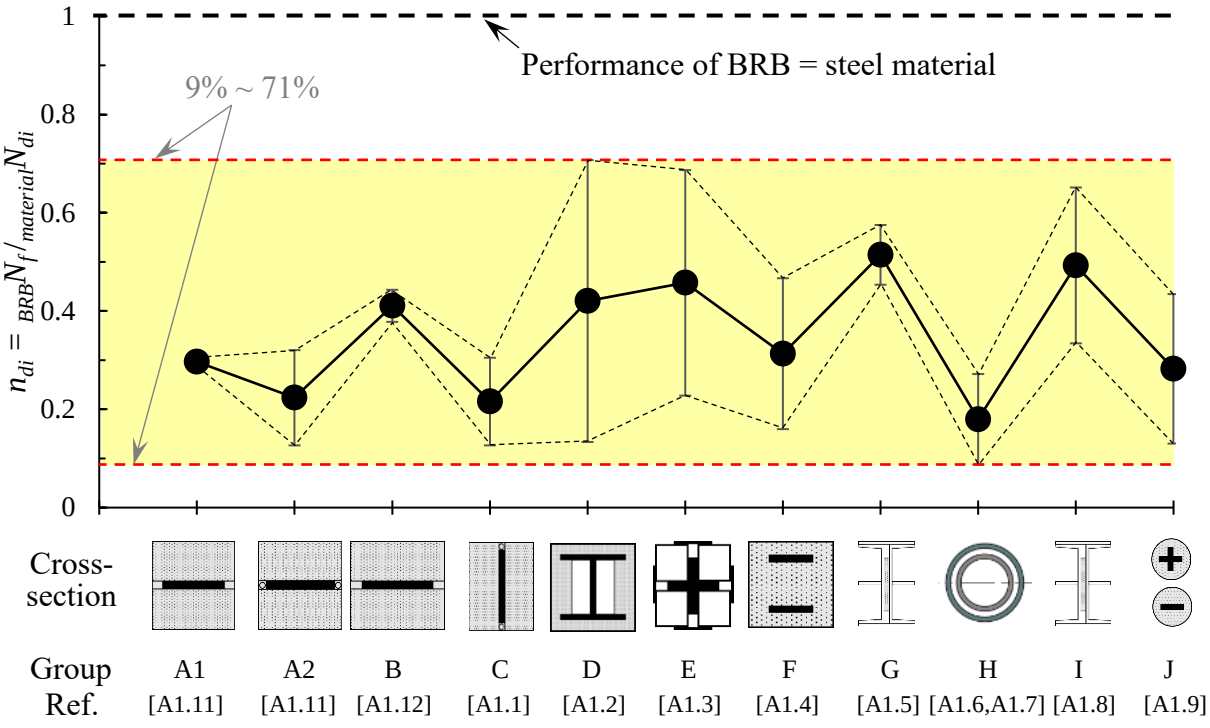

Fig. A1.3 Difference between N_f of BRBs and N_{di} of materials

A1.3 Numerical analyses on steel beams

This section discusses the numerical analyses on steel beams. Based on the analytical result, the LCF performance of steel members is examined in terms of the performance calculated from the material's N_{di} equation. However, the purpose is not to precisely evaluate the steel beam; rather, to demonstrate the performance calculated by the material's equation can be used as a benchmark for the performance for which the members should strive.

A1.3.1 Analytical method

Under severe earthquakes, the fracture at the beam end (as shown in Fig. A1.4) is observed as the typical failure mode. By getting the strain at this critical part of the beam from the member in-plane analysis and applying it to material's N_{di} equations, the LCF performance of the steel beam is investigated.

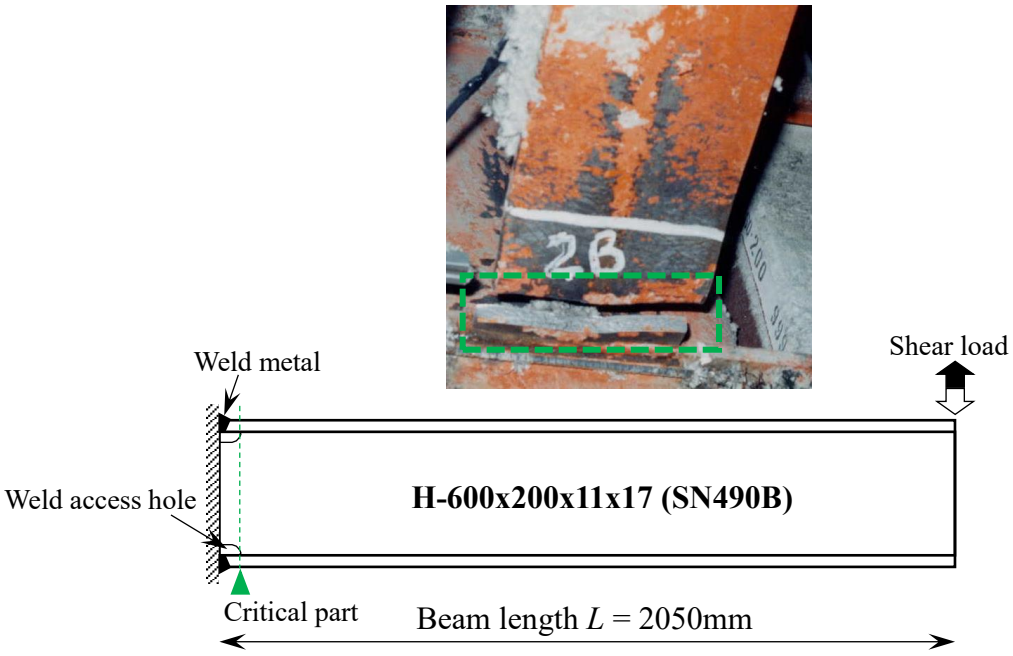

Fig. A1.4 Critical part of the steel beam

Basic assumption of in-plane analytical method [A1.13, A1.14]

The in-plane analysis of the cantilever wide-flange beams subjected to cyclic loading histories was conducted under following assumptions:

(1) The assumption of the plane section

(2) The deformation due to shear force is considered to be always elastic

(3) There is no out-of-plane deformation of the beam

(4) The beam reaches its maximum load without local buckling

(5) The decrease in moment transfer efficiency due to the out-of-plane deformation of the column flange is negligible.

Analytical algorithm

The algorithm of this numerical analysis [A1.13, A1.14] is based on the monotonic in-plane analyses in the previous literatures [A1.15– A1.17]. The basic idea of the algorithm is to obtain the moment-curvature ($M-\phi$) relation (see "Appendix 2") of a certain beam section through the internal force balance under the assumption of the plane section (Fig. A1.5). Moreover, the load-deformation ($M-\theta$) relation (see "Appendix 2") of the beam can be derived by integrating the moment-curvature relation along the beam span (Fig. A1.6). This analytical method is known to be sufficiently accurate before the beam reaches its maximum strength.

Mesh generation

As shown in Fig. A.7, the flange of the beam was divided into 5 elements in the plate thickness direction, whereas the web was divided into 33 elements in the height direction. Furthermore, the beam was divided into the element size of 10-mm in the longitudinal

direction.

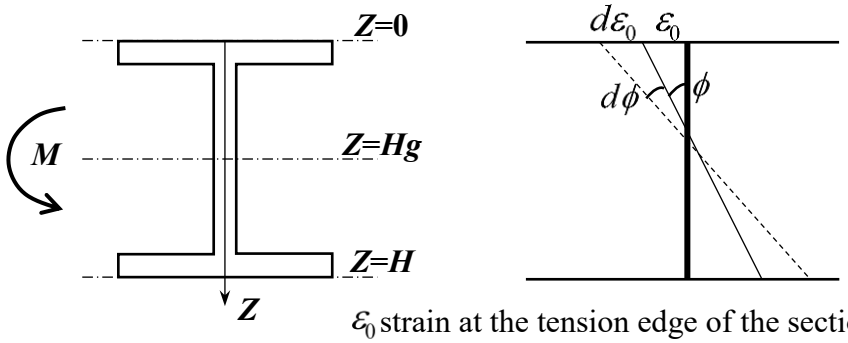

ε_0 strain at the tension edge of the section
ϕ curvature
Hg distance from the tension edge to the center of gravity

Fig. A1.5 Internal force balance of the beam

.

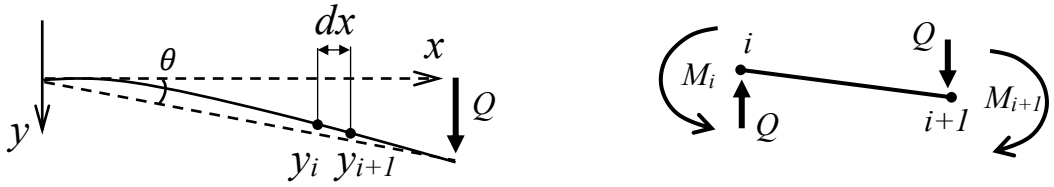

Fig. A1.6 Mesh generation along the beam span

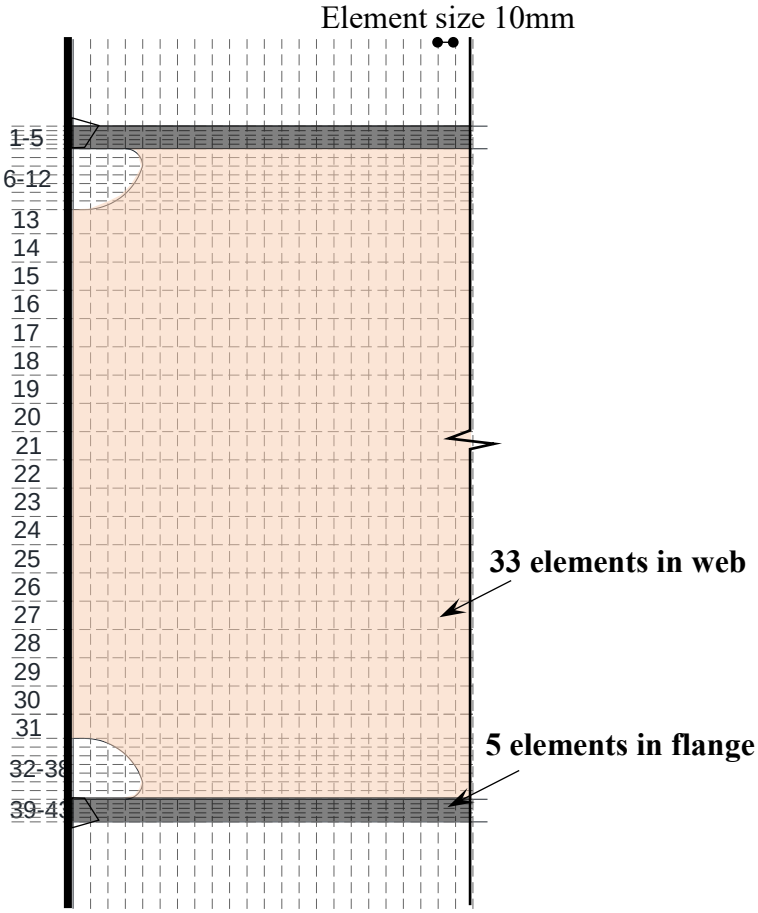

Fig. A1.7 Mesh generation at the beam flange and web

A1.3.2 Analytical parameters

The beam analytical model is shown in Figure A1.10. The beam used in previous study [A1.18] has a wide flange section of 600 mm (depth) x 200 mm (width) x 11 mm (web thickness) x 17 mm (flange thickness) and made from SN490B steel grade (nominal yield strength is 325 N/mm^2 and nominal tensile strength is 490 N/mm^2). The beam is connected to the column using an end plate (with a thickness of 50 mm) type connection. In this regard, it can be said that the decrease in moment transfer efficiency due to the out-of-plane deformation of the column flange is negligible.

The nominal stress and strain curve shown in Fig. A1.8 up to the tensile strength are converted into true stress and true strain curve. Then, this curve is input as the material properties for the numerical analysis. Four peak-to-peak constant amplitudes $3\theta_p$, $2.5\theta_p$, $2\theta_p$ are employed as the target rotation angles. θ_p is shown in Table A1.3.

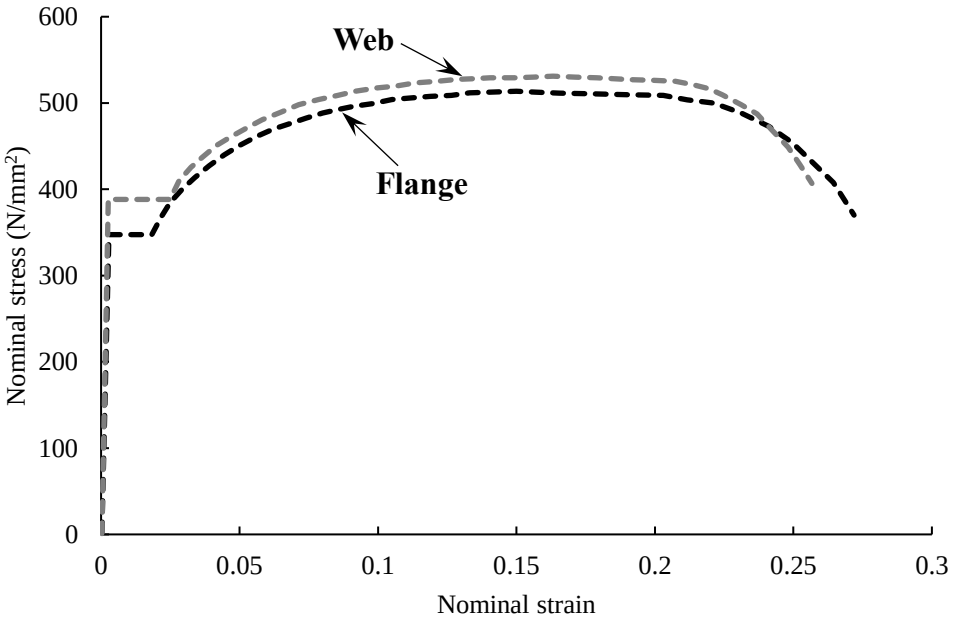

Fig. A1.8 Nominal stress vs. nominal strain curve

A1.3.3 Comparison between test and analytical results

Comparison of load-deformation relationship

Fig. A1.9 shows the moment (M) - rotation angles (θ) from the test and analytical results as well as strain histories at the critical part obtained from numerical results at rotation angles of 0.02 rad, 0.025 rad, 0.03 rad.

This figure shows that the M - θ relation of test and analytical results have good correspondence. In this regard, it can be said that the in-plane numerical analysis used can reasonably reproduce the test result. Because the strain history is not available in the literature [A1.18], the strain history generated from the verified analytical approach is used in N_{di} equation of materials for further discussion of steel beam performance evaluation.

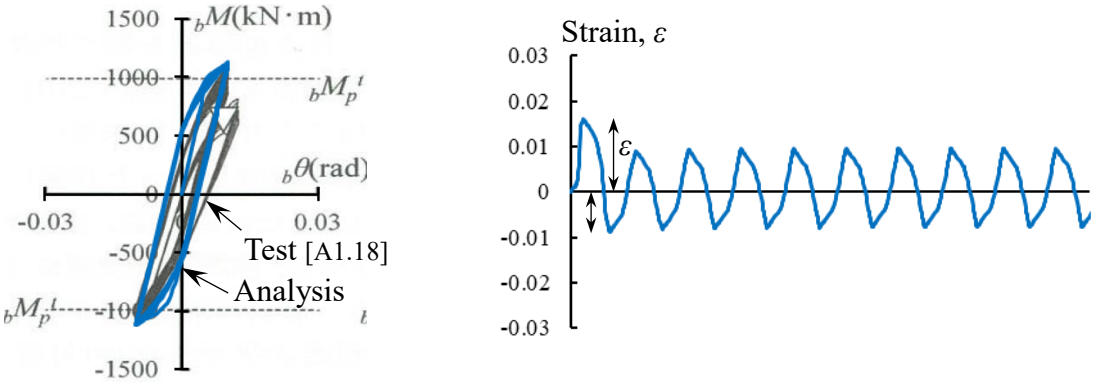

(a) rotation angle 2 θ_p

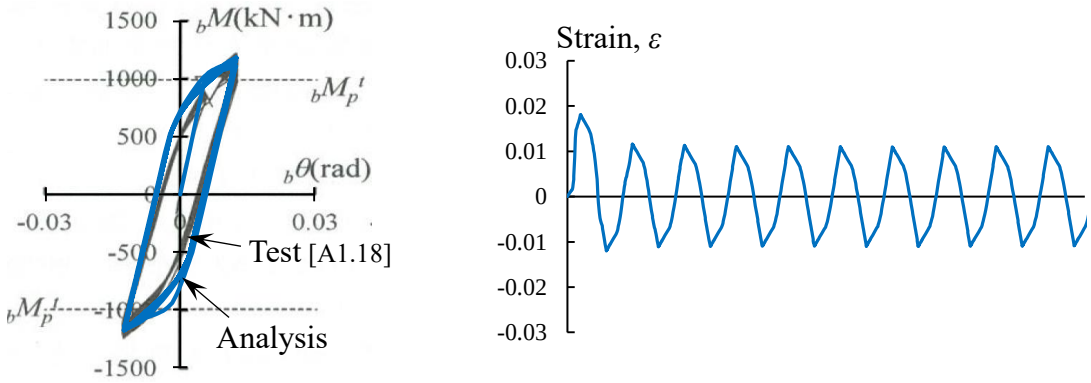

(b) rotation angle 2.5 θ_p

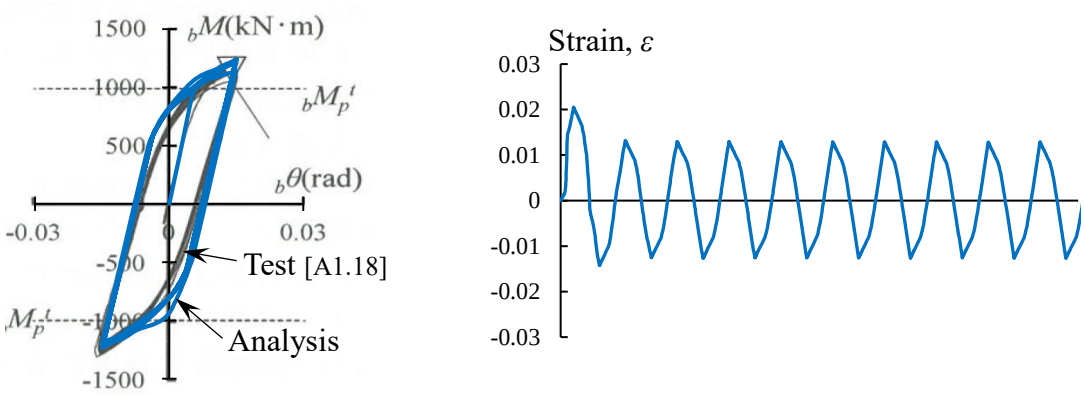

(c) rotation angle 3 θ_p

Fig. A1.9 Moment-rotation angle relations and strain history at critical part

Comparison of LCF performances

To evaluate the LCF performance of beams, each half amplitude of the strain history at the critical part as shown in Fig. A1.9a is used to apply into Miner's rule (Eq. A1.1) and the N_{di} equation (Eq. A1.1) for steel materials. It should be noticed that, for the in-plane analysis program used, strain at the critical part is calculated as the average value (not localized region) in the beam width direction. D is the cumulative damage value, and fracture is considered when $D = 1$.

$$N_{di} = \left(\frac{0.117}{\varepsilon} \right)^{1/0.39} \tag{A1.1}$$

$$D = \sum_{i=1}^{x} \frac{0.5}{N_{di}} \tag{A1.2}$$

The number of cycles at any arbitrary x when $D = 1$ is considered to be the LCF performance of steel beams. This calculated number of cycles is used to compare with the number of cycles to fracture of the beam test result at each rotation angle as shown in Fig. A1.10. Table A1.2 shows the number of cycles at each rotation angle obtained from test and calculated results.

As illustrated in Fig. A1.10, the steel beam LCF performance is generally represented by the number of cycles and rotation angles in the vertical and horizontal axes, as opposed to steel materials and BRBs. The comparison of LCF performance of the steel beams between test and calculated results in the figure indicates both LCF curves have the same slope, and their number of cycles are about 3.2 – 3.8 times different. This difference is deemed to be contributed by the decrease in moment transfer efficiency due to the loss of web section by the weld access hole. The multiaxial constraint in the localized region of the steel beam due to shear force may also cause this difference. It is worth noting that

the beam in-plane analysis program used has the limitation that it can only consider the average strain in the direction of the flange width at the critical part. Therefore, as a future study, it is necessary to quantitatively elucidate the rate of reduction or local strain concentration ratio of beam members due to effects such as local combined stresses using advanced finite element analysis program.

Table A1.2 Number of cycles at each rotation angle

Beam section	Rotation angle (rad)	${}_{mem}N_f$ (test)	N_{di} equation	$N_{di}/{}_{mem}N_f$
	$3\theta_p$ (θ_p = 0.0075)	44	167	3.79
H-600x200x11x17	$2.5\theta_p$ (θ_p = 0.0077)	74	261	3.53
	$2\theta_p$ (θ_p = 0.0076)	137	441	3.22

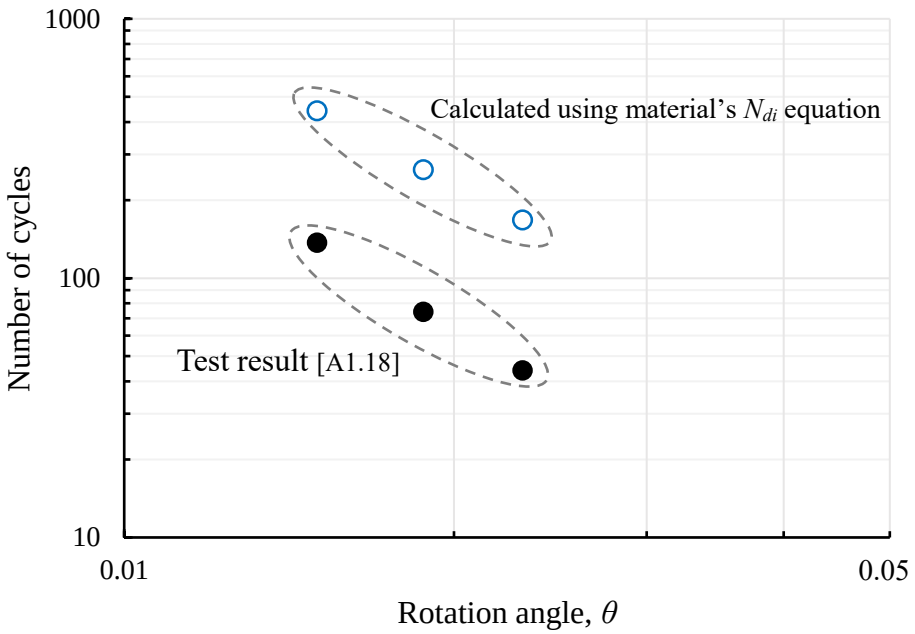

Fig. A1.10 Comparison of LCF performances between test and calculated results

A1.3.4 Effect of tensile stress-strain relationships

This section investigates the effect of tensile stress and strain relations on the analytical results. In most cases, the stress and strain curves from the tensile tests are not available in the literatures. Therefore, it is difficult to reasonably simulate the test result only with the yield strength and tensile strength, for example given the effect of shape of the stress-strain curve.

To examine the effect of stress-strain relations, bilinear model with known yield strength, tensile strength and uniform elongation are considered. The uniform elongation *ue* is taken as the parameters and changed from 25% to 150% as shown in Fig. A1.11 for beam flange. For example, 1.0ue refers to the bilinear model with uniform elongation equals that of the test [A1.18].

Fig. A1.12 shows the average (tensile and compressive side) moment at each uniform elongation. The moment tends to decrease with the increase in *ue*, and the significant difference is observed when *ue* is 0.5% or smaller. On the other hand, Fig. A1.13 exhibits that the strain tends to increase with the increase in *ue*, which is opposite to the trend of moment. Therefore, the LCF performances of the steel beams also decrease as the uniform elongation increase as illustrated in Fig. A1.14. Nevertheless, Figs. A1.13 and A1.14 indicates that the results of the beam using bilinear model with 1.0*ue* are similar with that using the tensile stress-strain curve from the test results.

This result suggests that the effect of tensile stress-strain relations on the analytical result is significant. In case of the stress-strain curve is not available, if unavoidable, the bilinear model with known yield strength, tensile strength and uniform elongation may also be used for numerical simulation. Once again, the stress-strain curves from tensile tests are essential for reasonable simulations.

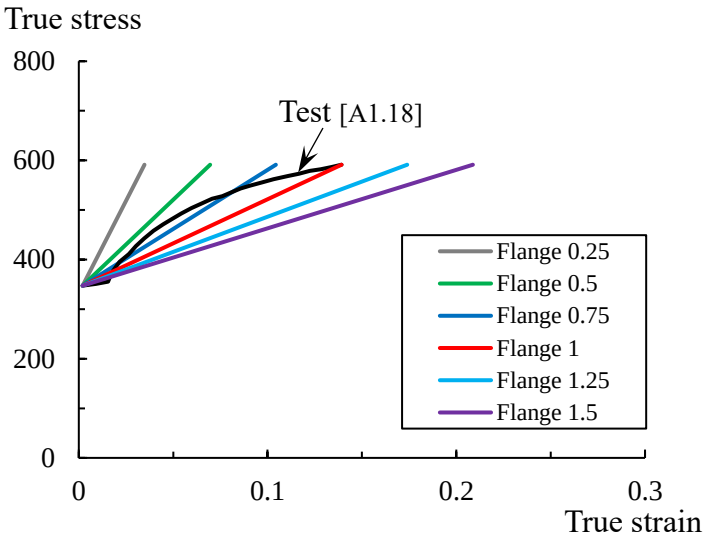

Fig. A1.11 Parametric uniform elongations

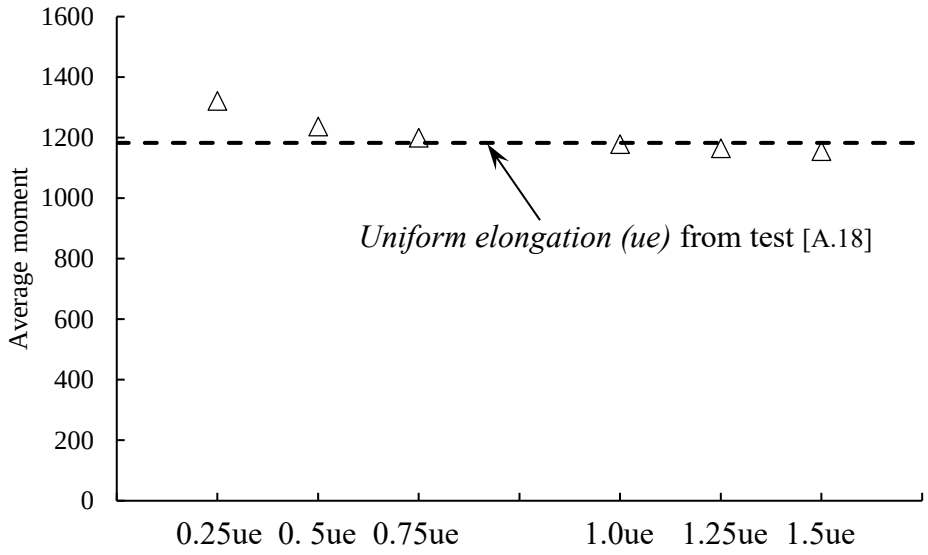

Fig. A1.12 Average moment at different uniform elongations

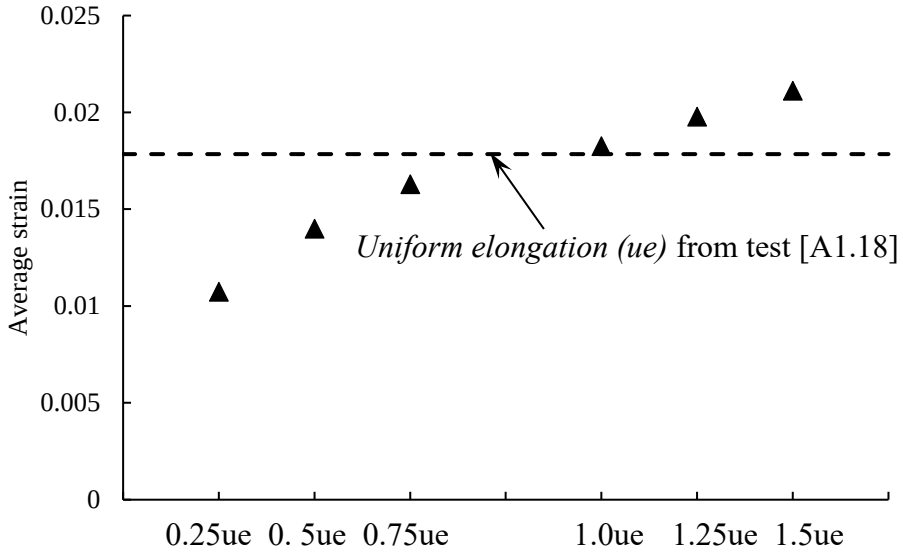

Fig. A1.13 Average strain at different uniform elongations

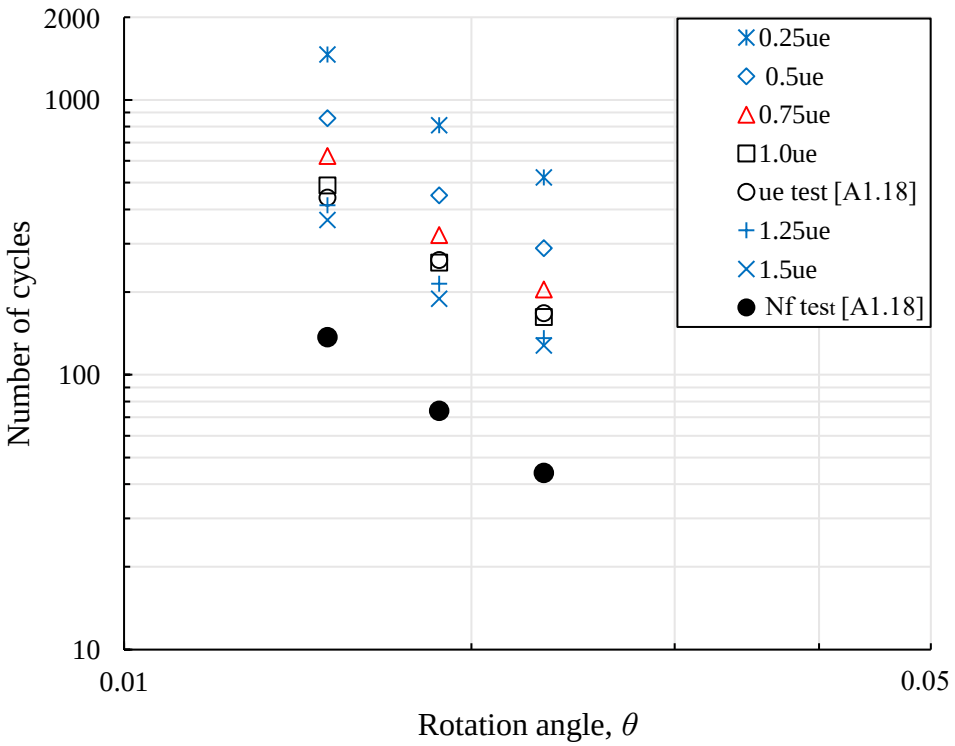

Fig. A1.14 LCF performances of beam considering effect of stress-strain relations

References for Appendix 1

[A1.1]Koya Y, Ene D, Ito T, Makita T. Tests on damping braces by concrete filled channel steel. Hazama Ando Technical Research Report 2018;6:1–6.

[A1.2]Obara I, Sasaki S, Sasaki Y, Miura Y, Otsuka Y. Experimental study on buckling-restrained brace using H-shaped steel - Part 3 Fatigue performance. Fujita Technical Research Report 2019;55:19–24.

[A1.3]Narihara H, Tsujita Osamu, Yasuda Satoshi. The experimental study on buckling-restrained brace (Part 4 Low cycle fatigue test on aseismic brace with SN400B, SN490B). Architectural Institute of Japan, Summaries of Technical Papers of Annual Meeting (Hokuriku) 2002:555–6.

[A1.4]Kubota J, Tagami J, Kurino H, Inoue T, Sawamoto Y. The experimental study on structural behavior of buckling restrained braces with universal joints. Architectural Institute of Japan, Summaries of Technical Papers of Annual Meeting (Tohoku) 2018:715–6.

[A1.5]Horie T, Mase S, Terada T. Development of unbonded brace damper restrained by channel section steel (Part 5 Low cycle fatigue tests on unbonded brace damper with SN400B). Architectural Institute of Japan, Summaries of Technical Papers of Annual Meeting (Tokai) 2003:767–8.

[A1.6]Ishii T, Takaki N, Fujisawa K, Shimizu T, Miyagawa K, Kitamura W. Low-cycle fatigue performance of tube-in-tube braces buckling-restrained (Part 1 Test results). Architectural Institute of Japan, Summaries of Technical Papers of Annual Meeting (Tokai) 2012:781–2.

[A1.7]Takaki N, Fujisawa K, Ishii T, Shimizu T, Kitamura W, Miyagawa Kazuaki. Low-cycle fatigue performance of tube-in-tube braces buckling-restrained (Part 2 Fatigue performance). Architectural Institute of Japan, Summaries of Technical Papers of Annual Meeting (Tokai) 2012:783–4.

[A1.8]Ishii M, Uehara S, Ogi Y, Morishita K. Hysteresis dampers for controlling seismic response of bridges and structures. Mitsubishi Heavy Industry Technical Research Report 2005;42.

[A1.9]Terashima M. Full-scale experiments of unbonded braces with large axial force capacity. Architectural Institute of Japan, Summaries of Technical Papers of

Annual Meeting (Tokai) 2021:1003–4.

[A1.10] Recommended provisions for seismic damping systems applied to steel structures. Architectural Institute of Japan; 2014.

[A1.11] Koyano K, Nakagomi T, Midorikawa M, Iwata Mamoru. Fatigue performance of the buckling-restrained brace using steel mortar planks. Journal of Structural and Construction Engineering, AIJ 2017;82:921–8.

[A1.12] Nishimura E, kikuta S, Kawamata T, Hirai H, Honda J. Experimental study on buckling-restrained braces of damping type. Toda Technical Research Report 2018;44:7.1-7.6.

[A1.13] Yamada S, Jiao Y. A concise hysteretic model of structural steel considering the Bauschinger effect. International Journal of Steel Structures 2016;16:671–83. https://doi.org/10.1007/s13296-015-0134-9.

[A1.14] Yamada S, Jiao Y, Lee D-S, Ishida T, Kishiki S. A concise hysteretic model of 590 N/mm^2 grade high performance steel considering the Bauschinger effect. International Journal of Steel Structures 2020;20:1979–88. https://doi.org/10.1007/s13296-020-00401-w.

[A1.15] Kato B, Akiyama H. The ultimate strength of the steel beam-column (Part 4). Transactions of the Architectural Institute of Japan 1968;151:15-20,70. https://doi.org/10.3130/aijsaxx.151.0_15.

[A1.16] Yamada S, Akiyama H. Deteriorating behavior of steel members in post-buckling range. Structural Stability and Design, Balkema, Rotterdam 1995:169–74.

[A1.17] Yamada M, Sakae K, Tadokoro T, Shirakawa K. Elasto-plastic bending deformation of wide flange beam-columns under axial compression, Part I: Bending moment-curvature and bending moment-deflection relations under static loading. Journal of Structural and Construction Engineering, Transactions of the AIJ 1966;127:8–14.

[A1.18] Japanese Society of Steel Construction: Safety Assessment Methods for Steel Beam at Welded Ends against Long-Period Earthquake Ground Motions. JSSC Technical Report 2016:45–6.

Appendix 2: In-plane analytical method

Basic assumption of in-plane analytical method [A2.1, A2.2]

The in-plane analysis of the cantilever wide-flange beams subjected to cyclic loading histories was conducted under following assumptions:

(1) The assumption of the plane section

(2) The deformation due to shear force is considered to be always elastic

(3) There is no out-of-plane deformation of the beam

(4) The beam reaches its maximum load without local buckling

Analytical algorithm

The algorithm of this numerical analysis [A2.1, A2.2] is based on the monotonic in-plane analyses in [A2.3– A2.5]. The basic idea of the algorithm is to obtain the moment-curvature ($M-\phi$) relation of a certain beam section through the internal force balance under the assumption of the plane section. Moreover, the load-deformation ($M-\theta$) relation of the beam can be derived by integrating the moment-curvature relation along the beam span. This analytical method is known to be sufficiently accurate before the beam reaches its maximum strength. This in-plane analytical method also employed steel hysteresis model considering the Bauschinger effect proposed in [A2.1, A2.2], which is also summarized in Appendix A3.

The calculation of moment-curvature relationship and moment-rotation relationship can be obtained as follows.

Calculation of moment-curvature relationship:

The moment-curvature relationship of a specific section was obtained by the internal

force balance in the beam section. Fig. A2.1 shows the internal force balance of the beam section. The width of the beam section is the function of the distance from the section tension edge $g(Z)$. The stress value at each point in this section is the function of the strain value at that point $f(\varepsilon)$. Therefore, the axial force P and bending moment M can be written as:

$$P = \int_0^H f(\varepsilon) \cdot g(Z) dz = \int_0^H f(\varepsilon + \phi \cdot Z) \cdot g(Z) dz \quad (A2.1)$$

$$M = \int_0^H f(\varepsilon) \cdot g(Z) \cdot Z dz - P \cdot H_g = \int_0^H f(\varepsilon + \phi \cdot Z) \cdot g(Z) \cdot Z dz - P \cdot H_g \quad (A2.2)$$

by giving the section a small curvature increment $d\phi$, Eqs. A2.1 and A2.2 change to:

$$P + dP = \int_0^H f(\varepsilon + d\varepsilon_0 + (\phi + d\phi) \cdot Z) \cdot g(Z) dz \quad (A2.3)$$

$$M + dM = \int_0^H f(\varepsilon + d\varepsilon_0 + (\phi + d\phi) \cdot Z) \cdot g(Z) \cdot Z dz - P \cdot H_g \quad (A2.4)$$

Where $d\varepsilon_0$ is the increment of tension edge strain. The steel beams were subjected to pure bending, therefore, $P = 0$, $dP = 0$. Eqs. A2.3 and A2.4 were derived using Taylor series expansion. Terms after the 2nd term are considered negligible.

Through Eqs. A2.5 and A2.6, the moment curvature relationship can be obtained.

$$d\varepsilon_0 = \frac{\int_0^H f(\varepsilon + \phi \cdot Z) \cdot g(Z) \cdot Z dz}{\int_0^H f'(\varepsilon + \phi \cdot Z) \cdot g(Z) dz} d\phi \quad (A2.5)$$

$$dM = \int_0^H f'(\varepsilon_0 + \phi \cdot Z) \cdot (d\varepsilon_0 + d\phi \cdot Z) \cdot g(Z) \cdot Z dz \quad (A2.6)$$

Calculation of the moment-rotation relationship:

The moment-rotation relationship of the beam was derived by integrating the moment-curvature relationship along the beam span. The beam was divided into meshes 10 mm in size. In a certain mesh No. [*i*, *i*+1], the boundary condition is shown in Fig. A2.2. The

curvature of a certain mesh is considered constant. Therefore,

$$y'' = \phi_i \tag{A2.7}$$

$$\theta = y' = \phi_i \cdot x + C_1 \tag{A2.8}$$

$$y = 0.5 \cdot \phi_i \cdot x^2 + C_1 x + C_2 \tag{A2.9}$$

for mesh No i, suppose the boundary condition θ_i and y_i are known, then

$$\theta_{i+1} = \theta_i + \phi_i \cdot \Delta x \tag{A2.10}$$

$$y_{i+1} = y_i + \theta \cdot \Delta x + 0.5 \cdot \phi_i \cdot \Delta x^2 + \frac{Q \cdot \Delta x}{G \cdot A_w} \tag{A2.11}$$

Where is G shear stiffness, and A_w is the area of the beam web. Also, from the force balance in mesh No. i, the moment of i+1 point can be obtained by Eq. A2.12

$$M_{i+1} = M_i - Q \cdot \Delta x \tag{A2.12}$$

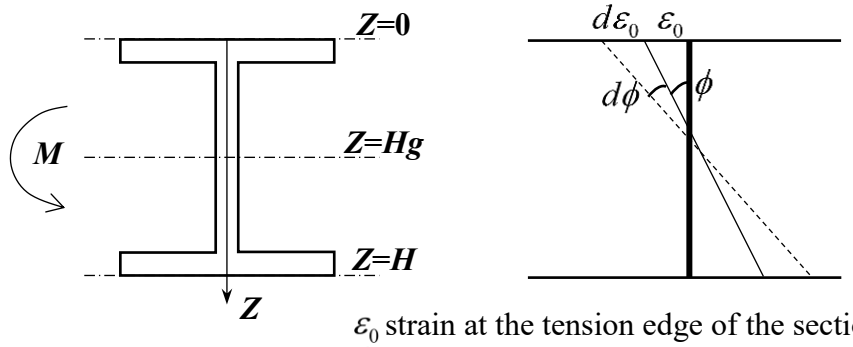

ε_0 strain at the tension edge of the section
ϕ curvature
Hg distance from the tension edge to the center of gravity

Fig. A2.1 Internal force balance of the beam section

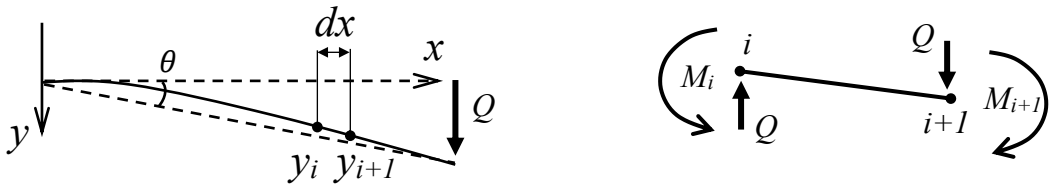

Fig. A2.2 Mesh generation along the beam span

References for Appendix 2

[A2.1] Yamada S, Jiao Y. A concise hysteretic model of structural steel considering the Bauschinger effect. International Journal of Steel Structures 2016;16:671–83. https://doi.org/10.1007/s13296-015-0134-9.

[A2.2] Yamada S, Jiao Y, Lee D-S, Ishida T, Kishiki S. A concise hysteretic model of 590 N/mm^2 grade high performance steel considering the Bauschinger effect. International Journal of Steel Structures 2020;20:1979–88. https://doi.org/10.1007/s13296-020-00401-w.

[A2.3] Kato B, Akiyama H, Uchida N. Ultimate strength of structural steel members (I). Transactions of the AIJ 1966;119:22–30.

[A2.4] Yamada M, Sakae K, Tadokoro T, Shirakawa K. Elasto-plastic bending deformation of wide flange beam-columns under axial compression, Part I: Bending moment-curvature and bending moment-deflection relations under static loading. Journal of Structural and Construction Engineering, Transactions of the AIJ 1966;127:8–14.

[A2.5] Yamada S, Akiyama H. Deteriorating behavior of steel members in post-buckling range. Structural Stability and Design, Balkema, Rotterdam 1995:169–74.

Appendix 3: Steel Hysteresis Model [A3.1, A3.2]

Previous studies [A3.1, A3.2] have reported the details of the hysteresis model of steel and then been summarized in [A3.3], which is reprinted as follows.

- The hysteretic curve under cyclic loading of steel was decomposed into the skeleton curve, the Bauschinger and the elastic unloading arts as shown in Fig. A3a.
- The skeleton curve was formed by sequentially connecting the paths of the loads that exceeded the maximum load obtained in the preceding cycle. This was adopted in the hysteresis model as the true stress-true strain relationship derived from the nominal stress-nominal strain relationship of the coupon test using Eqs. A3.1 and A3.2. Where ${}_t\sigma$ and ${}_n\sigma$ are the true and nominal stresses, ${}_t\varepsilon$ and ${}_n\varepsilon$ indicates the true and nominal strain.

$${}_t\sigma = (1+{}_n\varepsilon)\cdot{}_n\sigma \tag{A3.1}$$

$${}_t\varepsilon = \ln(1+{}_n\varepsilon) \tag{A3.2}$$

- The Bauschinger parts were softened due to the Bauschinger effect and modeled as bilinear (Fig. A3b). The model involves stress when entering the skeleton curve ${}_t\sigma_{Bs}$, elastic stiffness E, plastic strain increments in each cycle of the Bauschinger part $\Delta_t\varepsilon_B$, and stress of the stiffness changing point ${}_t\sigma_E$. Among them, ${}_t\sigma_{Bs}$ was set as the maximum stress from the previous cycle, and $\Delta\varepsilon_B$ can be calculated using Eqs. A3.3 and A3.4. $\sum\Delta_t\varepsilon_s$ denotes the cumulative plastic strain of the skeleton curve. The stress of the stiffness changing point of the Bauschinger part

can be calculated using Eq. A3.5.

In the case of 400 N/mm^2 and 490 N/mm^2 class structural steels

$$\Delta_t\varepsilon_B = 0.33\sum\Delta_t\varepsilon_s \tag{A3.3}$$

In the case of 590 N/mm^2 class structural steel

$$\Delta_t\varepsilon_B = 0.72\sum\Delta_t\varepsilon_s \tag{A3.4}$$

In the case of 400 N/mm^2, 490 N/mm^2 and 590 N/mm^2 class structural steels

$${}_t\sigma_E = 0.67\sum{}_t\sigma_{Bs} \tag{A3.5}$$

Fig. A3c shows an example (tension-compression cyclic loads) of the hysteresis to understand the model.

- ✧ The compressive side of the first cycle was considered as the skeleton curve owing to the initial compressive stress experienced the steel materials (loop 3-6 in Fig. A3c). The softening caused by the plastic strain in the tensile side was considered by adopting the bilinear model of the Bauschinger part (loop 4-5 in Fig. A3c).
- ✧ The entering and unloading points in the skeleton curve were reset each time when the hysteresis loop entered a skeleton curve and remained unchanged until the loop entered the subsequent skeleton curve fragment. (loops 0-2, 3-6, 7-10, 11-14, and 15-18 in Fig. A3c)
- ✧ For unloading within the plastic region of the Bauschinger part, the plastic region moved to the subsequent entering point of the skeleton curve before unloading (point 23 in Fig. A3c, which moves toward point 18).

Appendix 3: Steel Hysteresis Model

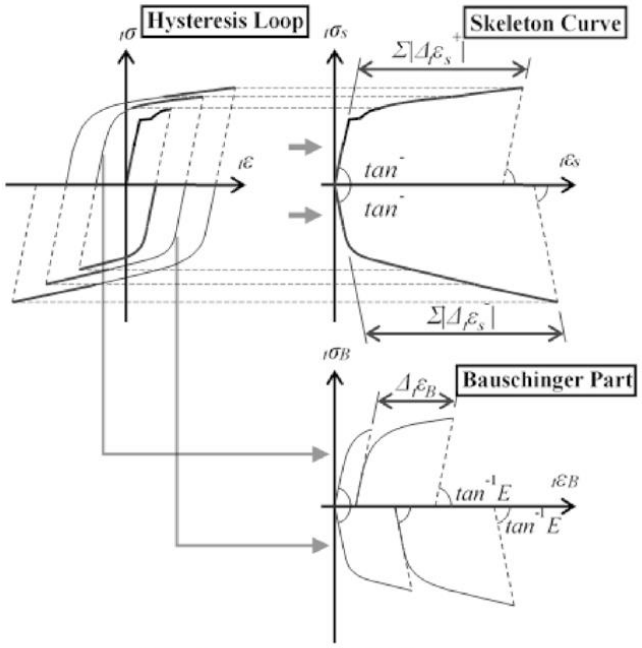

(a) Decomposition of the hysteresis curve

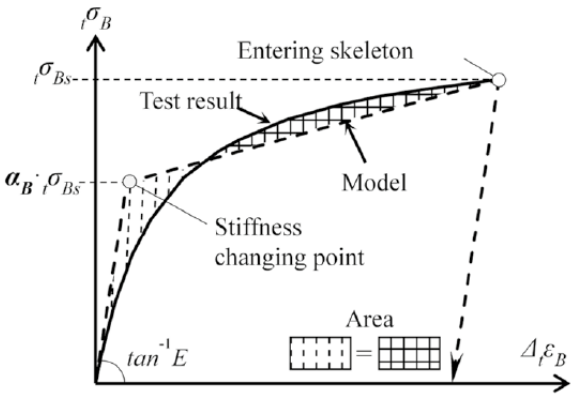

(b) Model of the Bauschinger part

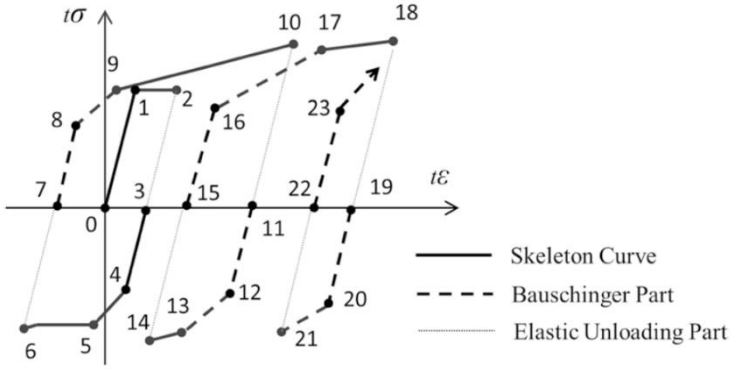

(c) Example of the hysteresis model considering the Bauschinger effect

Fig. A3 Explanation of the hysteresis model (reprinted from [A3.3])

References for Appendix 3

[A3.1] Yamada S, Jiao Y. A concise hysteretic model of structural steel considering the Bauschinger effect. International Journal of Steel Structures 2016;16:671–83. https://doi.org/10.1007/s13296-015-0134-9.

[A3.2] Yamada S, Jiao Y, Lee D-S, Ishida T, Kishiki S. A concise hysteretic model of 590 N/mm^2 grade high performance steel considering the Bauschinger effect. International Journal of Steel Structures 2020;20:1979–88. https://doi.org/10.1007/s13296-020-00401-w.

[A3.3] Yamada S, Jiao Y. Damage Evaluation Method for Steel Beams Subjected to Cyclic Loading. International Journal of Steel Structures 2022. https://doi.org/10.1007/s13296-022-00673-4.

Appendix 4: Effect of element types and mesh sizes

1. Influences of element types

To investigate the effect of element types, the analytical models using solid element with reduced integration (C3D8R) and without reduced integration (C3D8), axisymmetric shell with reduced integration (CAX4R) and without reduced integration (CAX4) are considered. In case of steel material, axisymmetric model is typically used due to its less calculation time and good accuracy. However, one of its drawbacks is initial imperfection cannot be considered due to its axisymmetric nature (the out-of-plane deformation is locked). Therefore, the analyses of these models under pure tension without imperfection are performed.

The equivalent plastic strain (PEEQ) and equivalent stress (MISES) distributions of different element types at yield strains are shown in Fig. A4.1. At yield strain, the strain and stress distribution do not show any difference regardless of the element types. Similar trend of the stress and strain distributions can be also observed at lateral displacement at U1=2.5mm (approximately 44% reduction in cross-section) as illustrated in Fig. A4.2. Although the stress and strain distribution are almost the same, their values tend to be slightly different when the reduced integration is considered for both 3D solid and axisymmetric elements. It should be noted that the analytical model with reduced integration is used owing to its less calculation time while maintaining good accuracy.

Due to less calculation time and introduction of initial imperfection are desired, C3D8R solid models with reduced integration are considered in this study.

Appendix 4: Effect of element types and mesh sizes

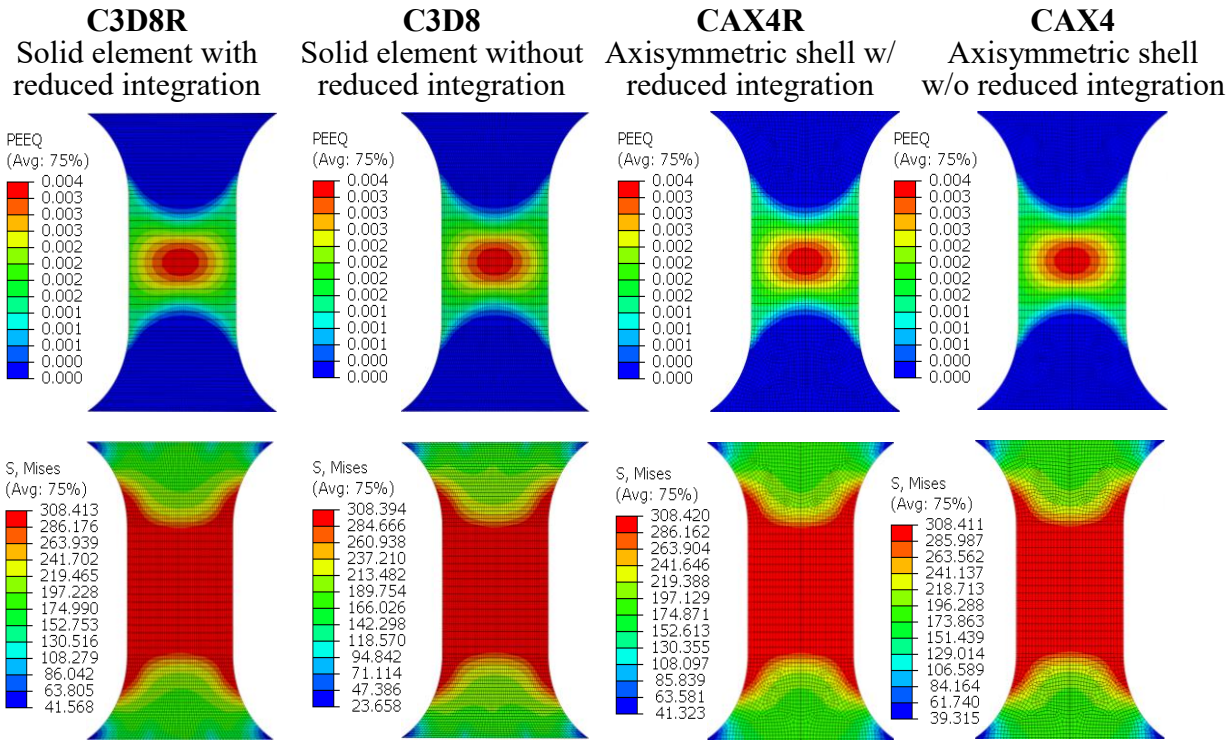

Fig. A4.1 Strain (PEEQ) and stress (MISES) distributions of different element types at yield strain (Specimen with D=17, Le/D=1.0, R/D=0.75, and mesh sizes R=0.5, Le=1.0)

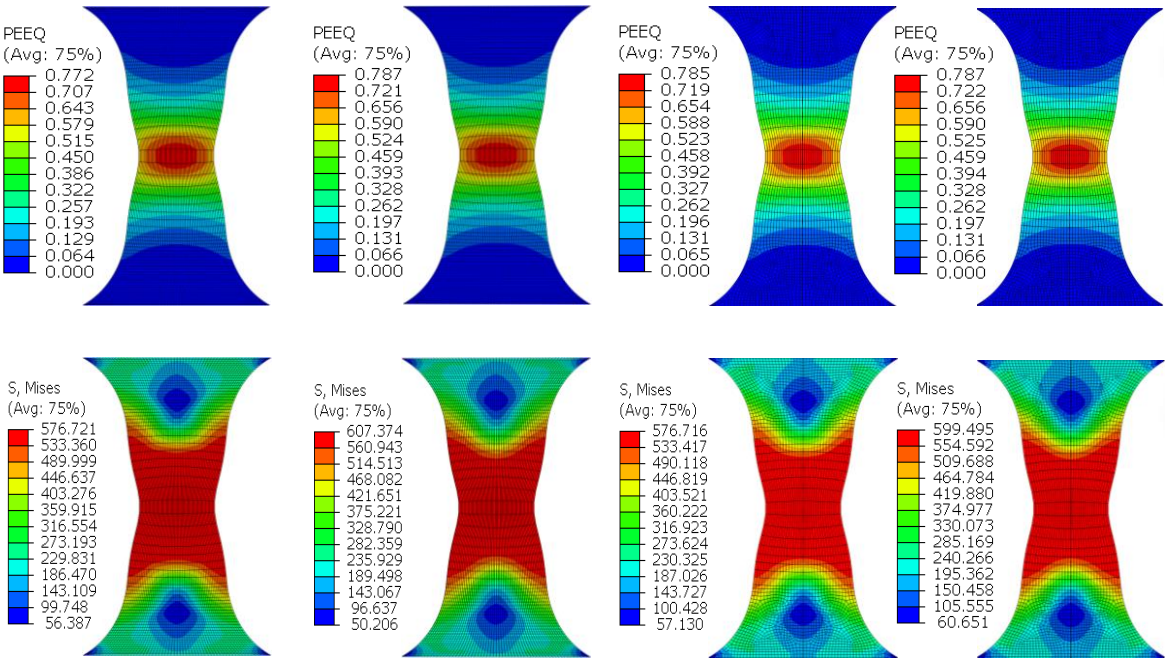

Fig. A4.2 Strain (PEEQ) and stress (MISES) distributions of different element types at U1 = 2.5mm (Specimen with D=17, Le/D=1.0, R/D=0.75, and mesh sizes R=0.5, Le=1.0)

2. Influences of mesh sizes

To examine the influences of mesh sizes, C3D8R solid elements with different mesh sizes – that is, fine, medium and coarse meshes as tabulated in Table A4.1 are considered. Figs. A4.3 and A4.4 illustrate the equivalent plastic strain (PEEQ) and equivalent plastic stress (MISES) distributions at yield strain and buckling, respectively. From Fig. A4.4, it is observed that the equivalent plastic strain tends to be larger when the mesh is finer, which is consistent with the report by the previous study e.g., [A4.1]. Nevertheless, these figures indicate the strain and stress distributions are almost similar, regardless of the mesh size. Also, Table A4.1 shows that the effect of mesh sizes on the true axial strain at buckling is almost insignificant.

Due to less calculation time while maintaining good accuracy is aspired, 3D solid models (C3D8R, an 8-node linear brick, reduced integration, hourglass control) with medium mesh are employed in this study.

Table A4.1 Strains at buckling of different mesh size

Name	Mesh size	True axial strain (%) at buckling
Fine mesh	$R = 0.25$, $Le = 0.25$	24.0
Medium mesh	$R = 0.5$, $Le = 1.0$	25.2
Coarse mesh	$R = 1$, $Le = 2.0$	24.4

References for Appendix 4:

[A4.1] Mortezagholi MH, Zahrai SM. Evaluating ultra low cycle fatigue based on ductile fracture model in double core BRBs. Eng Struct 2020;223:111158. https://doi.org/10.1016/j.engstruct.2020.111158.

Appendix 4: Effect of element types and mesh sizes

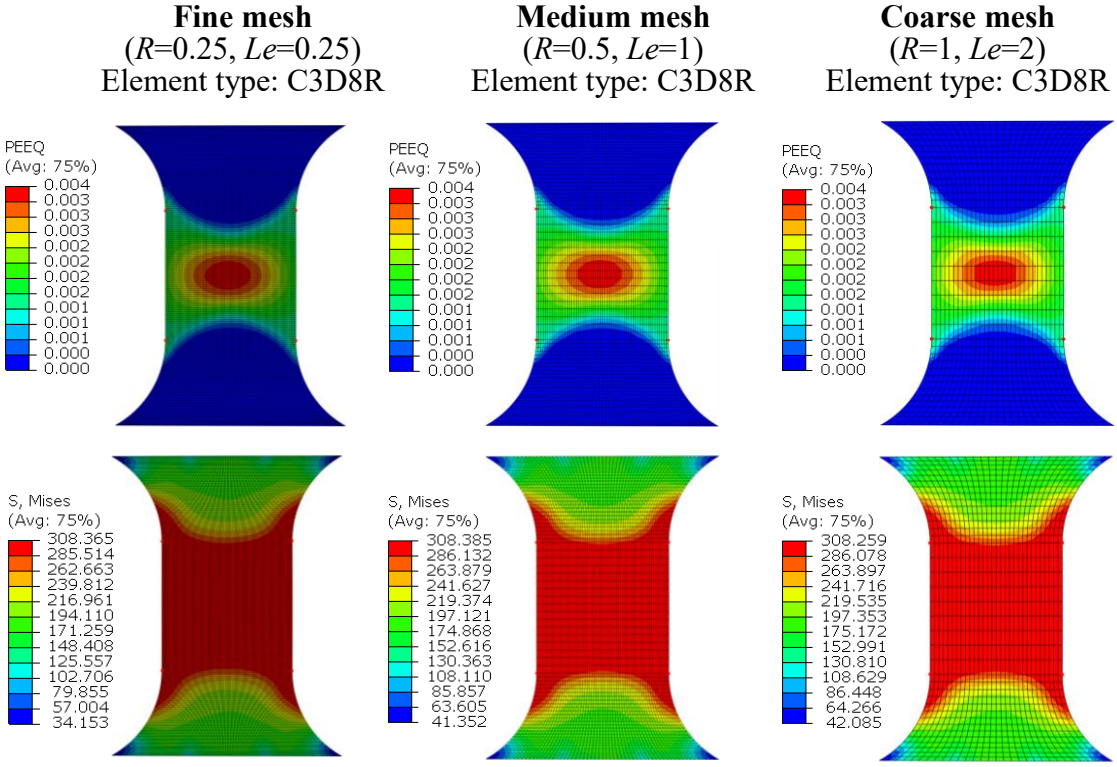

Fig. A4.3 Strain (PEEQ) and stress (MISES) distributions of different mesh sizes at yield strain (Specimen with D=17, Le/D=1.0, R/D=0.75)

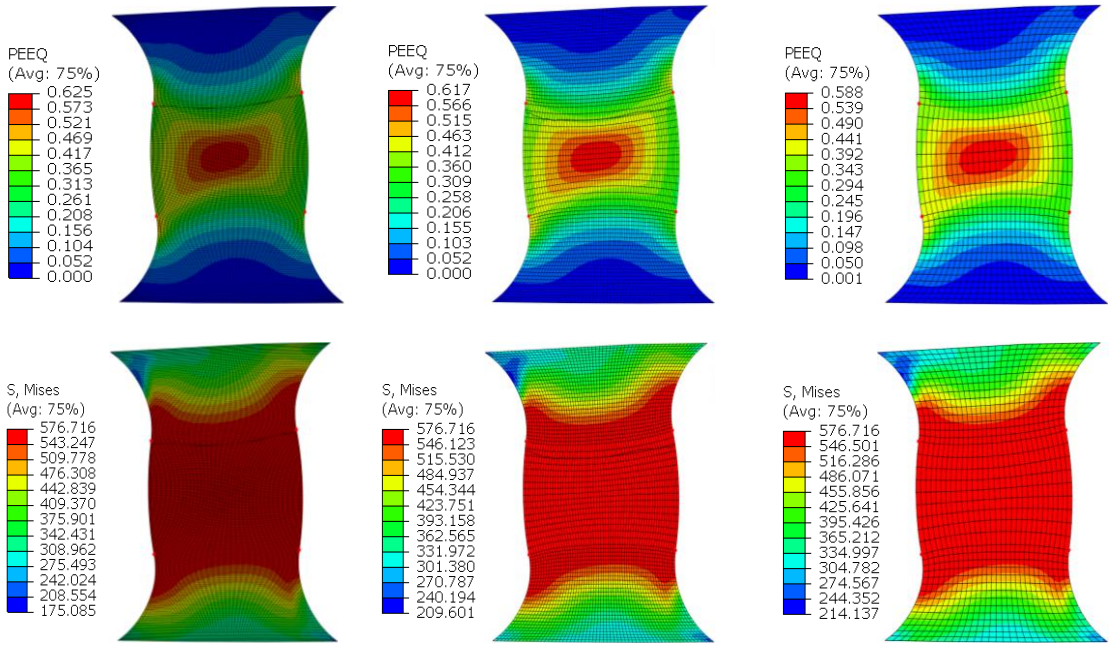

Fig. A4.4 Strain (PEEQ) and stress (MISES) distributions of different mesh sizes at buckling (Specimen with D=17, Le/D=1.0, R/D=0.75)

Appendix 5: Fracture modes

Numerous efforts have been expended by researchers to identify the transition of the fracture mode. For example, in previous studies [A5.1– A5.4], it was reported that in ordinary low-cycle fatigue regime ($N_f > 10^2$) the development of small surface cracks has led to the failure of the specimen, while at very large strain amplitudes, the fracture mode transition was caused by the development of internal cracks that originated from the shear cracking of pearlite inside the material. Additionally, previous studies [A5.5– A5.7] have indicated that the damage mechanism in the ELCF regime is a combination of the fatigue mechanism and ductile fracture process, in which the latter is more dominant because ELCF involves both the large-scale inelastic strain and cyclic loading. Likewise, Liu et al. [A5.8] who studied the ductile-fatigue transition fracture mode of welded T-joints which were subjected to quasistatic cyclic large plastic strain loading indicated that the fracture mode could transition from fatigue fracture to ductile fracture as strain amplitudes increased to a critical value.

Fig. A5 shows the fracture surfaces of Lot I and II specimens tested subject to constant amplitude cyclic and monotonic loadings. From this figure, it can be noticed that the fracture mode of specimens at small and large strain amplitudes can be categorized. The fracture mode of the specimen tested at a strain of 2% can be recognized as fatigue fracture. During the test, it was observed that specimen fractured after small surface cracks which could be identified by visual observation and which developed to have substantial sizes. These main cracks connected with each other. However, specimens tested at larger strains (> 4.5%) can be recognized owing to the accumulative ductile fracture. Necking becomes more dominant and cup-and-cone shapes (which are the characteristics for ductile fracture and can be typically observed on the fracture surface

of tensile test) can be also identified from these fracture surfaces. In particular, from Figs. A5(e) and A5(f) it is worth noting that the fracture surfaces of the specimens tested at a strain of 12% and those of the monotonic tensile tests are similar. These findings also corroborate the finding that the fracture mode of specimens tested at larger plastic strains ($\varepsilon > 4.5\%$) falls into a ductile manner.

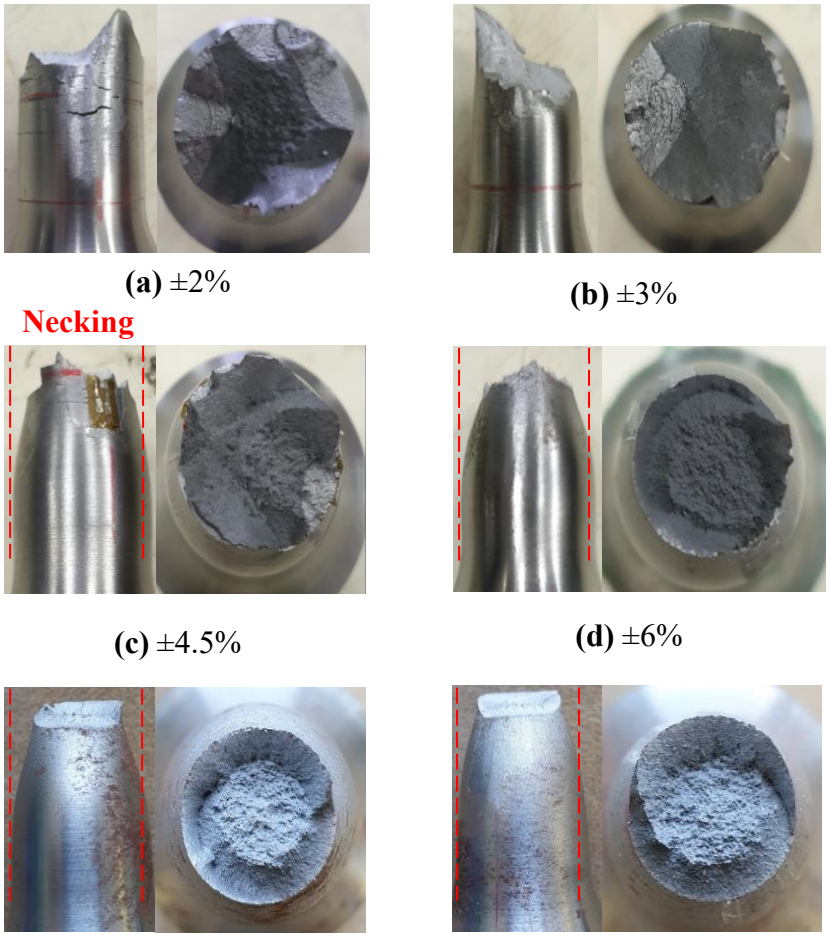

(a) ±2% **(b)** ±3%

(c) ±4.5% **(d)** ±6%

(e) ±12% **(f)** Monotonic tension

Fig. A5 Fracture surfaces of Type G specimens

References for Appendix 5:

[A5.1]Shimada K, Komotori J, Shimizu M. The applicability of the Manson-Coffin law and Miner's law to extremely low cycle fatigue. Transactions of the Japan Society of Mechanical Engineers Series A 1987;53:1178–85. https://doi.org/10.1299/kikaia.53.1178.

[A5.2]Komotori J, Yokoyama M, Shimizu M. Microstructual effect on extremely low cycle fatigue of dual phase steel. Mechanical Behaviour of Materials VI, Proceedings of the Sixth International Conferrence, Kyoto, Japan 1993:517–23. https://doi.org/10.1016/b978-0-08-037890-9.50201-5.

[A5.3]Komotori J, Shimizu M. Fracture mechanism of ferritic ductile cast iron in extremely low cycle fatigue. Low Cycle Fatigue and Elasto-Plastic Behaviour of Materials 1998:39–44.

[A5.4]Komotori J, Shimizu M. Grain size effect in low cycle fatigue of steel under mean strain. Proceedings of The 7th International Conference On Fracture (ICF7) 1989:1213–20. https://doi.org/10.1016/B978-0-08-034341-9.50135-2.

[A5.5]Bleck W, Dahl W, Nonn A, Amlung L, Feldmann M, Schäfer D, et al. Numerical and experimental analyses of damage behaviour of steel moment connection. Eng Fract Mech 2009;76:1531–47. https://doi.org/10.1016/j.engfracmech.2009.03.004.

[A5.6]Kuwamura H. Transition between fatigue and ductile fracture in steel. Journal of Structural Engineering 1997;123:864–70. https://doi.org/10.1061/(ASCE)0733-9445(1997)123:7(864).

[A5.7]Kuwamura H, Yamamoto K. Ductile Crack as Trigger of Brittle Fracture in Steel. Journal of Structural Engineering 1997;123:729–35. https://doi.org/10.1061/(ASCE)0733-9445(1997)123:6(729).

[A5.8]Liu Y, Jia LJ, Ge H, Kato T, Ikai T. Ductile-fatigue transition fracture mode of welded T-joints under quasi-static cyclic large plastic strain loading. Eng Fract Mech 2017;176:38–60. https://doi.org/10.1016/j.engfracmech.2017.02.018.

Appendix 6: Cumulative plastic strains

Definition of cumulative plastic strains

The cumulative plastic strain can be obtained as follows.

$$\sum \varepsilon_p = \varepsilon_{pi}^{+} + \varepsilon_{pi}^{-}$$

Where ε_{pi}^{+} and ε_{pi}^{-} the plastic strain at the tension side and compression side, respectively (Fig. A6.1).

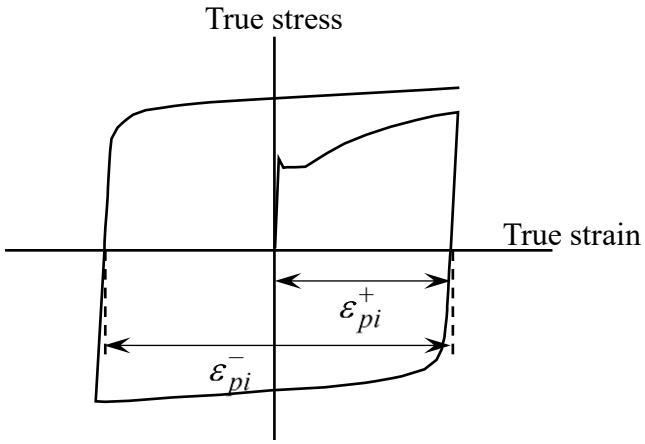

Fig. A6.1 Schematic diagram of plastic strain at tension and compression sides used for determining the cumulative plastic strains

Cumulative plastic strain of various structural steels

The relationship between cumulative plastic strain and number of cycles to damage initiation in Fig. A6.3 indicates that regardless of the different steel strength, the cumulative strain up to the fracture are almost the same extended up to the fracture strains of the tensile tests. Similarly, the cumulative strain up to damage initiation also shows linear relationship extended up to uniform elongations of the tensile test (Fig. A6.2). However, the uniform elongation of high-performance steel SA440C is lower when compared to others. This may be contributed by the effect of heat treatment to achieve

high strength. Besides, according to strain-life curves and the results from Figs. A6.2 and A6.3, it can be said that the effect of the considered steel strengths on the cumulative plastic strain in the low and extremely low cycle fatigue regimes is almost insignificant.

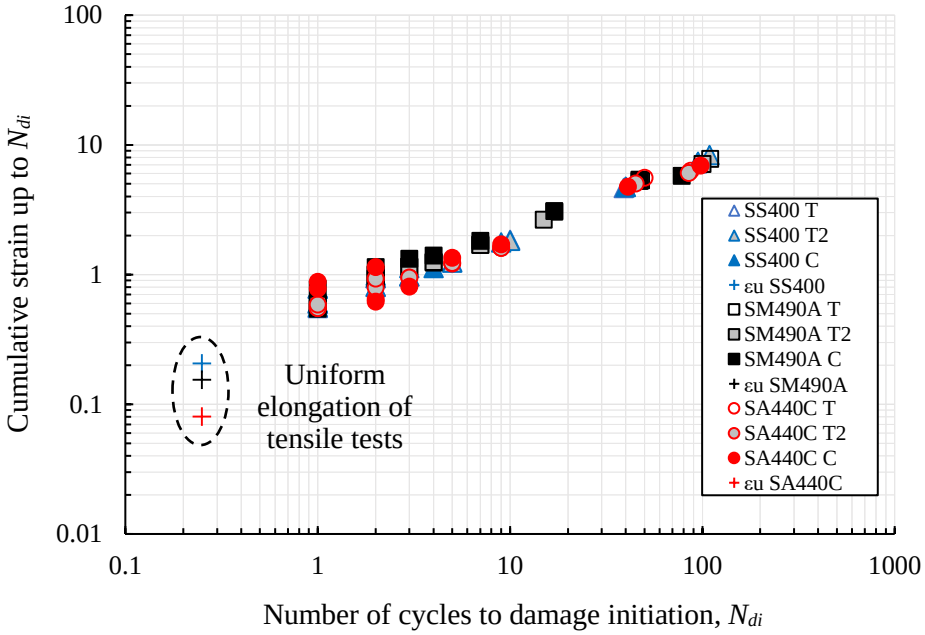

Fig. A6.2 Cumulative plastic strain vs. number of cycles to damage initiation

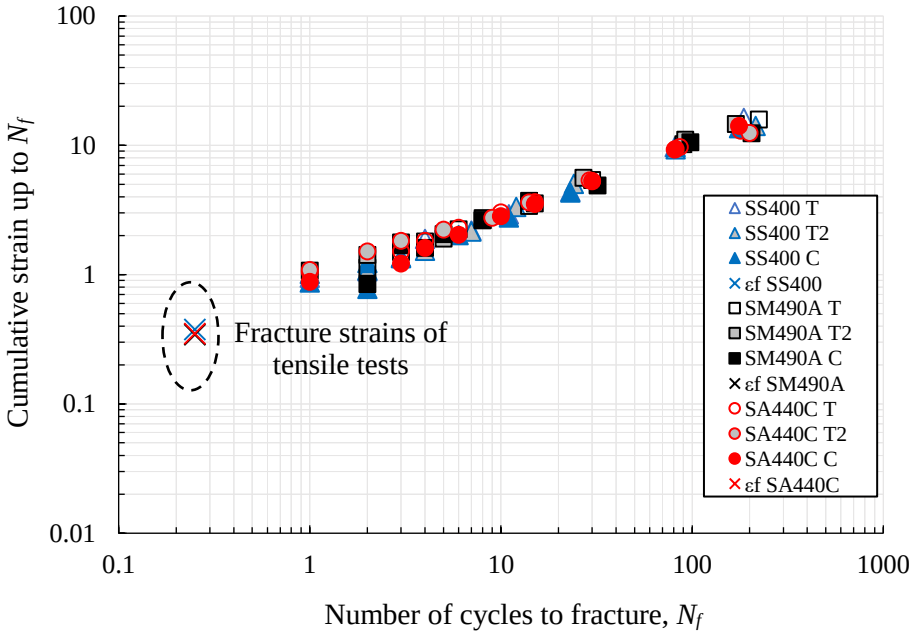

Fig. A6.3 Cumulative plastic strain vs. number of cycles to fracture

Appendix 7: Plastic strain energy

Definition of plastic strain energy

The plastic strain energy is determined by calculating the area of the true stress – true strain hysteretic curve at each cycle as schematically illustrated in Fig. A7.1.

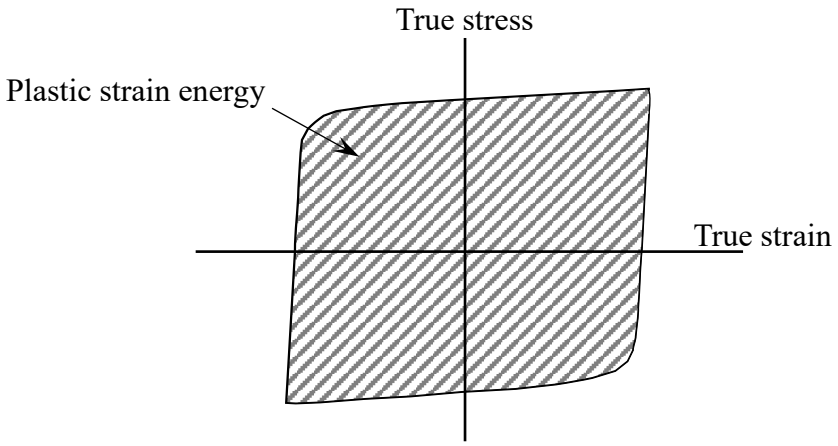

Fig. A7.1 Schematic diagram of plastic strain energy

Plastic strain energy of various structural steels

From Fig. A7.2, it is observed that the plastic strain energy of various structural steels shows linear relationship together. However, the scatter of the dissipated energy at similar cycles seem to be slightly greater if compared to the cumulative plastic strains. The amount of dissipated energy tends to be slightly greater for higher strength steels, provided that the number of cycles (N_{di} and N_f) of these structural steels is similar. The same trend is also observed (in Fig. A7.3) for plastic strain energy up to N_f.

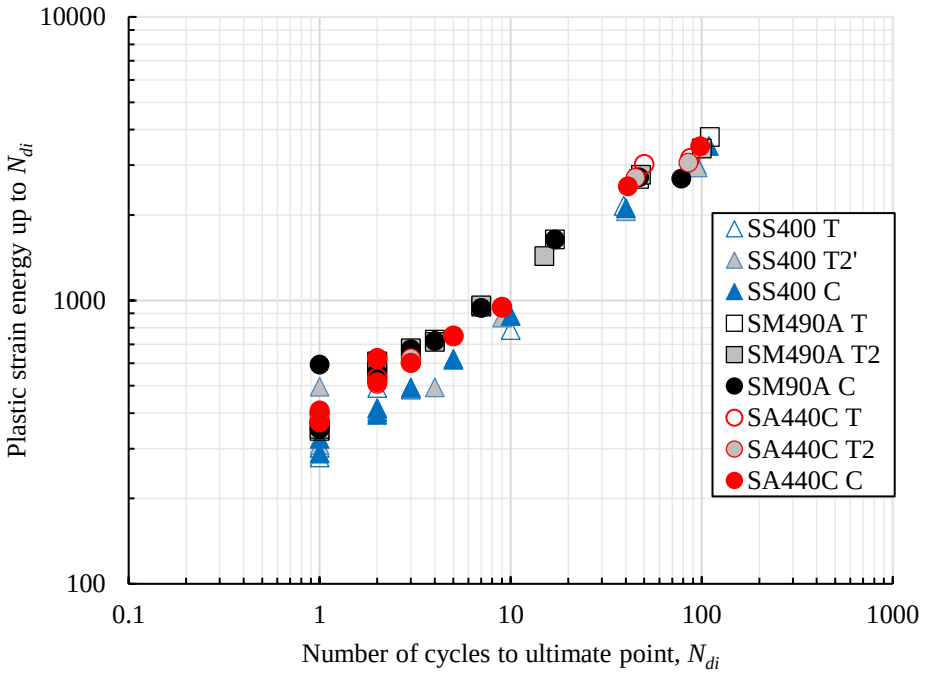

Fig. A7.2 Plastic strain energy vs. number of cycles to ultimate point

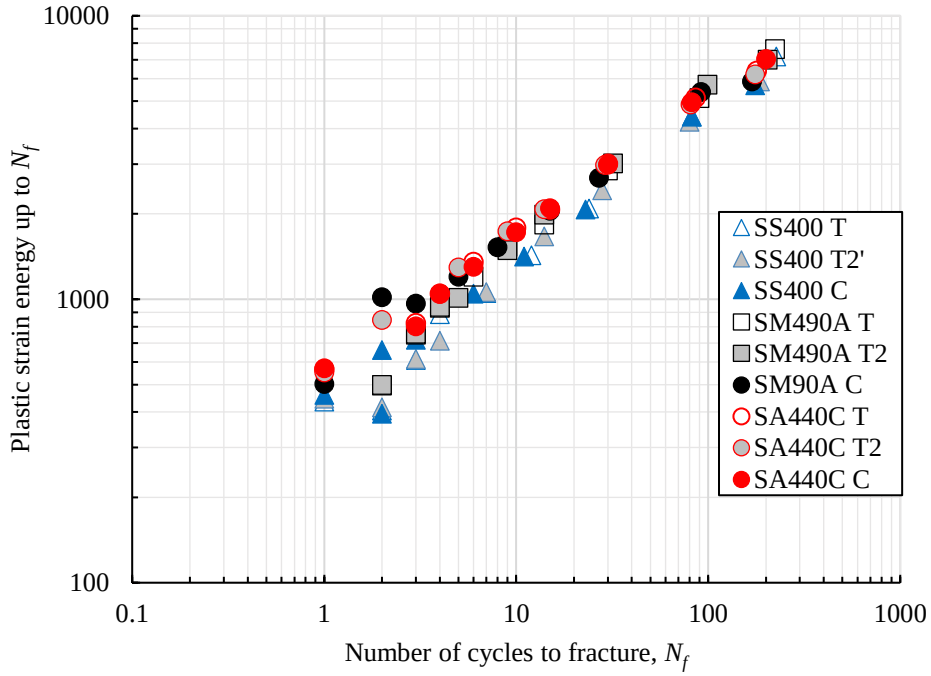

Fig. A7.3 Plastic strain energy vs. number of cycles to fracture

List of publications

Peer-reviewed international journal papers

1. S. Yamada, T. Touch, Y. Jiao, T. Ishida, S. Kishiki, Deformation capacity of 400 N/mm^2 class structural steel under extremely large strains, Journal of Constructional Steel Research, Vol. 182, Article 106678, July 2021. https://doi.org/10.1016/j.jcsr.2021.106678. (regarding Chapter 2 & 3)
2. S. Yamada, T. Touch, Y. Jiao, S. Kishiki, Cyclic deformation capacities of structural steels for earthquake-resistant steel buildings, Journal of Earthquake Engineering. Under review (regarding Chapter 3)
3. "Investigation of optimal round specimen shapes under large tensile and compressive strains" regarding Chapter 2 (in preparation)

Peer-reviewed domestic conference papers

1. トッチ タイリン、山田 哲、石田 孝徳、焦 瑜、大歪振幅繰り返し載荷を受ける構造用鋼材の実験、鋼構造年次論文報告集第 27 巻(2019 年 11 月)
2. T. Touch, S. Yamada, T. Ishida, Y. Jiao, S. Kishiki, Cyclic Deformation Capacity up to Ultimate Strength and Fracture of Structural Steel SS400 under Large Strains, Proc. Constr. Steel. 28, pp 949–955, 2020.
3. 焦 瑜、前島淳平、トッチ タイリン、山田 哲、河野 守、吉敷　祥一、地震による損傷を受けた建築構造用鋼材の高温時力学特性、鋼構造年次論文報告集第 30 巻(2022 年 11 月)

International conference papers (Oral presentation)

1. T. Touch, S. Yamada, T. Ishida, and Y. Jiao, Extremely Low Cycle Fatigue Behavior of Structural Steel, 10th International Symposium on Steel Structures, November 13-16, 2019, Jeju, Korea

Domestic conference paper (Oral presentation)

1. T. Touch, S. Yamada, T. Ishida, Y. Jiao. Experimental Study on Fatigue Characteristics of Structural Steel Part 1: Extremely Low Cycle Fatigue of Structural Steel SS400. Summaries of technical papers of annual meeting, Architectural Institute of Japan, pp. 1003-1004, Sept. 2019.
2. T. Touch, S. Yamada, T. Ishida, Y. Jiao. Experimental Study on Fatigue Characteristics of Structural Steel Part 2: Cyclic Deformation Capacity of Structural Steel SS400 under Large Strain Amplitude. Summaries of technical papers of annual meeting, Architectural Institute of Japan, pp. 667-668, Sept. 2020.
3. T. Touch, S. Yamada, T. Ishida, Y. Jiao, Shoichi Kishiki. Experimental Study on Fatigue Characteristics of Structural Steel Part 3: Deformation Capacities of

Various Structural Steels under Large Strain Amplitudes. Summaries of technical papers of annual meeting, Architectural Institute of Japan, pp. 675-676, Sept. 2021.

4. T. Touch, S. Yamada, Y. Jiao, S. Kishiki. Experimental Study on Fatigue Characteristics of Structural Steel Part 4: Cyclic Deformation Capacities up to the Ultimate Point. Summaries of technical papers of annual meeting, Architectural Institute of Japan, pp. 1021-1022, July 2022.
5. T. Touch, S. Yamada, T. Ishida, Y. Jiao. Cyclic Loading Test of SS400 Steel under Large Strain Amplitude, Proceeding of the Architectural Research Meetings, Kanto Chapter, Architectural Institute of Japan, Vol. 90, pp. 449-452, Mar. 2020.
6. T. Touch, S. Yamada, T. Ishida, Y. Jiao, S. Kishiki. Deformation Capacities of Various Structural Steels under Cyclic Loadings of Very Large Inelastic Strains, Proceeding of the Architectural Research Meetings, Kanto Chapter, Architectural Institute of Japan, Vol. 91, pp. 157-160, Mar. 2021.
7. 焦 瑜, 前島 淳平, トッチ タイリン, 山田 哲, 河野 守, 吉敷 祥一. 地震による損傷を受けた建築構造用鋼材の高温時力学性能 その 1 実験の概要, 日本建築学会大会大会学術講演, 日本建築学会大会学術講演梗概集, 構造Ⅲ, pp. 5-6, July 2022.
8. 前島 淳平, 焦 瑜, トッチ タイリン, 山田 哲, 河野 守, 吉敷 祥一. 地震による損傷を受けた建築構造用鋼材の高温時力学性能 その 2 実験結果及び検討, 日本建築学会大会大会学術講演, 日本建築学会大会学術講演梗概集, 構造Ⅲ, pp. 7-8, July 2022.

Acknowledgements

Although these words are the last to be written, they are the most important as the conduct of this dissertation for 5 years would be impossible without the contribution of the following people.

First and foremost, I would like to express my sincere and greatest gratitude to my supervisor, Professor **Shoichi Kishiki**. Despite being strict and persistent in the research, he always encourages as well as takes good cares of students besides his busy schedule. He is excellent in conceptualizing and presenting the research works. He always suggests good and creative stories about the research direction. He shares insightful advices in both academic and daily life. I have learnt a lot from him on the research aspect and life philosophy.

I wish to express my gratitude to Professor **Satoshi Yamada** of The University of Tokyo for his advice and patience in supervising me as well as the navigation through various aspects of research. He gave me a chance to come to Tokyo Institute of Technology. Even after moving to The University of Tokyo, he still finds time to have a discussion on the research work despite his busy schedule.

I would also like to express my gratitude to Professor **MOTOYUI Shojiro**, Professor **ISHIHARA Tadashi**, Professor **NISHIMURA Koshiro**, Professor **SATO Daiki** for serving on my doctoral committee and for contributing insightful and invaluable advices and comments on this dissertation. Your insightful comments and advice aid in the improvement and enhancement of the dissertation's quality.

Additionally, I would like to extend my gratitude to Associate Professor **Yu Jiao** of Tokyo City University. She is so kind and good caretaker. She always gives good advices on research and insightful life philosophy to me. She even discusses the future career and life after graduate with me. Thanks for the continuous and consistent guidance on experiments and insightful comments all the way along my research.

I would like to thank to Associate Professor **Takanori Ishida** of Yokohama National University for his valuable guidance on experiments and insightful comments when he was in Tokyo Institute of Technology.

I also would like to thank **OKUBO Motoko** san, **ENDO Yuko** san, and **NAGAMI**

Eiko san for offering me as well as the whole Kishiki lab members valuable spiritual support.

I would like to extend my gratitude to **MEXT** scholarship and **Iwatani** foundation for the financial support all along my academic life in Japan.

I wish to express my heartfelt appreciation to **my parents and family**. It has been ten years since I left my home country to study in Japan. Their loves and consistent supports are what making this moment reachable to where it should be. Last but not least, I wish to express my sincere and greatest gratitude to my beloved **wife** for understanding, supporting, cheering me up all the way along this journey.